Government of **Western Australia**
Department of **Mines, Industry Regulation and Safety**

RECORD 2018/12

CAPRICORN OROGEN RUTILE STUDY: A COMBINED ELECTRON BACKSCATTER DIFFRACTION (EBSD) AND LASER ABLATION SPLIT STREAM (LASS) ANALYTICAL APPROACH

by
D Plavsa, S Reddy, C Clark and A Agangi

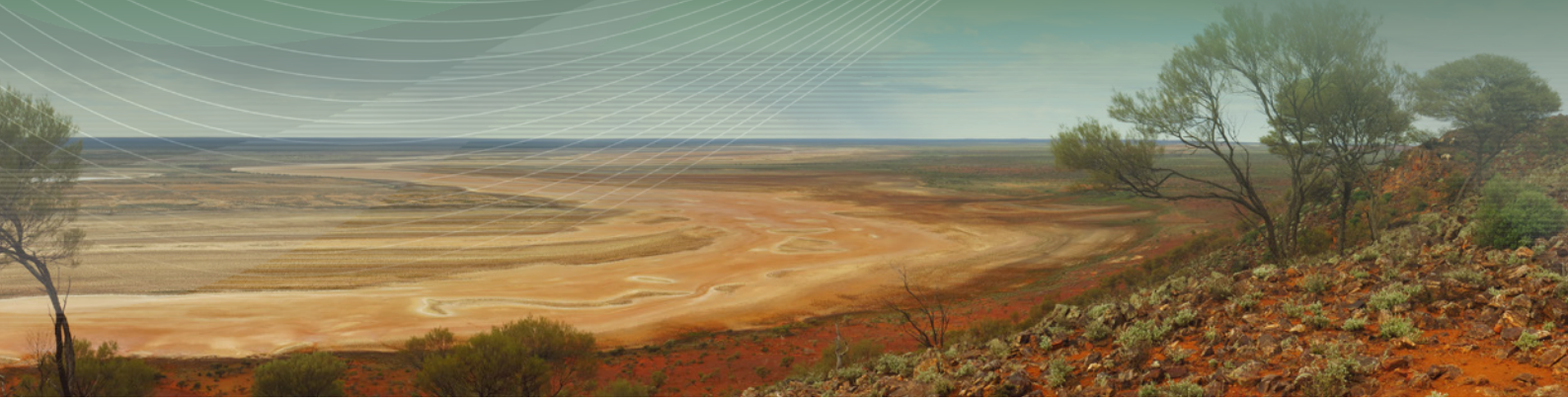

Geological Survey of Western Australia

Government of **Western Australia**
Department of **Mines, Industry Regulation and Safety**

RECORD 2018/12

CAPRICORN OROGEN RUTILE STUDY: A COMBINED ELECTRON BACKSCATTER DIFFRACTION (EBSD) AND LASER ABLATION SPLIT STREAM (LASS) ANALYTICAL APPROACH

by
D Plavsa[1], S Reddy[1], C Clark[1] and A Agangi[1,2]

1 School of Earth and Planetary Sciences, Curtin University, Bentley WA 6845, Australia
2 Department of Geology, University of Johannesburg, 2006 Auckland Park, South Africa

PERTH 2018

Geological Survey of Western Australia

MINISTER FOR MINES AND PETROLEUM
Hon Bill Johnston MLA

DIRECTOR GENERAL, DEPARTMENT OF MINES, INDUSTRY REGULATION AND SAFETY
David Smith

EXECUTIVE DIRECTOR, GEOLOGICAL SURVEY AND RESOURCE STRATEGY
Jeff Haworth

REFERENCE
The recommended reference for this publication is:
Plavsa, D, Reddy, S, Clark, C and Agangi, A 2018, Capricorn Orogen rutile study: a combined Electron Backscatter Diffraction (EBSD) and laser ablation split stream (LASS) analytical approach: Geological Survey of Western Australia, Record 2018/12, 54p.

ISBN 978-1-74168-835-1
ISSN 0728-2311

Grid references in this publication refer to the Geocentric Datum of Australia 1994 (GDA94). Locations mentioned in the text are referenced using Map Grid Australia (MGA) coordinates, Zone 50. All locations are quoted to at least the nearest 100 m.

John de Laeter Centre

Published 2018 by the Geological Survey of Western Australia
This Record is published in digital format (PDF) and is available online at <www.dmp.wa.gov.au/GSWApublications>.

Further details of geological products and maps are available from:
Information Centre
Department of Mines, Industry Regulation and Safety
100 Plain Street
EAST PERTH WESTERN AUSTRALIA 6004
Telephone: +61 8 9222 3459 Facsimile: +61 8 9222 3444
www.dmp.wa.gov.au/GSWApublications

Cover image: Elongate salt lake on the Yilgarn Craton — part of the Moore–Monger paleovalley — here viewed from the top of Wownaminya Hill, 20 km southeast of Yalgoo, Murchison Goldfields. Photograph by I Zibra, DMIRS

Contents

Figures

Appendices

Tables

Appendix tables are available on the accompanying zip file

Figures

Capricorn Orogen regional rutile study: a combined Electron Backscatter Diffraction (EBSD) and laser ablation split stream (LASS) analytical approach

by

D Plavsa[1], S Reddy[1], C Clark[1] and A Agangi[1,2]

Abstract

Using an integrated scanning electron microscope (SEM), electron backscatter diffraction (EBSD), and laser ablation split stream inductively coupled plasma mass spectrometry (LASS-ICPMS) approach, rutile was analysed from eight different rock packages in the Capricorn Orogen, Western Australia, including the 2240–2125 Ma Moogie Metamorphics, the 1840–1810 Ma Leake Spring Metamorphics, the 1820–1775 Ma Moorarie Supersuite, the 1760–1680 Ma Pooranoo Metamorphics, the 1673–1455 Ma Edmund Group, in addition to single samples from the 2758–2585 Ma Warrigal Gneiss, the 2005–1975 Ma Dalgaringa Supersuite, and the 2014–1920 Ma Bryah Group. U–Pb geochronology and Zr-in-rutile geothermometry of rutile revealed that multiple events affected the Moogie Metamorphics, at c. 1890 Ma (average Zr-in-rutile temperature = 674°C), c. 1200 Ma, and at c. 870 Ma. Rutile from the Moorarie Supersuite yielded magmatic cooling ages of 1776–1763 Ma. The c. 870 Ma event recorded by rutile within the Moogie Metamorphics is associated with the increase in W, Nb and Ta and demonstrates the power of the LASS method in establishing the timing of events associated with a significant increase in pathfinder elements. Two samples from the base of the Edmund Group yielded detrital rutile ages of 1685–1680 Ma (T = 700–600°C), here attributed to the Mangaroon Orogeny, and a younger low-grade metamorphic overprint at approximately 1100–1000 Ma, contemporaneous with the Edmundian Orogeny. The upper part of the Edmund Group (Ullawarra Formation) yielded only detrital rutile with a spread in ages ranging from Archean to Paleoproterozoic.

The trace element geochemistry of different TiO_2 polymorphs of the Moorarie Supersuite is quite variable, therefore polymorph distinction is essential when studying TiO_2 chemistry from mineral deposits. Discrimination diagrams for rutile provenance (Nb vs Cr) and rutile associated with mineralization [Ti, 100(Fe+Cr+V), 1000(W) ternary diagrams] need to be used with caution, as they do not efficiently discriminate rutile source provenance or mineralized rutile grains.

KEYWORDS: anatase, brookite, Capricorn Orogen, detrital minerals, geochemistry, uranium thorium lead dating, Proterozoic, rutile

Introduction

Rutile (tetragonal TiO_2) is an accessory rock-forming mineral that can be found in many metamorphic, igneous and detrital sedimentary rocks. The robustness of rutile under certain geological conditions, including surficial processes, as well as medium- to high-grade metamorphism, make it a useful mineral for geochemical, geochronological and thermochronological studies (Cherniak et al., 2007; Tomkins et al., 2007; Meinhold, 2010; Zack et al., 2011). The geochemistry of rutile — in particular, the high affinity of rutile for intake of high field strength elements (HFSE), such as Nb and Ta — has proven useful in studies of subduction zone processes (Foley et al., 2000; Rudnick et al., 2000), as well as provenance studies where elements such as Cr and Nb have been used to distinguish between metapelitic vs metamafic sources (Zack et al., 2002, 2004; Triebold et al., 2007, 2012). Furthermore, concentrations of Zr in rutile have been shown to be temperature and pressure dependent when buffered in the presence of zircon and quartz (Cherniak et al., 2007; Tomkins et al., 2007), thereby making rutile a particularly useful thermochronological tracer, especially in studies concerning the estimation of closure temperatures during exhumation and cooling. When combined with U–Pb geochronology, this method becomes very useful in deciphering the tectono-thermal history of ancient orogenic belts.

In addition to studies of rutile chemistry in common igneous and metamorphic rocks, anomalous compositions of rutile have been reported from mesothermal and gold-related deposits, as well as base metal deposits, with earliest reports of anomalous (high W and Sb) rutile compositions at the Big Bell gold deposit in Western Australia, by Graham and Morris (1973). Subsequent work on rutile compositions, in association with different types of ore deposits around the world (Clark and Williams-Jones, 2004; Meinhold, 2010), has shown that substitutions of Ti by elements such as V, W, Sb, Sn, Cr as well as Nb and Ta may be used as potential pathfinder elements in mineral exploration.

1 Centre for Exploration Targeting (CET), Curtin Node, School of Earth and Planetary Sciences, Curtin University, Bentley WA 6845

2 Department of Geology, University of Johannesburg, 2006 Auckland Park, South Africa

However, aside from the studies of Scott and Radford (2007) and Rice et al. (1998), a vast majority of studies on the potential of rutile as a vectoring mineral are limited by the lack of determination of the different types of the rutile polymorphs (anatase and brookite), all of which have been shown to have different chemistries (Triebold et al., 2011). Furthermore, in establishing the true potential of rutile as a vectoring mineral, it is essential to establish a 'background signature', not only in the unaltered wallrocks immediately adjacent to the known ore deposits, but also variations in rutile chemistry in different types of rocks on a regional scale.

The Paleoproterozoic Capricorn Orogen in Western Australia covers an area of approximately 220 000 km^2 and is located between the adjoining Archean Pilbara and Yilgarn Cratons (Fig. 1a). Recent discoveries of a number of volcanogenic massive sulfide (VMS) strata-bound base metal, orogenic gold, shear zone-related tungsten and rare earth element (REE) deposits (Pirajno, 2004; Johnson et al., 2013) have prompted an investigation into the mineral potential of the Capricorn Orogen. Furthermore, a recent crustal-scale seismic survey carried out across the western part of the Capricorn Orogen (Johnson et al., 2011a; 2013) indicates a number of mantle-tapping shear zones that may provide conduits for hydrothermal fluid flow and, consequently, increased mineralization potential.

In order to better characterize the mineralization potential of the Capricorn Orogen, a regional-scale study of rutile geochemistry was conducted to evaluate the applicability of rutile as a trace of crustal fluid circulation and hydrothermal events. An integration of different analytical methods, including electron backscatter diffraction (EBSD) for polymorph distinction, optical microscope and scanning electron microscope (SEM) for textural relationships, and laser ablation split stream (LASS) mass spectrometry (Kylander-Clark et al., 2013) for simultaneous acquisition of age and compositional data on rutile grains, is employed in order to establish geochemical trends between mineralized and unmineralized rocks, as well as the associated changes in TiO_2 polymorphs. This Record is focused on the western part of the Capricorn Orogen (the Gascoyne Province), including the lithologies transected by the seismic survey (Fig. 2) carried out in 2011 (Johnson et al., 2011a; 2013).

Regional tectonic setting

The Paleoproterozoic Capricorn Orogen, located between the Archean Pilbara and Yilgarn Cratons in Western Australia (Fig. 1), comprises Archean to Mesoproterozoic igneous plutonic rocks and medium- to high-grade metamorphic rocks of the Gascoyne Province in the west. Low-grade metasedimentary and mafic volcanic rocks are distributed throughout the orogen (Fig. 1) and comprise the Paleoproterozoic Yerrida, Bryah, Padbury, Earaheedy, Bresnahan, Ashburton, Blair and Mount Minnie Basins, and the Paleoproterozoic to Mesoproterozoic Edmund and Collier Basins (Cawood and Korsch, 2008; Martin et al., 2008; Johnson et al., 2013). The Capricorn Orogen records a protracted and punctuated tectono-thermal history spanning most of the Proterozoic, with the earliest interpretations favouring a model of oblique collision between the Archean Pilbara and Yilgarn Cratons during the 1820–1770 Ma Capricorn Orogeny (Horwitz and Smith, 1978; Tyler and Thorne, 1990; Evans et al., 2003). However, subsequent geochronological work carried out largely by the Geological Survey of Western Australia (GSWA) revealed a more complex tectono-thermal history with a two-stage collisional process, and the presence of previously undefined allochthonous terrane, now commonly referred to as the Glenburgh Terrane (Johnson et al., 2011c). The first stage in the amalgamation of the greater Western Australian Craton (WAC) involved the collision of the Glenburgh Terrane with the southern margin of the Pilbara Craton during the 2215–2145 Ma Ophthalmia Orogeny (Müller et al., 2005; Rasmussen et al., 2005). The combined Pilbara—Glenburgh terrane, also referred to as the Pilboyne Craton (Johnson, 2013), then collided with the northern margin of the Yilgarn Craton during the 2005–1950 Ma Glenburgh Orogeny (Kinny et al., 2004; Occhipinti et al., 2004; Sheppard et al., 2004; Johnson et al., 2011b). Post-collisional reworking of the Capricorn Orogen included several disparate intracratonic tectono-thermal events, of which the Capricorn Orogeny (1820–1770 Ma) is the most widespread and affected the entire Capricorn Orogen. The Capricorn Orogeny is also associated with significant granitic magmatism of the 1820–1775 Ma Moorarie Supersuite (Occhipinti et al., 1998; Occhipinti and Sheppard et al., 2001), and greenschist to upper amphibolite facies metamorphism (Sheppard et al., 2010a). Subsequent tectono-thermal events were more localized and typically associated with reactivation of previous crustal-scale shear zones. These events include:

- the 1680–1620 Ma Mangaroon Orogeny (Sheppard et al., 2005), also associated with significant granitic magmatism of the 1680–1620 Ma Durlacher Supersuite (Sheppard et al., 2010b), is most prominent in the northern part of the Gascoyne Province (the Mangaroon Zone, Fig. 2)
- the 1321–1171 Ma Mutherbukin Tectonic Event (Korhonen et al., 2015, 2017 and references therein), although not associated with significant magmatism, it is associated with hydrothermal fluid flow and an increase in the metamorphic grade from greenschist to upper amphibolite-facies metamorphism from the northern to the central portions of the Gascoyne Province, respectively
- the 1030–955 Ma Edmundian Orogeny (Sheppard et al., 2007) that was largely responsible for folding and deformation of the Mesoproterozoic Edmund and Collier Basins in the northern and eastern parts of the Capricorn Orogen
- the 930–750 Ma Kuparr Tectonic Event (Cutten and Johnson, 2018) as determined by $^{40}Ar/^{39}Ar$ dating of micas and U–Pb dating of phosphate minerals within major province-wide shear zones (Occhipinti, 2007; Occhipinti and Reddy, 2009; Piechocka et al., 2018) and by K–Ar dating of illite from slickenlines and fault breccias within the Edmund Group (Cutten and Johnson, 2018)
- the c. 570 Ma Mulka Tectonic Event, associated with reactivation of pre-existing faults (Bodorkos and Wingate, 2007).

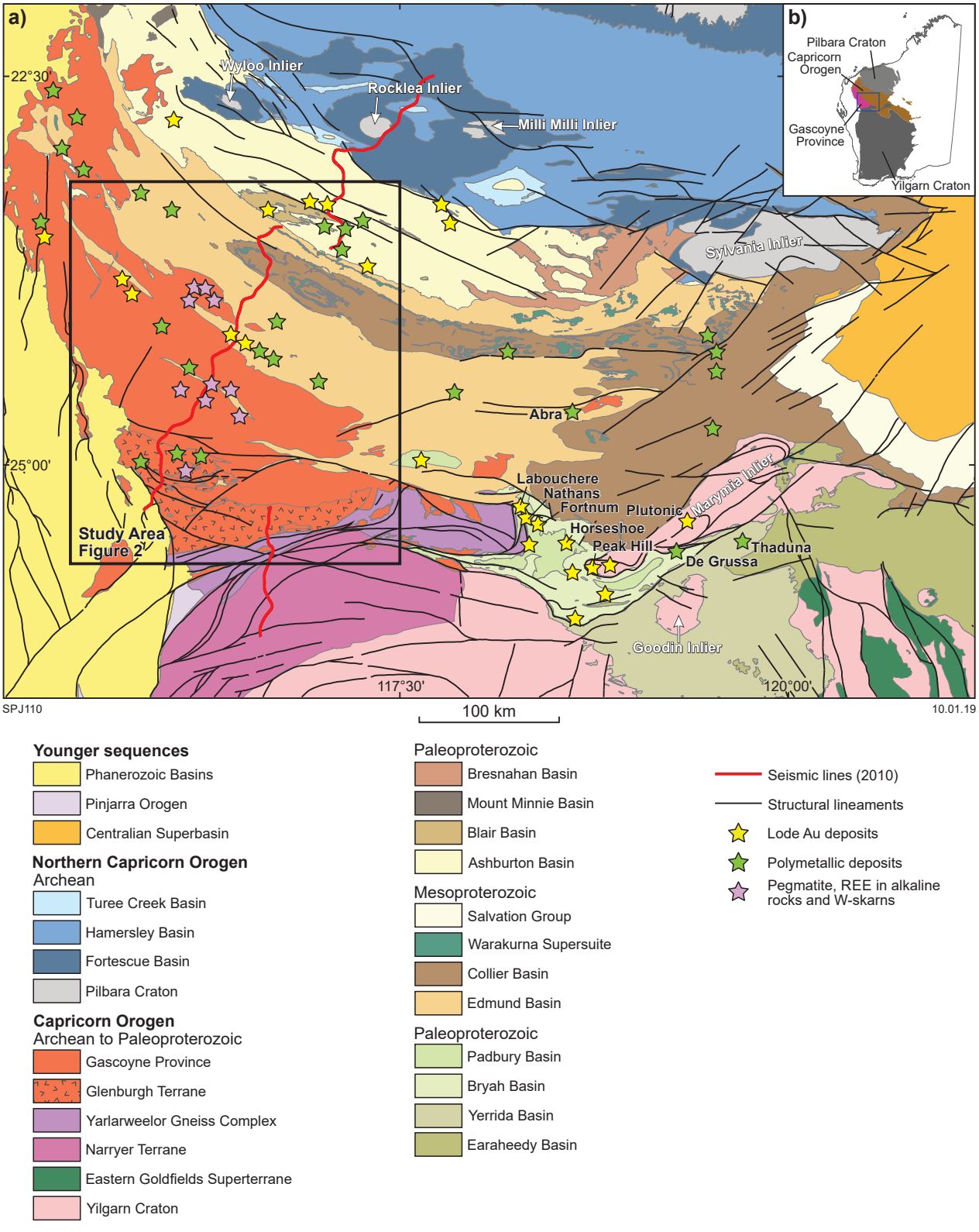

Figure 1. Geological map of the main tectonic units in the Capricorn Orogen, Western Australia: a) location of the Capricorn Orogen; b) Capricorn Orogen tectonic units

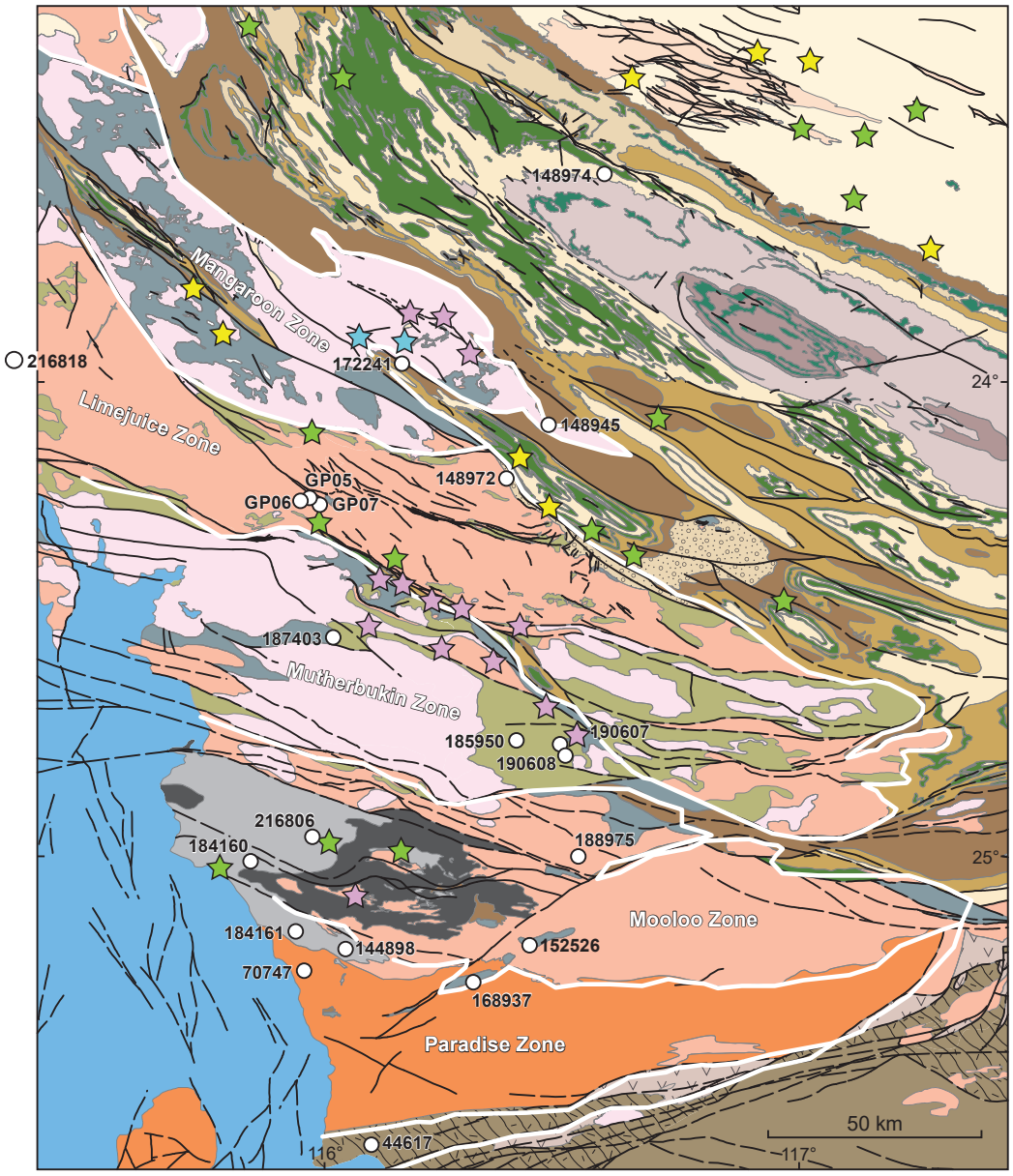

Figure 2. Geological map of the study area and the locations of analysed samples. Locations of ore deposits from Johnson et al. (2013) and Pirajno (2004)

Gascoyne Province

The focus of this study is the western part of the Capricorn Orogen and, in particular, the Gascoyne Province and the Paleo- to Mesoproterozoic Edmund Group (Fig. 2). The tectonic evolution of the Gascoyne Province has been described in detail by various authors, most notably Sheppard et al. (2004, 2005, 2010a,b), Johnson et al. (2011c, 2013, 2017), Korhonen and Johnson (2015) and Korhonen et al. (2017). A short summary is provided here, with the list of main sedimentation, magmatic and orogenic events listed in the legend to Figure 2. The current exposures of the Gascoyne Province provide clues for the punctuated tectono-thermal history, commencing with the collision of the oldest crustal unit: the combined Pilbara Craton—Glenburgh Terrane (aka Pilboyne Craton, Johnson et al., 2013) with the northern margin of the Yilgarn Craton during the 2005–1950 Ma Glenburgh Orogeny (Johnson et al., 2011b). The continental Andean-style magmatic arc that intruded the Glenburgh Terrane above a north-dipping subduction zone (the 2005–1975 Ma Dalgaringa Supersuite) along with the foreland sediments (the 2240–2125 Ma Moogie Metamorphics and the 2001–1955 Ma Camel Hill Metamorphics) were deformed during this orogeny (Occhipinti et al., 2004; Sheppard et al., 2004; Johnson et al., 2011b). Subsequently, the Gascoyne Province has undergone a protracted intracratonic sedimentation and tectono-thermal history, including deposition of sedimentary packages during basin-forming events and intrusion of voluminous felsic to mafic magmatic suites that were either synchronous or pre-date a number of disparate tectono-thermal events. The metasedimentary packages include the 1840–1810 Ma Leake Spring Metamorphics intruded by granitic rocks of the 1820–1775 Ma Moorarie Supersuite, and the 1760–1680 Ma Pooranoo Metamorphics intruded by granitic rocks of the 1680–1620 Ma Durlacher Supersuite (Fig. 2). Intrusion of the Moorarie Supersuite appears to have been contemporaneous with the widespread 1820–1770 Ma Capricorn Orogeny, whereas intrusion of the Durlacher Supersuite was contemporaneous with the younger 1680–1620 Ma Mangaroon Orogeny (Sheppard et al., 2005).

Basement rocks of the Gascoyne Province are unconformably overlain by the 1673–1455 Ma Edmund and 1171–1067 Ma Collier Groups, with an early deformation event, the 1321–1171 Ma Mutherbukin Tectonic Event (Korhonen et al., 2017), deforming the Edmund Group sedimentary rocks (Cutten et al., 2016). Both basins were variably deformed during the 1030–955 Ma Edmundian Orogeny, the 930–750 Ma Kuparr Tectonic Event and the c. 570 Ma Mulka Tectonic Event.

Sample descriptions

This study includes samples collected during field campaigns from 2014–2016 and samples requested from the GSWA. Links to petrographic reports available from the GSWA are listed in Appendix Table 1A. Rutile was analysed by laser ablation split stream inductively coupled plasma mass spectrometry (LASS-ICPMS) in a total of 23 samples. The list of units analysed includes (from oldest to youngest): the 2240–2125 Ma Moogie Metamorphics (GSWA 184160, 184161, 187403, 144898 and 216806); the 1840–1810 Ma Leake Spring Metamorphics (GSWA 190607 and 190608); the 1820–1775 Ma Moorarie Supersuite (samples DP14-GP05, DP14-GP06, DP14-GP07 and GSWA 185950, 188975 and 216818); the 1760–1680 Ma Pooranoo Metamorphics (GSWA 168937 and 152526, Mount James Subgroup); the 1673–1455 Ma Edmund Group (GSWA 148972 from the Mount Augustus Sandstone, correlative of the basal Yilgatherra Formation at the base of Edmund Group); Edmund Group, Depositional Package 1 (GSWA 172241 and 148945); and Edmund Group, Depositional Package 4, Ullawarra Formation, (GSWA 148974). In addition, single samples were analysed from the 3352–1813 Ma Yarlarweelor Gneiss Complex (GSWA 135476), the 2758–2585 Ma Warrigal Gneiss (GSWA 44617), the 2014–1920 Ma Bryah Group (GSWA 50859), and the 2005–1975 Ma Dalgaringa Supersuite (GSWA 70747). Sample localities are shown in Figure 2, with the exception of those for GSWA 135476 and 50859, which are located farther to the east.

2240–2125 Ma Moogie Metamorphics

GSWA 184160

This sample is a psammitic schist from the Paleoproterozoic Mumba Psammite component of the Moogie Metamorphics that are intercalated with the Halfway Gneiss within the Mooloo Zone (Fig. 2). It is a weakly foliated, quartz-rich metasedimentary rock that has been retrogressed to a chlorite-bearing assemblage. The foliation is defined by chlorite laths, and oriented and deformed quartz aggregates with approximately 70–75% quartz, 25% chlorite and trace rutile, zircon, apatite and Fe-oxide. Rutile usually occurs as elongate grains within foliated chlorite (Fig. 3a,b) and is mostly concordant to the foliation. Minor biotite and muscovite flakes are present within chlorite and suggest likely replacement of biotite by chlorite-bearing assemblages during retrogression. Locally, elongate rutile grains are folded and deformed (Fig. 3b), perhaps suggesting the growth of rutile before the development of foliation and retrogression during chlorite formation.

GSWA 184161

This sample is a quartzofeldspathic migmatite and was collected approximately 20 km to the southeast of GSWA 184160 within the Paradise Zone (Fig. 2). This migmatite is a part of the Mumba Psammite unit of the Moogie Metamorphics. The sample is foliated with the foliation defined by fine-grained chloritoid and quartz aggregates (Fig. 3c). Quartz is completely recrystallized and consists of interlocking subhedral to euhedral grains (~300 μm to 1 mm in size), with a decrease in quartz grain size (~50–200 μm) in chloritoid-rich layers. Chloritoid typically forms fine microgranular prismatic intergrowths with muscovite, suggesting contemporaneous growth. Rutile forms tan-brown crystals of various shapes and sizes (up to 300 μm), typically anhedral and commonly occurring within the melanocratic layers rich in chloritoid and muscovite. Locally, rutile is euhedral and contains visible

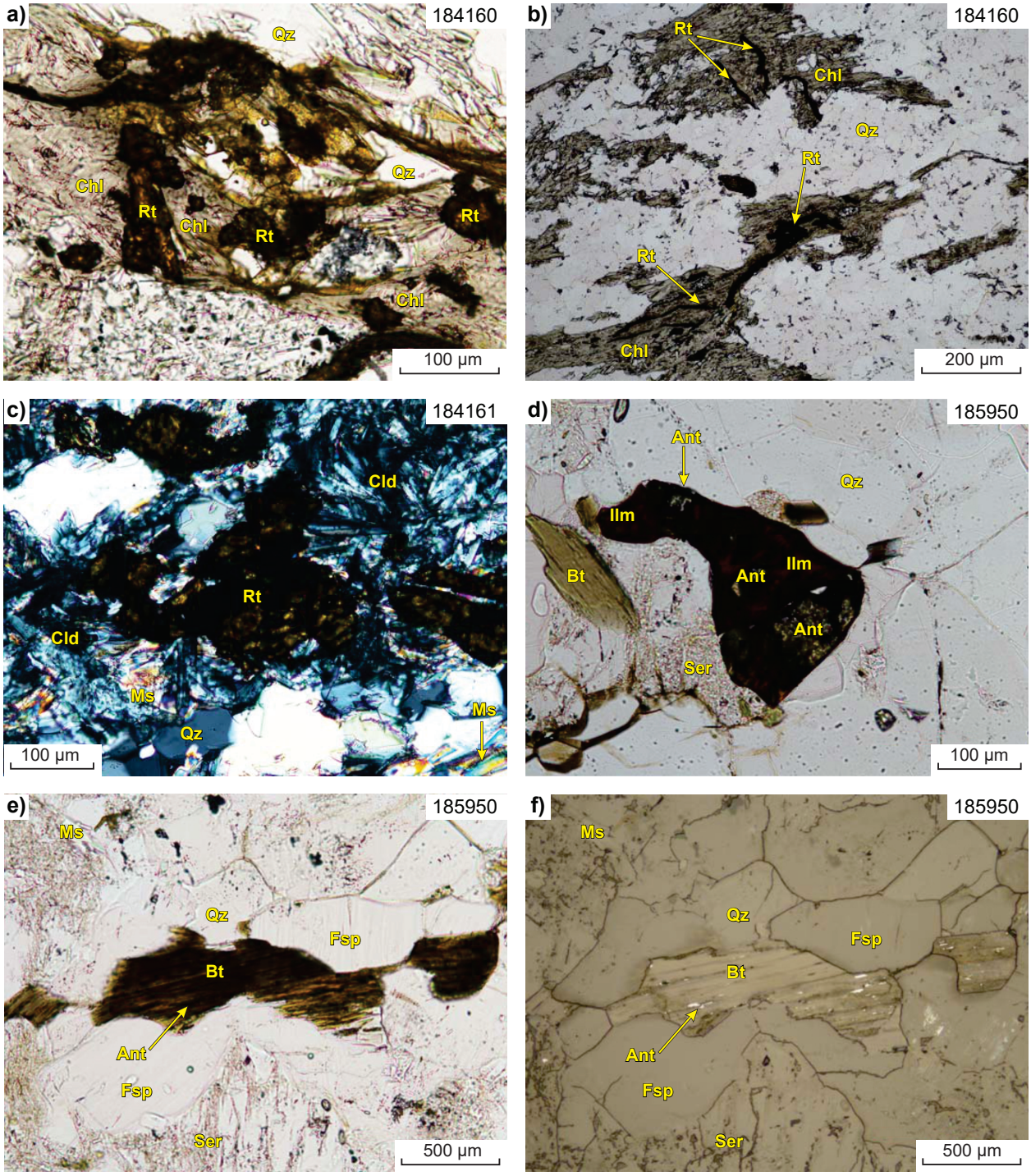

Figure 3. **Optical images of the Moogie Metamorphics and Moorarie Supersuite samples: a) GSWA 184160 – rutile grains in a chlorite–quartz-rich matrix, PPL; b) GSWA 184160 – elongate rutile grains occurring in association with chlorite, PPL; c) GSWA 184161 – large rutile grains in association with laths of chloritoid and quartz, XPL; d) GSWA 185950 – euhedral anatase grains fully enclosed and rimmed by anhedral ilmenite in a quartz–feldspar–biotite-rich matrix, PPL; e) GSWA 185950 – elongate anatase grains exsolved along biotite cleavage, PPL; f) GSWA 185950 – reflected light. Mineral abbreviations after Whitney and Evans (2010). Abbreviations: Ant, anatase; Bt, biotite; Cld, chloritoid; Chl, chlorite; Ilm, ilmenite; Fsp, feldspar; Qz, quartz; Ms, muscovite; Rt, rutile. These abbreviations are also used in subsequent images (Figs 4, 6)**

(100) and (010) crystal faces; whereas, in other places, it displays a porous texture (POR) defined by microgranular aggregates of rutile. Abundant zircon and apatite are also present in the sample. Within the thin section, no primary phase assemblages have been observed. However, field relationships suggest the former presence of garnet and staurolite porphyroblasts with internal fabrics defined by quartz inclusions along with sillimanite, quartz and biotite (Johnson et al., 2011b).

GSWA 187403

This sample is a quartzite from the Mumba Psammite unit of the Moogie Metamorphics and is located within the Mutherbukin Zone (Fig. 2). The entire sample was crushed for mineral separation, thus a petrographic report is not available.

GSWA 144898

This sample is a quartz–muscovite–chloritoid schist. The foliation is defined by orientation of polygonal quartz-rich domains, and partially by aligned muscovite. The green–blue pleochroic chloritoid is randomly oriented and crosscuts muscovite. Rutile occurs in irregular, fine-grained (10–50 µm) aggregates, intergrown with Fe-oxide (hematite) and quartz.

GSWA 216806

This sample is a weakly foliated quartzite with minor muscovite. The quartz has a polygonal texture. The sample also contains trace rutile, zircon, apatite, Fe-oxide and round sulfide grains. SEM observations have also revealed the presence of micron-scale native gold. Rutile occurs as subhedral to euhedral elongate grains, up to 200–300 µm in size. Small (<5 µm) sulfide grains are mostly composed of pyrite and pyrrhotite.

1840–1810 Ma Leake Spring Metamorphics

GSWA 190607 and 190608

These samples are pelitic gneisses composed predominantly of quartz, cordierite, fibrolite, chlorite, green biotite, and feldspar. Muscovite, rutile and zircon are present as accessories. Quartz is polygonal, and biotite is mostly randomly oriented and interstitial to other major components. Large (up to 1.5 mm) elongate cordierite grains contain inclusions of biotite, quartz, rutile and zircon grains with typical pleochroic haloes. Cordierite rims are commonly embayed and replaced by fibrolite–chlorite intergrowths. Rutile occurs as elongate prismatic, euhedral grains up to 500 µm in size and, in some cases, rimmed by ilmenite. In backscatter electron (BSE) images, rutile has homogenous brightness, and no zoning was observed.

1820–1775 Ma Moorarie Supersuite

GSWA 185950

This sample is a gneissic granite from the Moorarie Supersuite and is located within the Mutherbukin Zone (Fig. 2). The mineral assemblage consists of 50–55% microcline, ~35–40% quartz, ~5% biotite and <1% garnet, plus trace ilmenite, anatase, zircon, apatite and muscovite. Quartz and microcline are generally very fine grained (<1 mm), although large quartz grains with undulose extinction suggest deformation and recrystallization. Inclusions of biotite and quartz are present within garnet, suggesting prograde growth of garnet under amphibolite-facies conditions. Anatase typically occurs as euhedral to anhedral grains, either completely enclosed within ilmenite or rimmed by it (Fig. 3d). Both ilmenite and anatase commonly occur as overgrowths on biotite along with anatase needles that are parallel to the biotite cleavage, perhaps suggesting exsolution textures (Fig. 3e,f). Microcline grains show sericitic alteration, with coarse-grained muscovite laths present in places. The predominant TiO_2 phase in this sample is anatase, with minor brookite present in the heavy mineral separates but not observed in thin section, so its textural relationship with the surrounding mineral phases is not known.

GSWA 188975

This sample is a biotite gneiss from the Moorarie Supersuite located within the Mooloo Zone (Fig. 2). The rock is weakly foliated with the foliation defined by biotite flakes. The primary mineral assemblage consists of quartz (~40%), plagioclase (~40%), biotite (~10–15%), microcline (~2–5%), muscovite (~1%) and accessory zircon, sericite, carbonate, opaque oxides, rutile and titanite. Plagioclase is phenocrystic and surrounded by fine-grained quartz and biotite aggregates, with textures suggesting rotation of plagioclase crystals in a quartz–biotite-rich matrix. Quartz is coarser grained away from the darker biotite-rich bands and becomes progressively finer towards the 'shear' bands and in 'shadow' zones around feldspar phenocrysts (Fig. 4a). The foliation shows evidence of S–C kinematic fabric defined by biotite-rich layers. Feldspars are commonly altered to sericite and muscovite. Although rutile was present in the heavy mineral separates, no rutile was observed in thin section.

DP14-GP05, DP14-GP06, DP14-GP07

Samples DP14-GP05, DP14-GP06 and DP14-GP07 were collected from the Limejuice Zone (Fig. 2) where significant molybdenum mineralization and Cu, Au, W and U anomalies were discovered at the Minnie Springs Prospect. Molybdenum mineralization occurs as disseminated molybdenite and pyrite within alkali granites (sampled here), and as molybdenite within quartz-rich veinlets (Pirajno et al., 2008). Rhenium–osmium (Re–Os)

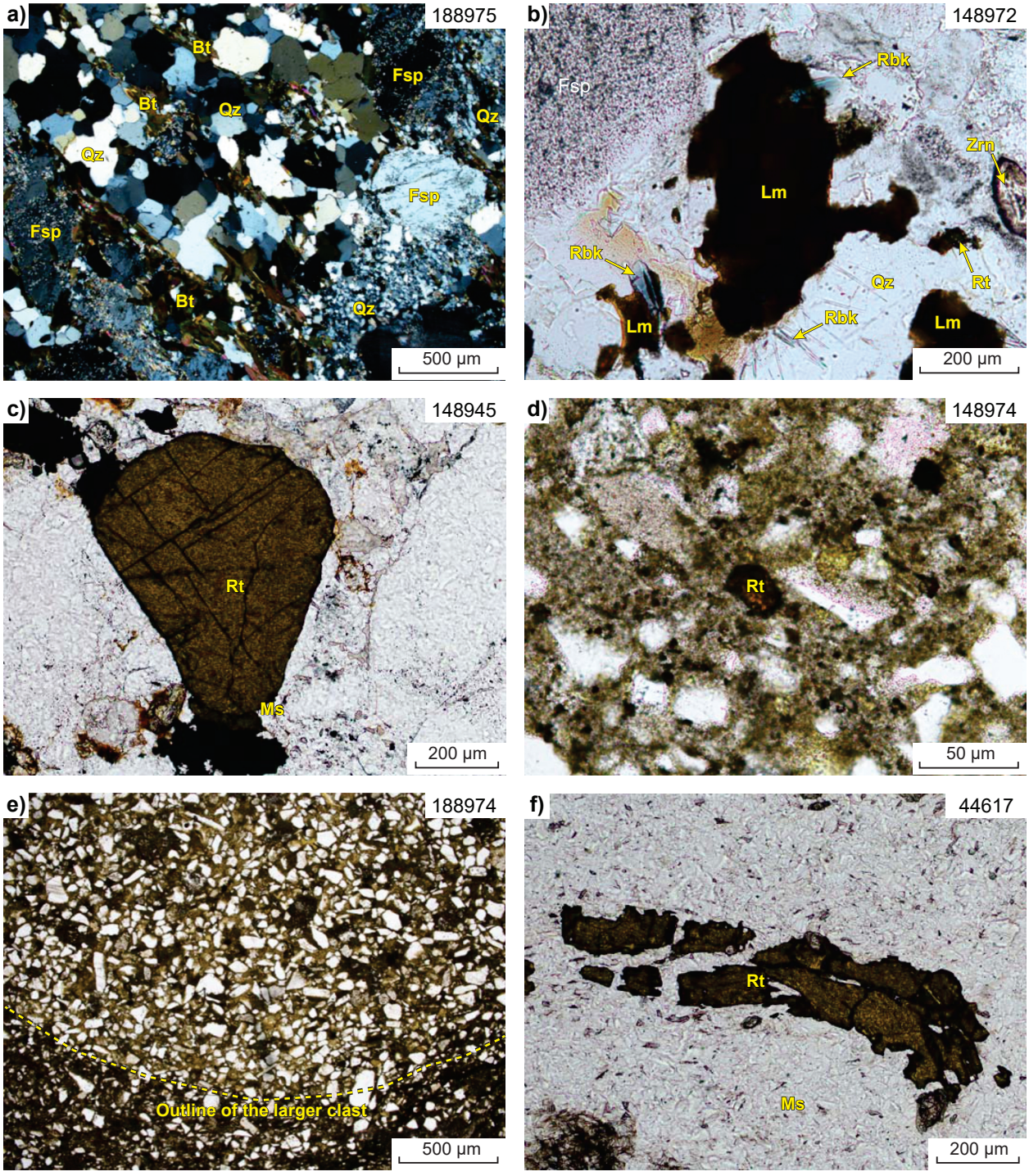

Figure 4. **Optical images of Moorarie Supersuite and Edmund Group samples: a) GSWA 188975 – biotite-rich bands defining the foliation along with a decrease in quartz grain size within the foliation bands and in pressure shadows of sericitized feldspar phenocrysts, XPL; b) GSWA 148972 – large anhedral limonite grains with euhedral riebeckite grains radiating outwards and into the surrounding quartz grains. Small rutile grain aggregates are present near the limonite rims, PPL; c) GSWA 148945 – a larger sericite–chlorite-rich clast with coarser grained quartz within a finer grained clay-rich siltstone, PPL; d) GSWA 148974 – rutile grain within a clay-rich matrix; e) round detrital rutile; f) GSWA 44617 – rutile aggregate in muscovite. Mineral abbreviations after Whitney and Evans (2010)**

dating of disseminated molybdenite within alkali granites yielded an age of 1773 ± 6 Ma, whereas molybdenite hosted in quartz veins yielded a younger age of 726 ± 11 Ma (Sheppard et al., 2010b; GSWA unpublished data). The samples were collected from the outcrops within the Minnie Springs exploration prospect. They are leucocratic granitic rocks containing perthitic K-feldspar (50–70%), quartz (25–40%), muscovite (1–5%), minor albite and accessory TiO_2, xenotime, monazite, allanite, pyrite and zircon. Samples DP14-GP05 and DP14-GP06 are medium grained, with euhedral quartz and perthitic K-feldspar. A strong fabric defined by sericite and microgranular quartz in sample DP14-GP07 suggests a higher degree of deformation with respect to DP14-GP05 and DP14-GP06. TiO_2 is interstitial and is commonly found at the margins of K-feldspar and quartz grains, as well as completely enclosed within quartz grains. In addition, TiO_2 is also present intergrown with pyrite and phosphate minerals (monazite and xenotime).

1760–1680 Ma Pooranoo Metamorphics

GSWA 168937

GSWA 168937 is a metasandstone from the Mount James Formation of the Pooranoo Metamorphics, and is located in the Paradise Zone (Fig. 2). Although the thin section was unavailable, there is a petrographic report in the GSWA Geochronology Record (Nelson, 2001). The mineral assemblage includes ~97–98% coarse-grained quartz (recrystallized to form quartzite) with minor muscovite (2–3%) and accessory tourmaline, zircon and rutile. Rutile is commonly present as disseminated, small (≤0.3 mm) aggregates, typically forming along quartz grain margins. Traces of fine-grained tourmaline occur with trails of minute fluid inclusions in quartz grains (Nelson, 2001).

GSWA 152526

GSWA 152526 is a fine-grained (<1 mm), well-foliated, quartz–muscovite metasedimentary rock from the Mount James Formation. The foliation is marked by muscovite and quartz-rich domains. Quartz has a granoblastic texture. Rutile forms foliation-parallel aggregates of anhedral, brown, semi-transparent grains. In several cases, rutile grains are intergrown with euhedral to anhedral Fe-oxide grains.

1679–1610 Ma Mount Augustus Sandstone

GSWA148972

This sample is a coarse-grained sandstone from the Mount Augustus Sandstone (Fig. 2). The sandstone largely consists of quartz grains (60–65%), orthoclase (30–35%), limonite (1–2%), riebeckite (<1%) and trace rutile, zircon and minor biotite (Fig. 4b). The quartz and feldspar grains are rounded to subrounded and poorly to moderately sorted. Grain boundaries between quartz and feldspar are recrystallized with interstitial limonite and clay minerals. Limonite locally has a cubic shape suggesting perhaps replacement of pyrite grains. Riebeckite forms randomly oriented elongate prisms and needles, and appears to be a secondary mineral as it grows across all the mineral phases and commonly occurs in association with limonite grains and, occasionally, radial growths around it (Figs 4b). Feldspars commonly contain opaque micro-inclusions.

1673–1455 Ma Edmund Group

GSWA 172241 and 148945, Depositional Package 1

GSWA 172241 is an altered quartz–amphibole–K-feldspar sedimentary rock. Green pleochroic amphibole forms randomly oriented elongate prisms. Although local alignment of amphibole can be observed in sub-mm-scale domains, no foliation is visible in the rock at the thin section scale. Carbonate, rutile and Fe-oxide occur as accessory minerals. Quartz has a granoblastic texture. Rutile is mostly anhedral and contains abundant inclusions of quartz and amphibole. Ilmenite inclusions oriented at ~60° are present in some rutile grains.

GSWA 148945 is a quartz-rich sandstone that grades from fine-grained, clast-supported conglomerate to sandstone. The mineral assemblage is characterized by quartz grains (98%) and very minor alkali feldspar, hematite with accessory zircon, rutile, apatite and monazite. The quartz grains are subrounded to rounded, with margins of the quartz grains, along with interstitial domains, filled by microgranular quartz. Thin (~1 mm) layers of heavy minerals define the laminations in the sedimentary rock. The heavy mineral layers are characterized by higher proportions of hematite (intergrown with rutile), zircon and monazite. Hematite–rutile intergrowths in these layers display exsolution features, with preferred orientations of microgranular rutile with 60° angles between the C-axes and the prisms. Rutile that occurs in association with hematite is typically zoned under BSE (oscillatory to patchy zonation), with variation in brightness due to higher concentrations of Fe, Nb and W. These rutile grains differ from detrital grains (only a single grain was analysed), that are well-rounded and homogeneous under optical microscope and SEM. The single detrital grain is large enough (up to 700 µm) to allow for multiple analyses to be carried out from rim to core (Fig. 4c).

GSWA 148974, Depositional Package 4, Ullawarra Formation (Curran Member)

This sample is a lithic sandstone from the upper part of the Edmund Group (Ullawarra Formation), located at the northern margin of the Edmund Group (Fig. 2). The sandstone is a fine-grained, poorly sorted, polymictic sandstone composed of 50% quartz, 10–15% chert, 5% microcline, 1–2% plagioclase, 1–5% lithic grains, 1–2% limonite and trace rutile and zircon. The sample is matrix-supported with a clay-rich matrix and largely angular to subrounded grains (Fig. 4d). A larger clast within the sandstone contains coarser grained quartz (200–300 µm),

chert, plagioclase and microcline embedded in a sericite-rich matrix (Fig. 4e). Rutile grains are typically red-brown to tan-brown in colour, subrounded to angular and are commonly found within the clay-rich matrix (Fig. 4d), with one rutile grain present in the sericite-rich clast. Thin veins rich in quartz and limonite cut across the sandstone.

Other samples

GSWA 44617, 2758–2585 Ma Warrigal Gneiss

GSWA 44617 is a quartz–muscovite schist and forms a part of the Warrigal Gneiss unit in the Errabiddy Shear Zone to the south of the Gascoyne Province (Fig. 2). Quartz (60%) is commonly coarse grained (up to 1 cm), deformed and elongate parallel to the main tectonic foliation defined by fine-grained muscovite (~40%), with accessory rutile and zircon. Muscovite-rich veins cut across quartz grains. Rutile is commonly present in association with muscovite (Fig. 4f) and is parallel to the main foliation. Occasionally, large muscovite grains (up to 3 mm) form elongate laths subparallel to the main foliation and are commonly replaced by very fine-grained sericite, suggesting two generations of muscovite grains. The precursor is likely a felsic igneous rock.

GSWA 50859, 2014–1920 Ma Bryah Group

GSWA 50859 is a fine-grained (<1 mm) ultramafic rock from the Bryah Group. The main assemblage consists of talc (60–65%), serpentine (35–40%), with accessory rutile, barite, forsterite, augite, apatite and titanite (as small inclusions in rutile). Talc is typically fibrous, with serpentine typically replacing forsterite. All rutile grains display well-defined twins, both under optical microscope and SEM and can be up to 2 mm long. The majority of the rutile grains are subhedral to euhedral, up to 200 µm in size, and can be elongate with aspect ratios of up to 5:1. Rutile grains are oikocrystic and contain fine-grained (<5 µm) inclusions of titanite, apatite and augite (most abundant). There is no recognizable tectonic fabric in the sample.

GSWA 70747, 2005–1975 Ma Dalgaringa Supersuite

GSWA 70747 is a metasiltstone unit within the Dalgaringa Supersuite at the southern margin of the Gascoyne Province. The main assemblage consists of quartz (40–45%) and chlorite (55–60%), with trace garnet and accessory rutile and zircon. Microgranular quartz (0.5 – 1 mm) and chlorite define the foliation in the rock. Rutile grains are largely subhedral to anhedral and elongate, and typically occur within chlorite-rich domains. They are commonly twinned, brown in colour and can be up to 500 µm in size. The long axes of rutile grains are parallel to the foliation, suggesting they formed contemporaneously with the main fabric-forming event.

Analytical methods

Heavy mineral separates and thin sections for the selected samples were obtained from the GSWA. Links to sample petrographic reports for samples with existing zircon U–Pb data are given in the appendices (Tables 1A and 2A respectively). Rutile (as well as anatase and brookite) grains were handpicked and mounted in epoxy resin discs. The grains were polished and imaged on the Tescan MIRA3 field emission scanning electron microscope (FE-SEM) using BSE, energy dispersive spectrometry (EDS) and electron backscatter diffraction (EBSD) detectors at the Microscopy and Microanalysis Facility, John de Laeter Centre, Curtin University. The SEM, BSE and EDS imaging and analysis were carried out at 20 kV accelerating voltage, 12–27 nm spot size and 14–16 mm working distance. The grains typically vary in texture, brightness in BSE and size, with some grains up to 600 µm. U–Pb geochronology and trace element geochemistry analysis of TiO_2 grains were carried out simultaneously using the laser ablation split stream (LASS) system at the University of California, Santa Barbara (UCSB), as well as at the John de Laeter Centre.

Laser ablation split stream (LASS) ICP mass spectrometry

The LASS analytical set-up at UCSB consists of a Photon Machines 193 nm ArF Excimer laser coupled to a Nu Plasma multicollector inductively coupled plasma mass spectrometer (MC-ICPMS) and Agilent 7700x quadrupole ICPMS. The detailed outline of the LASS instrumentation and techniques is given in Kylander-Clark et al. (2013). The spot size used was 25–35 µm with laser fluence between 3–5 mJ/cm^3, laser pulse of ~100 nm and a repetition rate of 4 Hz. Analyses were conducted over 20-second ablation periods with approximately 17 washout periods, during which the background signal was collected. The LASS instrumentation at the John de Laeter Centre consists of a Resonetics S-155-LR 193 nm excimer laser ablation system coupled to an Agilent 7700x quadrupole ICPMS (trace element geochemistry) and a Nu Plasma II MC-ICPMS (U–Pb geochronology). Rutile grains were analysed in situ in thin sections with a beam diameter of ~23 µm, repetition rate of 5 Hz and laser fluence of ~3 mJ/cm^2 (independently measured). The total acquisition time was 75 seconds, including 40 seconds of background signal collection, 20-second sample ablation and 15-second washout period. During each session, sample surfaces were cleaned by firing two laser shots before each analysis in order to avoid surface contamination. The ablated material was carried by helium gas and subsequently mixed with argon before input into the plasma. The ablation stream is split two ways upon mixing with argon and directed into the two mass spectrometers.

During both analytical sessions, the set-up for carrying out U–Pb isotope measurements was kept the same to ensure consistency between the two laboratories. The U–Pb measurements were carried out on the MC-ICPMS consisting of 12 Faraday cups equipped with 1011-ohm resistors and four ETP discrete-dynode ion counters.

The ^{238}U and ^{232}Th were measured using the Faraday cups and the ^{206}Pb, ^{207}Pb, ^{208}Pb and ^{204}Pb + Hg were measured on the ion counters. Post-acquisition data processing, including calculations of U–Pb isotope ratios and their propagated uncertainties, were carried out using Iolite software (Paton et al., 2010). The ages are reported at 95% confidence level. Concordant values are taken as being <5% discordant. Precision on individual analyses is variable and largely depends on the concentration of U, Pb and Th, with lower concentrations yielding predictably lower precision. Mass bias and instrumental drift corrections were carried out using the common standard-sample-standard bracketing method, with a typical run consisting of a suite of NIST glass, matrix-matched internal standards and multiple rutile reference materials at the beginning and end of the run, with internal standards (Rutile R10) analysed throughout the run, typically after nine analyses of sample unknowns. Up to 120 unknowns were commonly analysed in one run and the entire suite of samples was analysed during continuous acquisition over three days. To monitor the accuracy of the LASS method, multiple rutile reference materials were analysed during the entire analytical session. The reference materials include the matrix-matched internal standard used for standard-sample bracketing rutile R10 from Gjerstad, in southern Norway (Luvizotto et al., 2009) and reference standards treated as unknowns during the analytical session to test the accuracy of the method, including Sugluk-4 (SUG) from the Trans-Hudson Orogen (Canada), PCA-S207 from the eastern region of Lake Athabasca (Canada), rutile from weakly retrogressed HP eclogite (9826J) in the northwestern part of Gurskøy, Norway (Kylander-Clark, 2008), R13 and R19 (Luvizotto et al., 2009; Zack et al., 2011) and Windmill Hill Quartzite (WHQ), from the Jimperding metamorphic belt in Western Australia (Clark et al., 2000; Taylor et al., 2012). The results of U–Pb analyses of the samples and the calculated temperatures are listed in Appendix Table 2A. The results of the U–Pb dating of rutile reference materials are shown in Appendix Table 3A and Appendix Figure 1A and 1B. No common-Pb correction was applied. The results are typically within 2% of accepted values for the majority of the standards analysed.

Trace element concentrations for the reference materials and samples were measured simultaneously on the Agilent 7700x quadrupole ICPMS. US National Institute of Standards and Technology (NIST) and Basalt, Hawaiian Volcanic Observatory (BHVO) glasses were used as a calibration standard for concentration determination and to correct for any instrumental drift, mass bias and elemental fractionation. Internal standardization was done stoichiometrically assuming 100% TiO_2 (i.e. 59.94% Ti). Rutile standard R10 was monitored within each run along with the four other reference materials (PCA, SUG, 9826J and WHQ). Measured trace elements include ^{49}Ti (internal standard), ^{27}Al, *^{28}Si*, *^{43}Ca*, ^{51}V, ^{52}Cr, ^{55}Mn, ^{56}Fe, *^{59}Co*, ^{60}Ni, ^{63}Cu, ^{90}Zr, ^{93}Nb, ^{95}Mo, ^{118}Sn, ^{121}Sb, ^{178}Hf, ^{181}Ta and ^{182}W (elements in italics were only measured at the Curtin University LASS laboratory). Post-acquisition data processing was carried out using the function trace element internal standard (IS) in Iolite software (Paton et al., 2010) along with concentration calculations using the normalized sensitivity equations of Longerich et al. (1996). Analyses where inclusions of silicate minerals (mostly quartz) and/or zircon, apatite, monazite and ilmenite were observed under BSE, or suspected based on high Si (>0.5 wt%) and Zr (>1 wt%), were filtered out of the dataset. The precision on individual analyses is dependent on the spot size (approximately 1.2% better on average for 35 µm spot size) and the concentration of analyte element in the sample. Typical precision on individual analyses obtained during the analytical session is >5% for elements <10 ppm, 3–5% for elements between 10–100 ppm and <3% for elements >100 ppm. Uncertainties on individual spot measurements are cited at 2σ level and include the internal uncertainties associated with counting statistics only. A summary of the typical trace element values for the standards is given in Appendix Table 4A with the full trace element dataset for the standards and samples given in Appendix Tables 5A and 6A, respectively. During the analytical session, standards were re-polished exposing the different parts of grains, thus slightly different trace element concentrations were obtained for certain elements (mainly Al, Cu, Nb, Sn and Sb, Appendix Figure 2A). The trace element concentrations within the standard R10 also varied from rim to core (e.g. Cu, Cr, Fe, Nb and V) and along certain grain orientations (e.g. W and Ta, see Appendix Figure 2B) showing trace element heterogeneity within the R10 standard, similar to those reported by Luvizotto et al. (2009).

Electron backscatter diffraction (EBSD) mapping

Electron backscatter diffraction (EBSD) mapping and spot analysis was carried out to determine the different types of TiO_2 polymorphs and to detect any intergrain orientation variations. Before analysis, grains were polished for 3–4 hours with a 0.06 mm colloidal silica in a NaOH solution (pH = 10) on a VIBROMET 2 polisher. All of the data was collected on the Tescan MIRA3 field emission scanning electron microscope (FE-SEM) at the John de Laeter Centre.

Data acquisition and processing were carried out using Oxford Instruments Aztec 2.4 and CHANNEL 5.12 software (detailed analytical methods are described by Reddy et al., 2007). The operating conditions included 20 kV accelerating voltage, 19–22 mm working distance and 27 nm spot size. Crystallographic parameters and occupancy data used to create 'match units' for anatase, brookite and rutile electron backscatter pattern (EBSP) indexing were obtained from the American Mineralogist database (Horn et al., 1972; Meagher and Lager, 1979; Swope et al., 1995). The theoretically generated EBSP patterns for anatase, brookite and rutile are different and should, therefore, effectively discriminate between the three TiO_2 polymorphs. The accuracy of the EBSD method is assessed by the mean angular deviation (MAD) that measures the 'closeness of fit' between the theoretical and empirically obtained EBSP patterns, with values >1.0° commonly regarded as 'poor quality'.

Data are presented as a series of maps showing TiO_2 phase distribution and crystallographic orientation information. Before generating EBSD maps, all data were noise-reduced using a 'wildspike' correction, followed by five-neighbour zero solution extrapolation. Maps showing phase relationships and microstructural information were produced using the CHANNEL 5.12

software (Tango module). Different colours were used to represent all identified phases on phase maps. Individual grain misorientation maps were created using a 'texture' component in the Tango module with changes in colour of the rainbow spectrum representing grain misorientation relative to a user-defined orientation. Variable map sizes were obtained due to the variation in grain size, with a typical step size for each map between 0.15 and 2 μm.

Results

Rutile texture descriptions and polymorph distinction (EBSD)

2240–2125 Ma
Moogie Metamorphics

The main TiO_2 phase from the Mumba Psammite unit of the Moogie Metamorphics (GSWA 184160 and 184161) is rutile as confirmed by EBSD analysis. Rutile grains from these samples display similar textural relationships, and are closely associated with chlorite and quartz bands that define the foliation. In thin section, rutile is commonly deformed and is parallel to the foliation. Biotite and muscovite are commonly replaced by chlorite, suggesting deformation of rutile and replacement of micas during retrogression to chlorite-bearing assemblages. BSE imaging of the rutile grains reveals largely homogenous, moderately bright and homogeneous (MBH) rutile grains that are closely intergrown with quartz and chlorite. Some grains are intergrown with feldspar and quartz resulting in trellis-type textures (Fig. 5a) akin to pseudomorphic textures after ilmenite (Janssen et al., 2010). The pole figures (Fig. 5a) reveal a structured relationship between the C-axes, with a common <010> axis and angles between C-axes around 60°, but ranging overall from 59 to 66°. Furthermore, the (101) twins are commonly observed in some rutile grains (Fig. 5b), with angles between the two C-axes equal to ~65° (Daneu et al., 2014).

GSWA 187403, also from the Mumba Psammite, contains rutile only as the main TiO_2 phase. The rutile textures and luminescence under BSE are quite variable, with the least bright, featureless rutile grains (MBH) occurring as individual, commonly euhedral, grains (Fig. 5c) as well as oscillatory zoned rims around moderately bright (MED) to bright (BRH) grains (Fig. 5d, grain R3gr14). This variability is consistent with detrital origin. Some rutile grains show oscillatory zoning with Fe-rich cores (approaching ilmenite compositions) and Fe-poor rims. Patchy brightness (PBH) is also commonly found in some grains with the brighter patches enriched in W and Nb (Fig. 5d, grain R3gr15).

Rutile in GSWA 144898 and 216806 mostly has homogenous, moderate brightness in SEM images. Faint zoning due to the crystal lattice and twin misorientation was observed in a few grains from both samples.

1840–1810 Ma
Leake Spring Metamorphics

GSWA 190607 and 190608

Rutile in GSWA 190607 and 190608 forms euhedral to subhedral prisms up to a few hundred microns long, in some cases forming aggregates. In BSE images, rutile is moderately bright and featureless. The textural features (sharp boundaries, euhedral habit) and the absence of zoning suggest that rutile is in equilibrium with the coexisting minerals.

1820–1775 Ma
Moorarie Supersuite

GSWA 185950 and 188975

GSWA 185950 and 188975 yielded all three TiO^2 phases (rutile, anatase and brookite), although they do not occur simultaneously in the same sample. In GSWA 188975, anatase and rutile are both present, whereas brookite is absent. They are both present as individual grains, although in many instances, anatase forms rims around rutile, suggesting replacement (Fig. 6a,b). Under BSE, both phases are moderately bright and featureless with a porous (POR) texture indicating possible volume loss (Fig. 6b). Both phases are also commonly intergrown with quartz. In GSWA 185950, anatase and brookite grains were observed in the grain mount (and only anatase in thin section) and occur only as individual grains with well-formed euhedral crystal habits (Fig. 6c). In BSE and secondary electron (SE) images, both anatase and brookite are moderately luminescent, with anatase grains commonly having uneven crystal surfaces, whereas brookite displays largely smooth surface textures (Fig. 6c).

Samples DP14-GP05, DP14-GP06, DP14-GP07 and GSWA 216818

Rutile grains from mineralized samples DP14-GP05, DP14-GP06 and DP14-GP07 are typically euhedral to anhedral, between 50–500 μm in size and show complex zoning under BSE that can be subdivided into four main types: 1) patchy and diffuse (Appendix Fig. 3a, grain I); 2) bright and undulose (predominantly in sample DP14-GP06, Appendix Fig. 3a, grain II); 3) oscillatory zoned and parallel to grain margins (Appendix Fig. 3a, grain III); and 4) sharp, nonparallel to grain margins (step-zonation, Appendix Fig. 3a, grain IV).

EDS mapping of the grains shows that BSE-bright zones are enriched in Nb and Fe (Appendix Fig. 3b). Rutile grains in sample DP14-GP06 (and to a lesser degree DP14-GP05) display ragged margins, particularly in zones of intense fracturing (Appendix Fig. 3a, grain II). Mobilization of Zr, Y, P, Nb, Ta and Ti along fractures resulted in formation of microgranular Nb–Ta-rich rutile, zircon and REE phosphates (xenotime and monazite) (Appendix Fig. 3a, grain II). Micro-inclusions (<1 μm) of Th-rich minerals

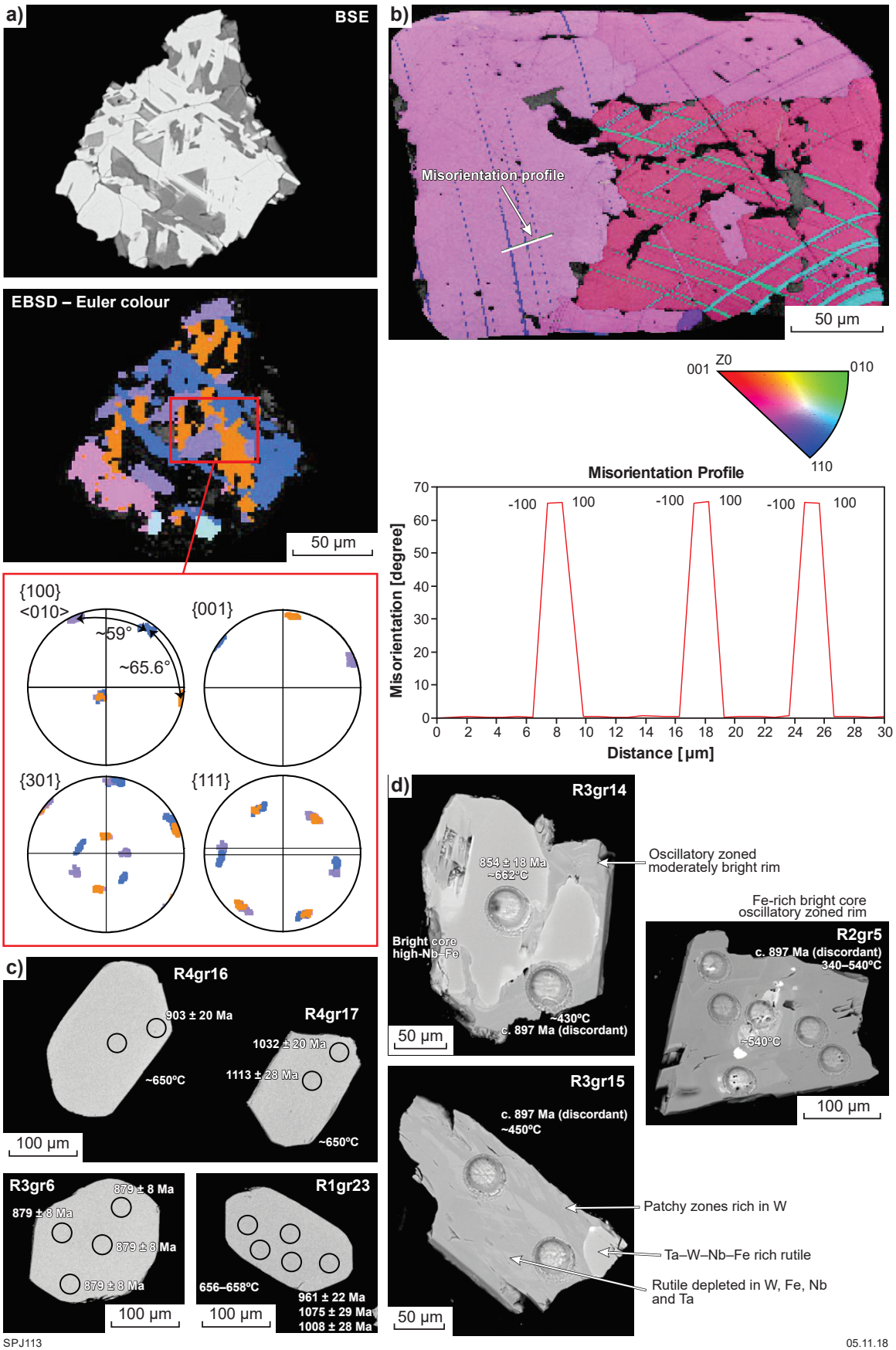

Figure 5. **BSE and EBSD rutile images of Moogie Metamorphics rutile grains: a) trellis-type texture of rutile grains intergrown with feldspar and quartz. Lower-hemisphere projections of the selected area showing orientations of different crystallographic planes and axes; b) rutile grain showing twins with inverse-pole colouring. Misorientation profile showing misorientation angles of ~65–66°, akin to ~114.4° (180–114.4 = 65.6°) misorientation angles of twins on (101) planes of Daneu et al. (2014); c) GSWA 187403 – euhedral MBH grains; d) GSWA 187403 – variable brightness of rutile grains under BSE and common variations in chemistry**

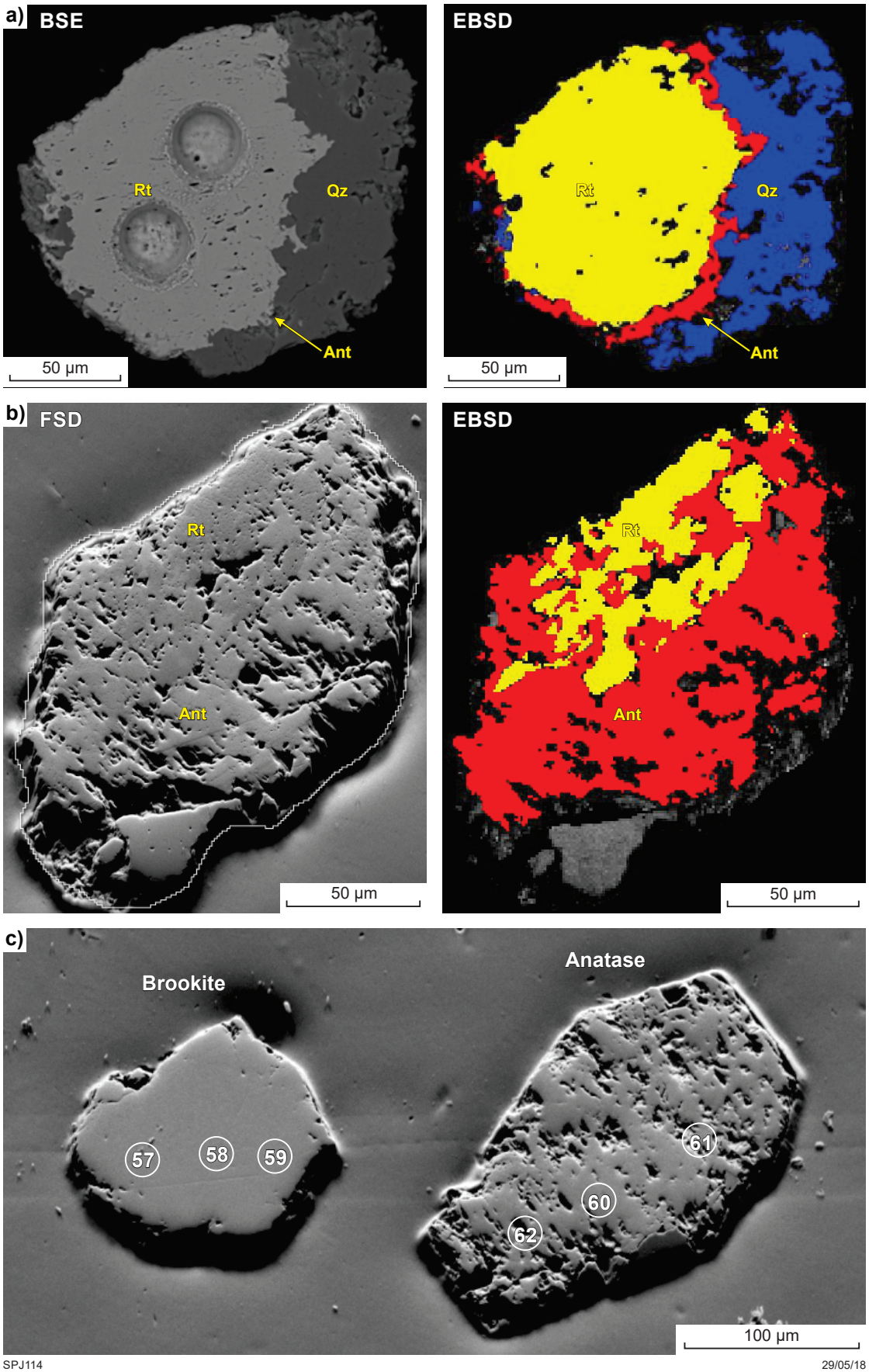

Figure 6. **BSE and EBSD images of TiO_2 phases in Moorarie Supersuite samples: a) GSWA 188975 – EBSD phase mapping reveals anatase rims forming around rutile, otherwise not detected by routine BSE imaging; b) Forward-scattered Electron Detector image (FSD – EBSD detector cameras) and EBSD phase mapping revealing rutile grains enclosed within anatase; c) anhedral brookite and euhedral anatase grains showing LASS spot locations**

(largely phosphates) are observed in some grains (sample DP14-GP07, Appendix Fig. 3a, grain V). Furthermore, coarse-grained (up to 250 µm) microgranular xenotime and monazite, along with minor zircon, are typically intergrown with rutile (Appendix Fig. 3a, grain VI). Irregularly shaped Sc-rich inclusions of manganocolumbite occur as inclusions in rutile (Appendix Fig. 3a, grain VII). Sulfide minerals (pyrite and chalcopyrite) were observed in a majority of the samples analysed, where they contain inclusions of, or are commonly intergrown with, rutile (Appendix Fig. 3a, grain VIII). Altered gabbro (GSWA 216818) contains anhedral rutile grains, up to 300 µm, typically rimmed by titanite.

Rutile grains from mineralized samples typically yield little to no internal grain misorientation in a majority of grains. A small number of grains yield misorientations of up to 7° near the grain margins (Appendix Fig. 3b). Attachment of individual rutile grains commonly occurs along (101) and (301) planes with grain misorientation angles at ~65° and ~55°, respectively (Appendix Fig. 3c), and <010> misorientation axes. The grain misorientation angles closely match the angles between the C-axes of individual rutile grains. Changes in brightness under BSE are largely independent of microstructure.

1760–1680 Ma Pooranoo Metamorphics

GSWA 168937 and 152526

In GSWA 168937 and 152526, rutile has grain sizes of up to 500 µm. Grains are commonly MBH textured, although many grains also have a porous (POR) texture. Grains are commonly intergrown with quartz and many of them contain micro-inclusions of zircon and monazite. The nonporous grain fraction is typically twinned along the (101) plane (Fig. 7a). Porous grains have a systematic orientation with three separate C-axes that are approximately at 60–65° from each other, rotating around a common <010> zone axis (Fig. 7b).

1679–1610 Ma Mount Augustus Sandstone

GSWA 148972

GSWA 148972 from the Mount Augustus Sandstone only contains rutile. Rutile grains are angular to prismatic with sizes ranging between 50 and 350 µm. Under BSE imaging, rutile grains have variable brightness with moderately bright featureless grains, patchy brightness with stripes of alternating bands or individual domains (PBH), with the brighter domains commonly characterized by small W and Nb peaks in the EDS spectrum (Fig. 8a). Some of the moderately bright grains also have a porous (POR) texture with three separate C-axis orientations around a common <010> zone axis similar to porous grains from GSWA 168937. Although some of the moderately bright to patchy grains have prismatic shapes, the porous rutile grains are typically anhedral and consist of aggregates of fine-grained rutile grains.

1673–1455 Ma Edmund Group

GSWA 172241 and 148945, Depositional Package 1

Rutile from GSWA 172241 forms aggregates of anhedral grains with ragged margins. Rutile cores contain abundant inclusions of needle-like amphibole and quartz, conferring a porous texture, with a decrease in the abundance of inclusions towards the rims (Fig. 8c). The abundance of inclusions in rutile suggests a metamorphic origin.

In GSWA 148945, rutile occurs as either inclusion-free, unzoned in BSE, rounded grains, of detrital origin, fine-grained (5–50 µm) aggregates forming exsolution features with hematite, or irregularly zoned, anhedral grains of up to 500 µm in size intergrown with hematite.

GSWA 148974, Depositional Package 4, Ullawarra Formation (Curran Member)

The main TiO_2 phase in Ullawarra Formation GSWA 148974 is rutile, with anatase forming thin rims (5–10 µm) around some rutile grains. Anatase could not be analysed due to size limitations on the laser spot size (25–35 µm). Rutile grains vary in size between 30 and 150 µm and are typically subrounded to angular and elongate (Fig. 8b). They are moderately bright and homogenous (MBH) in BSE brightness, with some containing inclusions of xenotime, zircon and ilmenite (Fig. 8b). Visible (101) twinning can be observed both in optical light and under the EBSD detector.

Other samples

GSWA 44517, 2758–2585 Ma Warrigal Gneiss

Rutile grains in Warrigal Gneiss GSWA 44617 are typically anhedral, unzoned under BSE with moderate brightness (MBH) and up to 550 µm in size. Rutile is typically closely associated with zircon, with zircon occurring either in contact with, or as inclusions in rutile, particularly along cracks. Zirconium mobility along the cracks in rutile, and the surrounding muscovite, can also be identified due to the increased brightness under BSE, as well as in the EDS spectra. Rutile is more abundant in the muscovite-rich zones.

GSWA 50859, 2014–1920 Ma Bryah Group

Rutile in Bryah Group GSWA 50859 forms anhedral crystals or elongate prisms up to 500 µm long. Abundant anhedral silicate inclusions are present in several rutile grains. Under BSE, rutile in this sample is featureless or has sharp planar (nonconcentric) brightness variations crosscutting whole grains corresponding to crystal lattice misorientations, typically along twin plane boundaries.

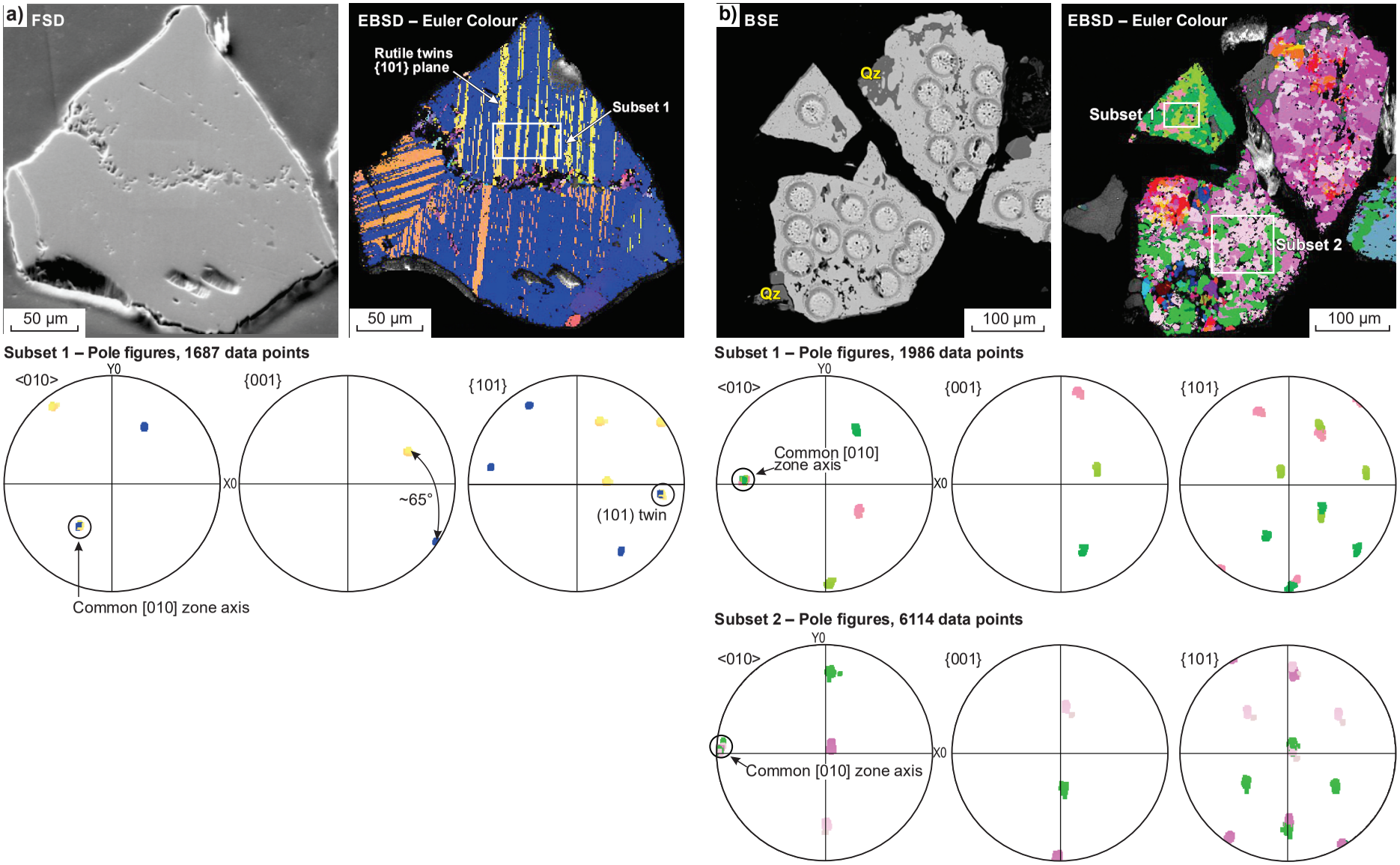

Figure 7. BSE and EBSD images of rutile in samples of Pooranoo Metamorphics and Edmund Group sedimentary rocks: a) EBSD mapping of MBH rutile grains revealing twins; lower hemisphere projections showing twins along a common (101) plane; b) BSE and EBSD mapping of porous (POR) textured rutile grains showing systematic orientation distribution of C-axes with a common [010] zone axis and (101) planes

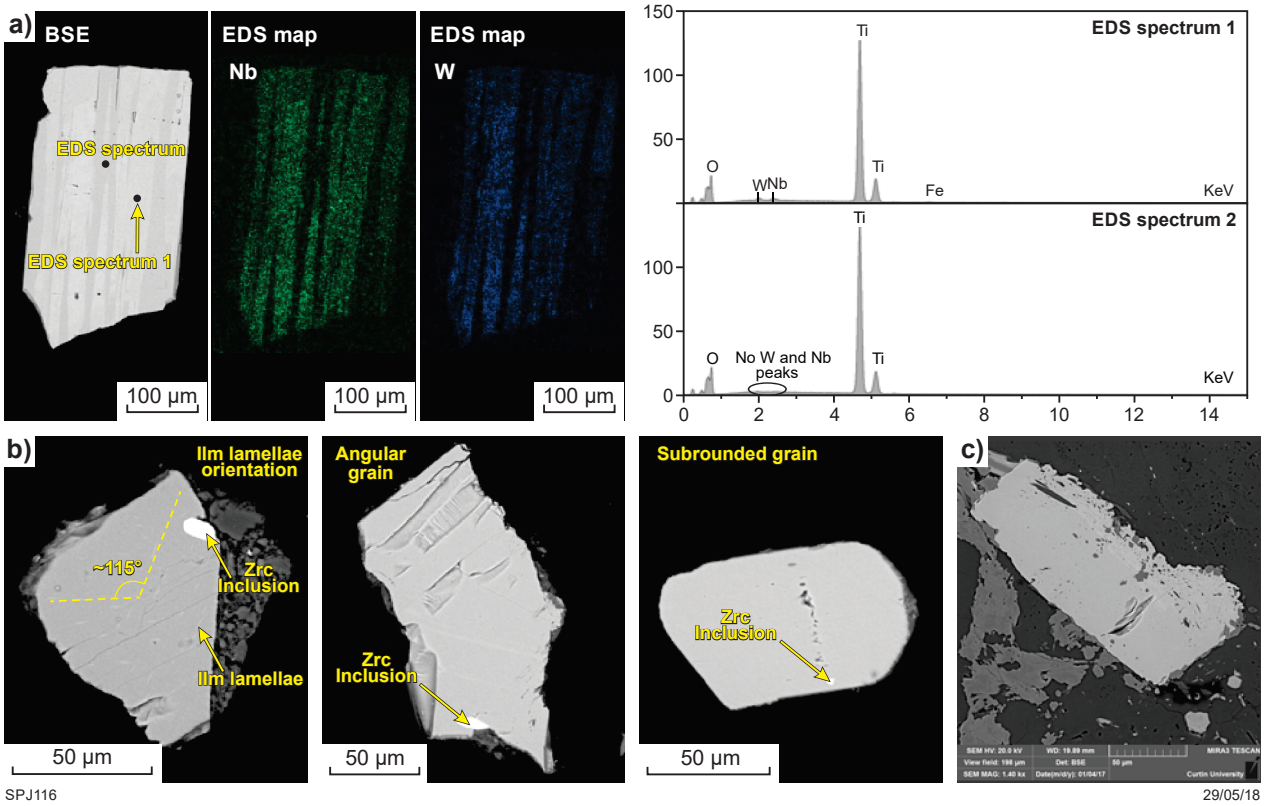

Figure 8. **BSE and EDS mapping of Edmund Group detrital rutile grains: a) variable brightness of patchy bright homogenous (PBH) rutile grains under BSE due to higher concentration of Nb and W in the grains with EDS spectra detecting Nb and W peaks in Nb-poor (darker) and Nb-rich (brighter) domains; b) BSE images showing oriented ilmenite lamellae in subrounded to angular rutile grains as well as inclusions of zircon (Zrc); c) GSWA 172241– poikilitic rutile**

GSWA 70747, 2005–1975 Ma Dalgaringa Supersuite

Rutile in Dalgaringa Supersuite GSWA 70747 forms euhedral to subhedral individual grains or fine anhedral aggregates occasionally up to 300–400 µm in size. Under BSE, rutile is mostly homogeneous. Sub-micrometre oriented ilmenite needles occur in a majority of grains, whereas some of the grains are deformed as evidenced by twin plane bending.

U–Pb geochronology

2240–2125 Ma Moogie Metamorphics

Rutile grains in GSWA 184160 and 184161 are quite similar with respect to their brightness and texture, consisting of typically MBH. Both samples show a high degree of discordance on the U–Pb Tera–Wasserburg plots (Fig. 9) that can be attributed to high proportions of common Pb, as well as low concentrations of uranium, largely between 0.48 and 15 ppm (average ~2 ppm). Linear regression through the discordant analyses of the two samples does not allow statistically reliable age determination, but yields lower intercepts of c. 1100 Ma (Fig. 9). The in situ rutile analyses in thin sections of the same samples re-analysed in February 2017 at the same laboratory yielded overlapping results. The high proportion of common Pb and the high mean square of weighted deviates (MSWD) values associated with discordia lines suggest the lower intercept ages could represent mixing of rutile grain ages reset during a common tectono-thermal event. Zirconium-in-rutile thermometer readings buffered in the presence of zircon and quartz yield indistinguishable temperatures of 396 ± 2°C and 397 ± 5°C for the two samples. Furthermore, textural relationships together with EBSD data suggest deformation of rutile grains in both samples during the formation of chlorite-bearing assemblages and breakdown of biotite. Previous U–Pb analyses of detrital zircons in GSWA 184160 indicated dates between c. 3165 and 2239 Ma, and metamorphic zircon rims gave dates of c. 1928 Ma (Wingate et al., 2010b). In GSWA 184161, U–Pb analyses of detrital zircons gave dates between c. 2743 and 2369 Ma, and metamorphic zircon rims gave a date of c. 1952 Ma (Kirkland et al., 2009).

Rutile from GSWA 216806 yielded a concordant age of 1890 ± 16 Ma (MSWD = 1.3). Zirconium thermometry indicates average temperatures of 674 ± 9°C. No zircons have been dated from this sample.

Rutile grains from GSWA 187403 yielded the greatest variety of textures and a large proportion of concordant analyses (Fig. 9). Concordant analyses range in $^{238}U/^{206}Pb$ ages dated between c. 1200 and 850 Ma, with the greatest peak on the probability density plot at c. 866 Ma (Fig. 10).

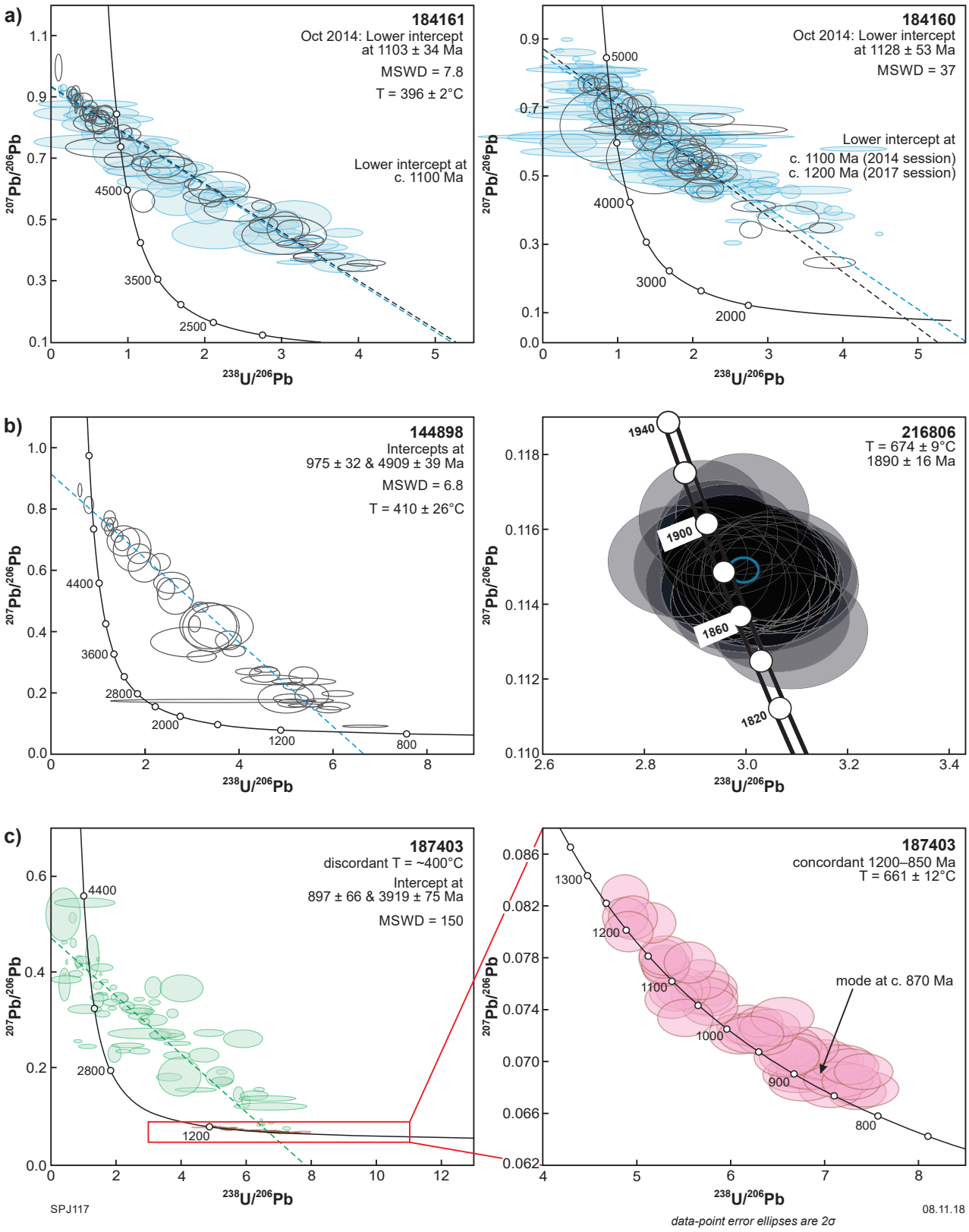

Figure 9. **U–Pb concordia plots and Zr-in-rutile temperatures for Moogie Metamorphics GSWA 184160, 184161, 144898, 216806 and 187403. Black and blue symbols for GSWA 148960 and 148961 indicate data from February 2017 and October 2014 analytical sessions, respectively. Green and red ellipses in GSWA 187403 represent discordant and concordant data points, respectively**

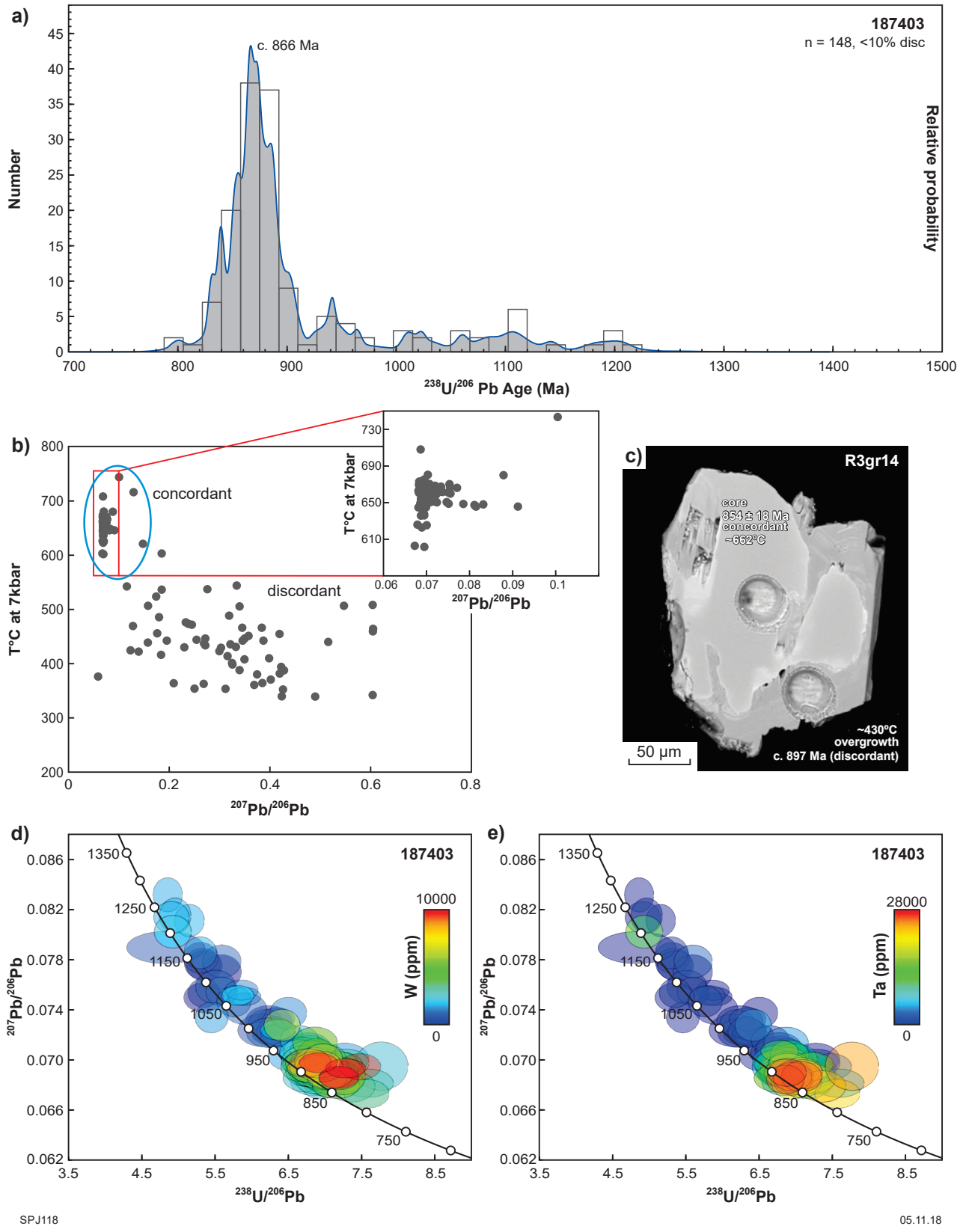

Figure 10. **Moogie Metamorphics (GSWA 187403) age probability density, Zr-in-rutile temperatures vs $^{207}Pb/^{206}Pb$, complex textures of rutile (BSE image) with temperature estimates and U–Pb concordia plots showing variation in W and Ta concentrations with age. The histogram shows the probability density plot for 148 analyses <10% discordant**

The older concordant analyses (between c. 866 and 1200 Ma) were obtained mostly from rutile grains with homogeneous and oscillatory zoned BSE textures, as well as rutile grains displaying patchy brightness. The bright rutile grains (BRH, Fig. 5d) yielded a majority of the younger dates (c. 866 Ma). Rutile grains with the lowest brightness (MBH), in places, form oscillatory zoned rims (RIM) around the brighter rutile grains and appear to completely replace them, resulting in patchy brightness characterized by a higher proportion of elements with higher atomic numbers (PBH – bright zones completely enclosed within grains with lower brightness, Fig. 5d). The data have strong variation in U concentrations (20–180 ppm) and variation in precision (<1% for some analyses), with low-U analyses yielding appreciably younger ages (Appendix Fig. 4). Previous zircon U–Pb analyses of detrital zircons from GSWA 187403 indicate yielded dates from c. 3212 to 2286 Ma, with metamorphic rims yielding a date of c. 1772 Ma (Wingate et al., 2010a). In GSWA 187403, temperatures calculated based on the Zr-in-rutile thermometer are lower for patchy rutile grains and those forming rims around brighter grains (Fig. 10). Furthermore, discordant rutile grains from all textures show, on average, much lower temperatures and uranium concentrations (U = 20–100 ppm for concordant analyses and 0.2–15 ppm for discordant analyses, Appendix Table 6A). Temperatures for concordant analyses based on the Zr-in-rutile thermometer are consistently between 576 and 579°C, whereas those associated with discordance, replacement textures and rims yielded lower temperatures between 379 and 446°C (Fig. 10). This suggests modification of primary rutile during either dissolution and precipitation or solid state diffusion at lower temperatures resulting in the loss of uranium, zirconium and the addition of common Pb.

Rutile from GSWA 144898 yielded discordant dates (Fig. 9). The regression through the analyses does not allow precise age determination (lower concordia intercept of 975 ± 32 Ma, MSWD = 6.8). Zirconium-in-rutile estimates indicates a temperature of 410 ± 26°C (n = 35 of 40 analyses, 5 outliers have T = 522–747°C). No zircons have been dated from this sample.

The linear distribution of analyses in concordia diagrams observed in several samples can be interpreted as the result of mixing of a radiogenic component (lower intercept with concordia) and a common-Pb component. The composition of an ideal, U-free, common-Pb component is estimated by projecting back the linear array to the ordinates axis ($^{238}U/^{206}Pb = 0$). This intersection is close to $^{207}Pb/^{206}Pb$ values of 0.9 for GSWA 184160, 184161 and 144898, which corresponds to crustal Pb compositions ($^{207}Pb/^{206}Pb = 0.90$ at 1200 Ma for $\mu = 11$) according to Stacey and Kramers (1975). For GSWA 187403, $^{207}Pb/^{206}Pb$ of the ideal common-Pb component is much lower than expected for crustal values. These radiogenic values can be explained, for instance, by remobilization of Pb from U-bearing phases. In addition, the wide scattering of analyses away from the best-fit line (GSWA 187403) implies that not all the data can be explained as simple two-end-member mixing between radiogenic and common-Pb components, and appears to require more than one common-Pb component.

1840–1810 Ma
Leake Spring Metamorphics

Rutile from GSWA 190607 and 190608 yielded a majority of concordant or near-concordant ages, mostly spanning the range 1160–850 Ma ($^{238}U/^{206}Pb$), with a main peak at c. 900 Ma (Appendix Fig. 5). This age range encompasses the 1030–955 Ma Edmundian Orogeny and the 930–750 Ma Kuparr Tectonic Event. Calculated temperatures have a prominent peak around 600°C. This spread of dates may be the result of isotopic re-setting of rutile formed in a previous (c. 1200 Ma or older) amphibolite-facies event. A few rutile grains in GSWA 190608 have $^{207}Pb/^{206}Pb$ dates as old as c. 2497 Ma.

1820–1775 Ma
Moorarie Supersuite

GSWA 188975 and 185950 yielded all three TiO_2 polymorphs with largely MBH grains and some porous (POR) textured rutile and anatase grains. Anatase and brookite analyses are all discordant, whereas rutile yielded some concordant (n = 10) grains with dates ranging between c. 2900 and 2200 Ma (Fig. 11). The dispersion of discordant analyses, along with the range of concordant rutile analyses in GSWA 188975, suggests that rutile in this sample may be inherited. Brookite and anatase analyses in GSWA 185950 yielded mostly common-Pb compositions and contain negligible concentrations of U and Th (Appendix Table 6A). Previous U–Pb analyses of zircon from GSWA 188975 indicated a magmatic age of 1804 ± 5 Ma and dates for xenocrystic zircons between c. 3526 and 1887 Ma (Wingate et al., 2011). Previous U–Pb analyses of zircon from GSWA 185950 yielded a date of 1797 ± 6 Ma interpreted as the crystallization age and dates of inherited zircons between c. 2527 and 2004 Ma (Wingate et al., 2010c).

Anatase and brookite grains in the granitic gneiss GSWA 185950 contain no uranium and, therefore, yielded only common-Pb ratios. Under BSE, anatase displayed largely euhedral morphologies with subhedral to anhedral brookite grains (Fig. 6c). Anatase grains are commonly completely enclosed or rimmed by ilmenite, suggesting younger replacement (Fig. 3d). Consequently, anatase may have formed as a primary phase, most likely during later stages of crystallization of the granitic gneiss. Brookite was not observed in thin section and the relative timing of its formation could not be inferred.

Samples DP14-GP05, DP14-GP06, DP14-GP07 and GSWA 216818

In sample DP14-GP05, 18 analyses (out of a total of 26) of rutile yielded a concordia age of 1761 ± 7 Ma (MSWD = 1.3, Fig. 11). In sample DP14-GP06, 26 (<5% discordant) analyses (out of 55) yielded a U–Pb intercept age of 1774 ± 17 (MSWD = 2.3) and a concordia age of 1776 ± 9 Ma (Fig. 11e,f). A total of 69 analyses from sample DP14-GP07 were obtained from 15 rutile grains (Fig. 11g,h). The majority of the analyses contained high concentrations of ^{208}Pb, and Th peaks were observed in

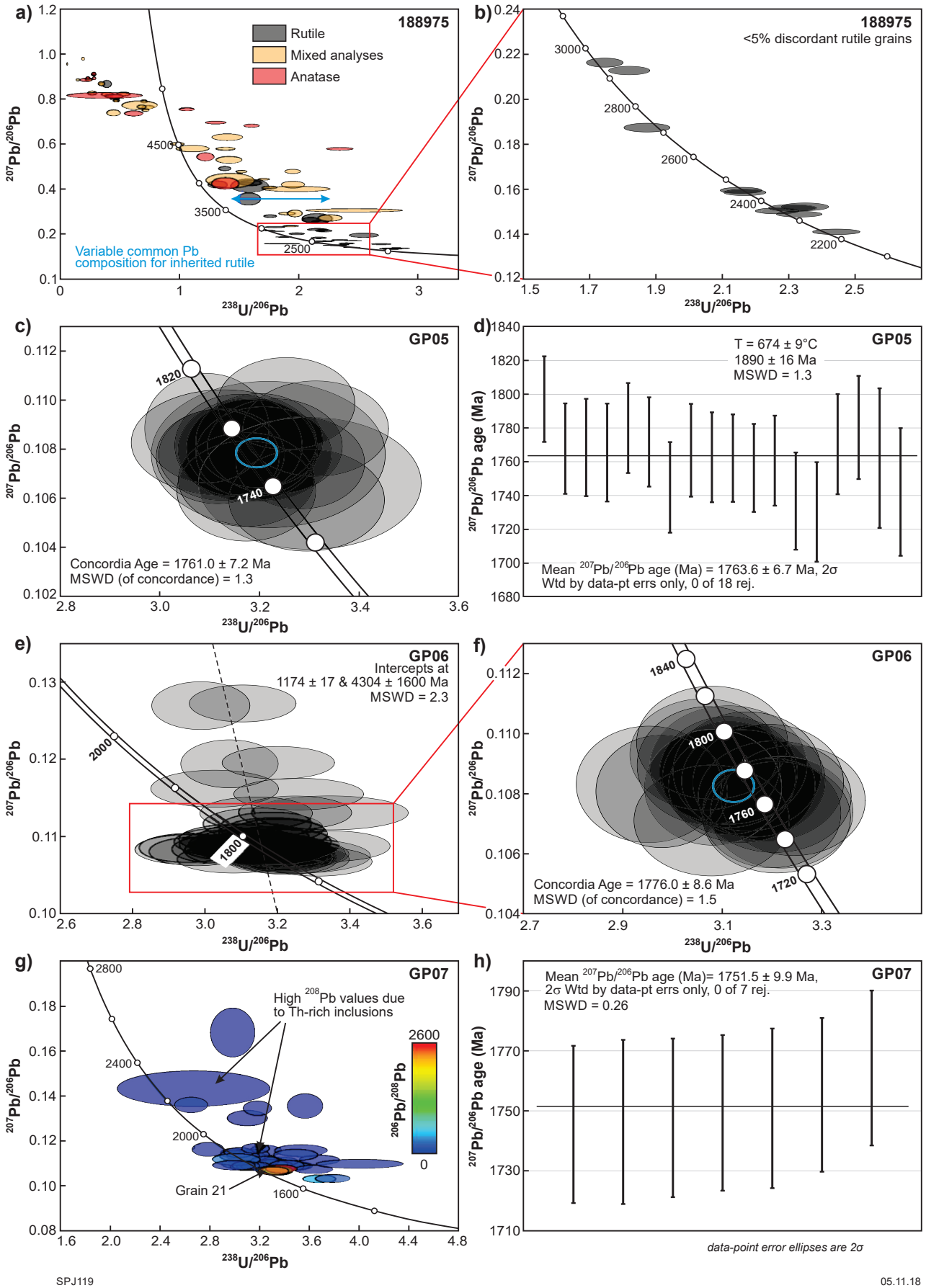

Figure 11. **Moorarie Supersuite U–Pb concordia and probability density plots with colours showing various TiO_2 phases: a) plot of rutile, anatase and brookite from GSWA 188975; b) subset of GSWA 188975 of 10 near-concordant rutile analyses; c) and d) concordia diagram and weighted average $^{207}Pb/^{206}Pb$ age for sample GP05; e) concordia plots of rutile analyses from sample GP06; f) same as e), but showing only concordant spot analyses; g) and h) concordia plot and average median $^{207}Pb/^{206}Pb$ age of rutile from sample GP07**

ablation spectra, which is consistent with the presence of phosphate- and silicate-rich micro-inclusions (zircon, xenotime and monazite) as also observed under BSE (Appendix Fig. 3a). In Th-inclusion-free (and Th-poor) grain 21, the weighted average of analyses <5% discordant on this grain yielded a $^{207}Pb/^{206}Pb$ date of 1752 ± 10 Ma (n = 7, MSWD = 0.26, 2σ). A limited number of spot analyses on rutile from GSWA 216818 did not yield any meaningful U–Pb results.

1760–1680 Ma
Pooranoo Metamorphics

Rutile grains from GSWA 168937 yielded largely discordant analyses from both the MBH to POR textured grains (Fig. 12a). The size of rutile grains (of up to 500 μm) in this sample permitted between 4 and 20 spots to be analysed for a single grain, allowing for discordia lines to be calculated for individual grains (Fig. 12b,c). The regression lines yielded imprecise lower intercepts at c. 1602, 1380, 1315, 1164 and 1151 Ma (Fig. 12b). However, some of the discordia lines have significantly high MSWD values (up to 8.8) with lower intercept uncertainties of up to 250 Ma, so caution is needed when interpreting their meaning. Nonetheless, multiple analyses on individual grains, together with the dispersion in discordant ages evident in the U–Pb Tera-Wasserburg plots, suggest that the rutile grains in this sample are of different generations, either as detrital grains, or subsequently reworked detrital grains with reset ages. Unfortunately, due to the similarity of rutile grains under BSE as well as in thin section, together with the spread of discordant ages on the Tera-Wasserburg plot, the distinction between the detrital and/or different generations of rutile cannot be made. Available detrital zircon U–Pb data for GSWA 168937 indicate two main age modes at 1968 ± 7 Ma and 1801 ±13 Ma (Nelson, 2001).

GSWA 152526 also yielded strongly discordant ages. The discordia line through all the analyses gave a lower intercept age of 957 ± 36 Ma (MSWD = 2.2). No zircons have been dated from this sample.

1679–1610 Ma
Mount Augustus Sandstone

GSWA 148972 yielded a variety of rutile textures, including MBH rutile and grains with variable brightness under BSE (PBH). In some massive textured grains, BSE brightness variations follow crystallographic orientations (Fig. 13a); whereas, in porous grains, the patchiness is randomly distributed throughout the grain (Fig. 13a, grain R3gr5). The MBH textured grains yielded largely concordant dates. The MBH rutile grains from GSWA 148972 yielded a weighted average $^{207}Pb/^{206}Pb$ date of 1679 ± 4 Ma (MSWD = 4.6, Fig. 13). Multiple spot analyses carried out on single PBH textured grains yielded lower discordia intercepts between c. 1066 and 927 Ma, whereas the porous (POR) textured grains yielded a lower intercept of 1045 ± 98 Ma (MSWD = 26, Fig. 13c). The high MSWD of the porous grains reflects the high common-Pb compositions of these grains, along with mixing of first generation rutile (c. 1680 Ma) and the younger metamorphic rutile (at c. 1050 Ma). However, lower intercept ages of c. 1050 Ma for the POR and PBH textured grains along with low Zr and the addition of common Pb, suggest these grains formed during a younger tectonothermal event that was associated with lower temperatures and an increase in the concentration of Nb (Fig. 13b). Detrital zircons from this sample yielded a main age component at 1679 ± 3 Ma (Martin et al., 2008), with older grains between c. 2435 and 1794 Ma (Wingate et al., 2007a).

1673–1455 Ma
Edmund Group

GSWA 148945 and 172241, Depositional Package 1

Rutile analyses in Depositional Package 1 GSWA 148945 yielded concordant analyses with high calculated temperatures (>550°C, peak at around 650°C) as well as low-U strongly discordant analyses with lower temperature (<550°C). A linear regression through all the analyses gives a lower intercept of age 1679 ± 26 Ma (MSWD = 3.7) (Fig. 14c). No zircons from this sample have been dated.

In GSWA 172241, rutile is strongly discordant with calculated low temperatures (mostly 400–500°C). A statistically reliable age could not be determined for this sample, but the discordia line intercepts concordia at c. 1350 Ma.

GSWA 148974, Depositional Package 4, Ullawarra Formation (Curran Member)

GSWA 148974 yielded a variety of rutile textures with most showing MBH textures, as well as rutile grains with variable brightness under BSE (PBH). Rutile from this sample yielded a spread in concordant ages between c. 3150 and 2050 Ma, largely from analyses of moderately bright, featureless (MBH) rutile grains, interpreted here to represent detrital rutile grains (Fig. 14a,b). The porous (POR) textured grains yielded only discordant data with an array of discordant analyses with variable common-Pb composition (Fig. 14a). Only some grains were sufficiently large to allow multiple analyses to be carried out (a maximum of up to nine analyses per grain, see inset Fig. 14b). A probability density plot yields a number of peaks, of which the main age modes are at c. 2675, 2454, 2345 and 2275 Ma, suggesting largely Paleoproterozoic and minor Archean sources (Fig.14b). Previous U–Pb dating of detrital zircons from this sample yielded a main age component at 1680 ± 10 Ma, with older grains between c. 3064 and 1760 Ma (Wingate et al., 2007b).

Other samples

2758–2585 Ma Warrigal Gneiss

Warrigal Gneiss GSWA 44617 yielded concordant to strongly discordant results for rutile. Near-concordant analyses gave a $^{207}Pb/^{206}Pb$ weighed mean $^{207}Pb/^{206}Pb$ date of 1906 ± 11 Ma (MSWD = 14; n = 34; Appendix Fig. 6).

2014–1920 Ma Bryah Group

There was no detectable U or Pb in rutile from Bryah Group GSWA 50859, thus a U–Pb age could not be determined. Only trace element analyses are available (see the following section Trace element geochemistry).

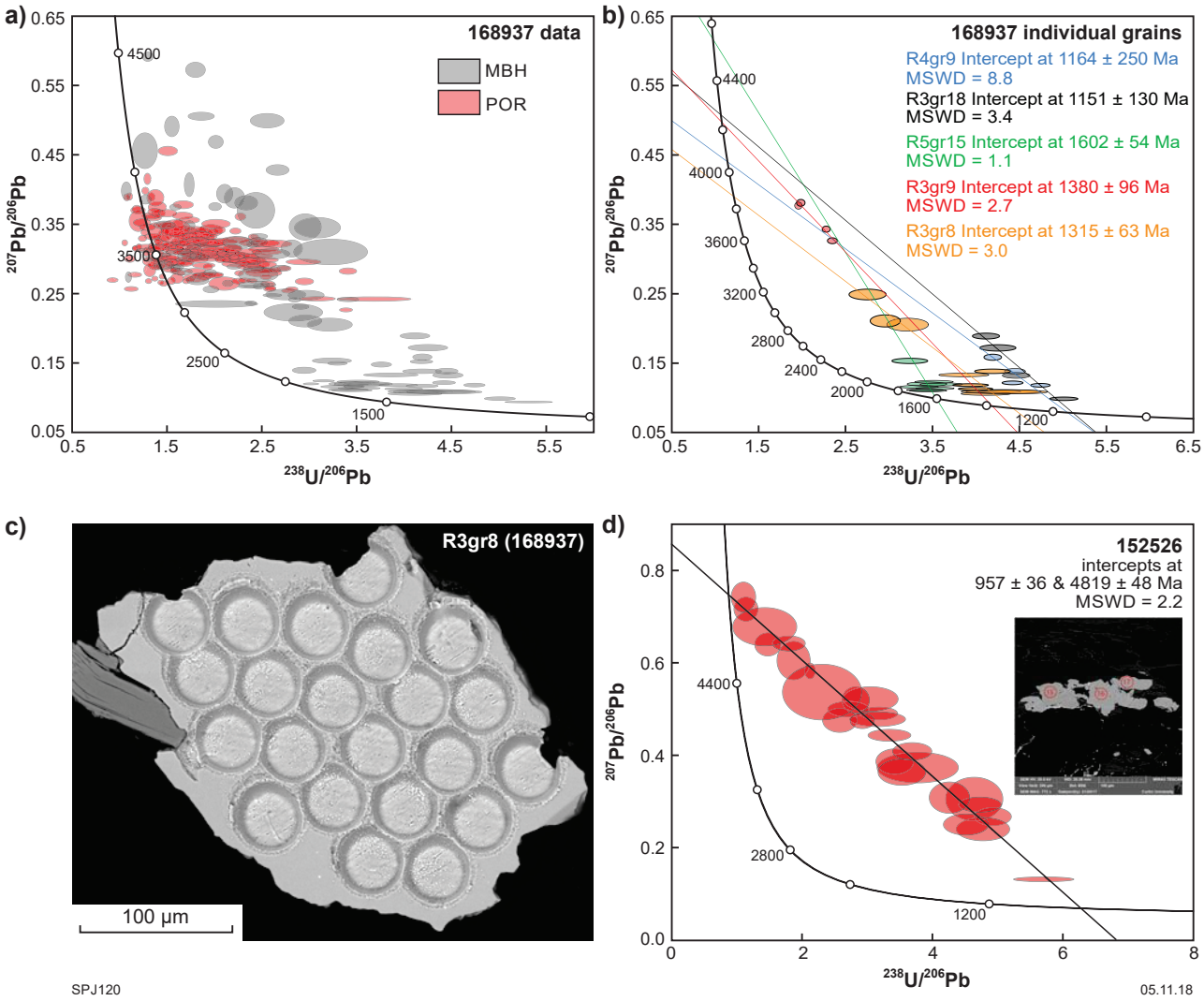

Figure 12. Pooranoo Metamorphics U–Pb rutile geochronology data: a) U–Pb concordia plot of GSWA 168937, showing analyses with colours indicating variation in texture of rutile grains; b) individual grain U–Pb discordia lines; c) BSE image of a rutile grain showing laser ablation spots on a single grain; d) U–Pb data for GSWA 152526 and BSE image of rutile (inset)

2005–1975 Ma Dalgaringa Supersuite

Rutile in Dalgaringa Supersuite GSWA 70747 yielded concordant to strongly discordant dates. Concordant dates span between c. 1400 and 890 Ma, with a major mode at c. 920 Ma (Appendix Fig. 6).

Trace element geochemistry

2240–2125 Ma Moogie Metamorphics

A trace element comparison for all samples is shown in Figure 15a. The lowest concentrations (typically <40 ppm) were observed mainly for Mn (with only six outliers of up to 250 ppm), Ni, Cu, Hf and Mo across all samples (Fig. 15a). However, some variations were observed between samples, with Mo and W enriched (Mo up to ~40 ppm, W up to ~18 000 ppm) in GSWA 187403 compared to GSWA 184160 and 184161 (0.1 – 1 ppm Mo, 3.7 – 1810 ppm W). Copper concentrations were consistently between 14–20 ppm for most samples of the Moogie Metamorphics, with relative enrichment (up to ~100 ppm) in GSWA 184160, 184161 and 187403 (Fig. 15a). Chromium values are typically between 1–1500 ppm for most samples, whereas V and Al are commonly enriched in GSWA 184160 and 184161 compared to GSWA 187403 (Fig. 15a). Highest concentrations were observed for Fe, Nb and Ta (Nb up to 110 000 ppm) in GSWA 187403, with comparably lower concentrations of all those elements in GSWA 184160 and 184161. The patterns of enrichment for Fe, Nb and Ta are strikingly similar between, and within, all three samples (Fig. 15a). Antimony concentrations are highest in GSWA 187403 (up to 277 ppm) and 216806 (up to 806 ppm) and associated mostly with discordant MBH textured grains, along with rims and patchy rutile grains. Zirconium and Hf show similar patterns of enrichment, with higher concentrations observed in GSWA 187403 (Zr = 180–520, Hf = 13–32 ppm) compared to GSWA 184160 and 184161 (typically Zr <100 ppm, Hf <5 ppm).

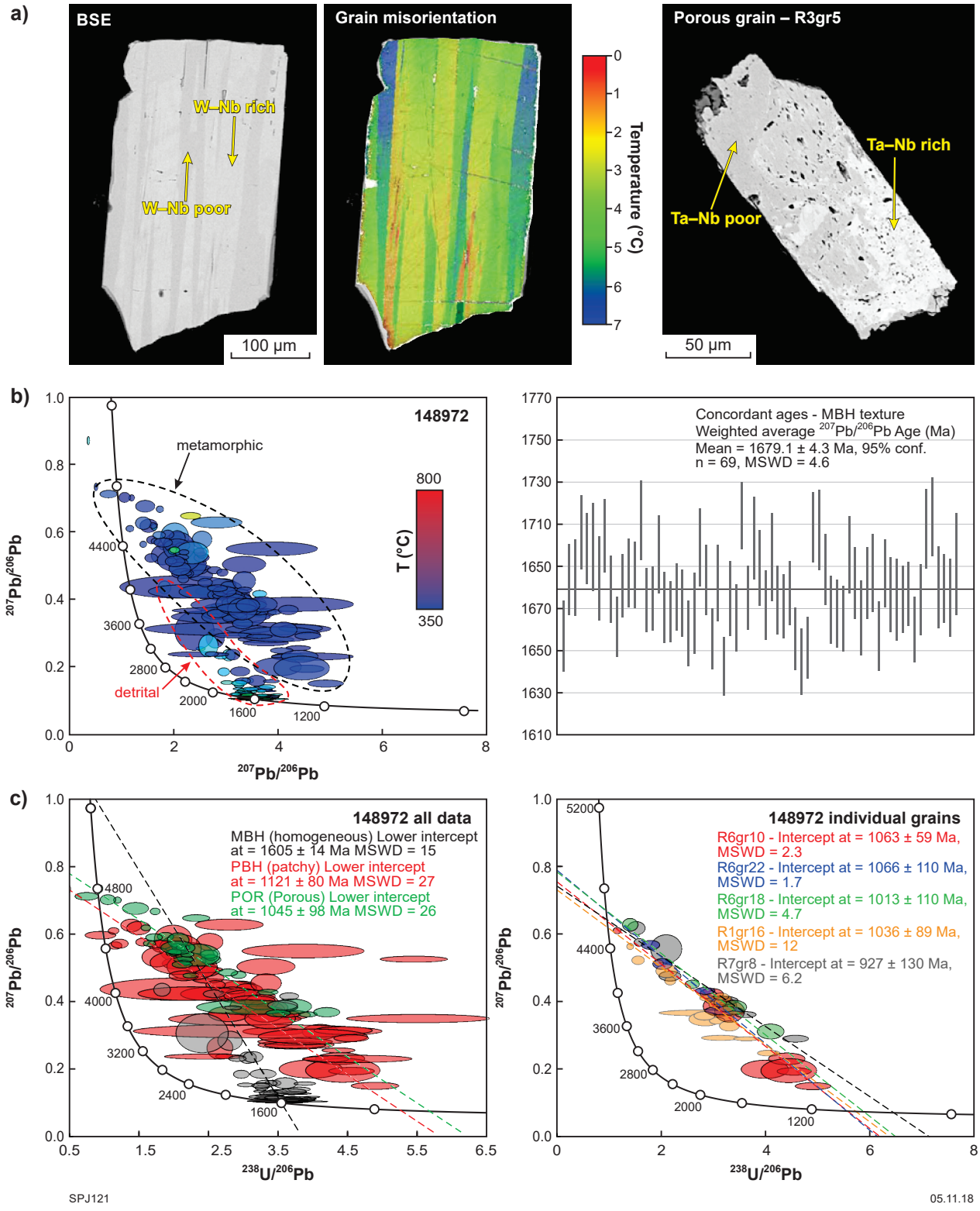

Figure 13. Edmund Group BSE and EBSD images and U–Pb geochronology data for rutile grains in GSWA 148972: a) BSE and EBSD images showing variation in brightness aligned with grain misorientation. Porous (POR) grain (R3gr5) showing variable brightness due to Nb and Ta enrichment; b) U–Pb concordia plot (colour-code based on Zr-in-rutile thermometry) and weighted average age of concordant analyses; c) U–Pb concordia plot for all data with colours representing different textures. Individual grain discordia were calculated for single grains on which multiple analyses were carried out

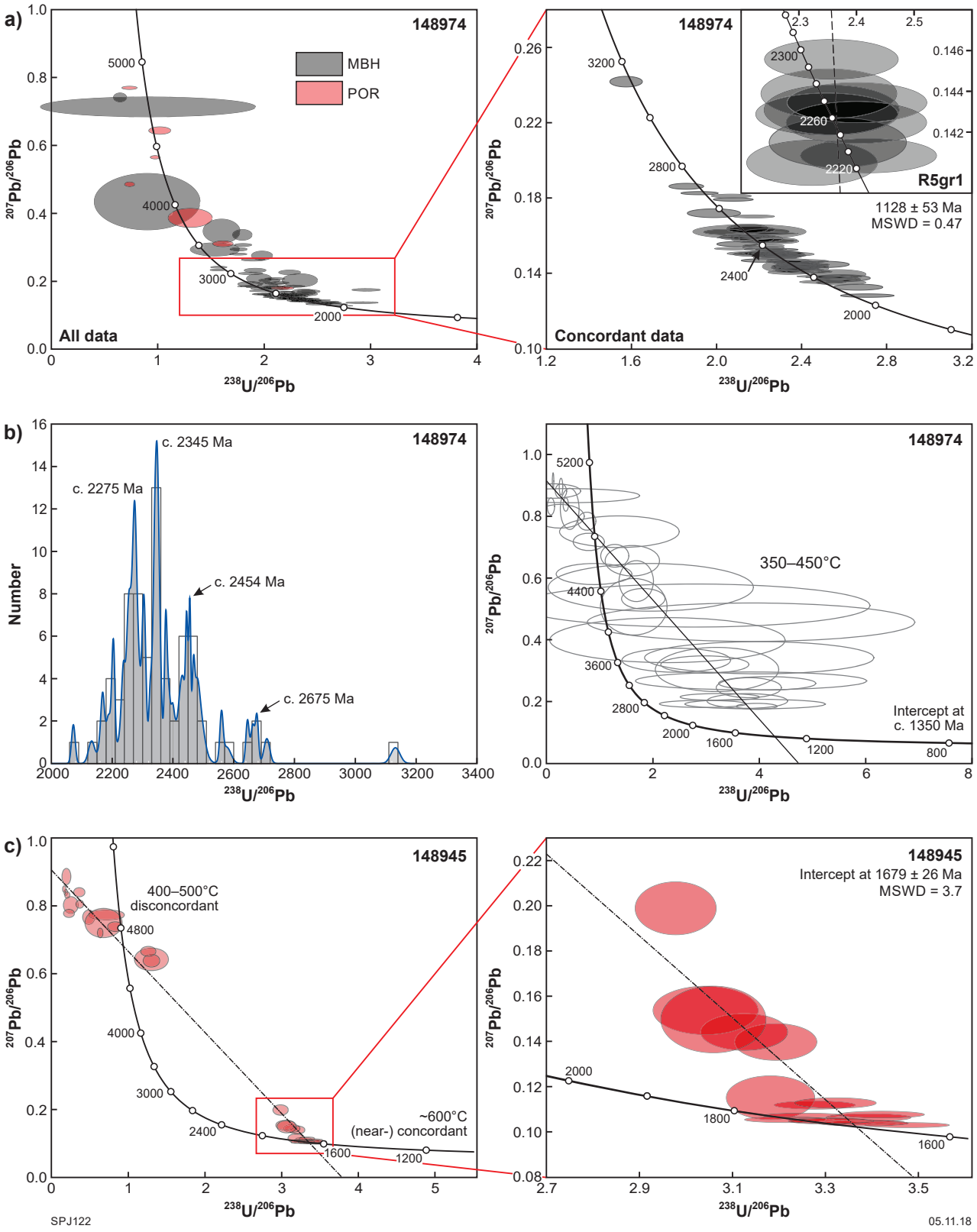

Figure 14. Edmund Group U–Pb rutile geochronology, GSWA 148974, 172241 and 148945: a) U–Pb concordia showing all data from GSWA 148974 and subset of data showing only concordant analyses; b) probability density plot of <5% discordant analyses (GSWA 148974) and U–Pb concordia diagram for GSWA 172241; c) U–Pb concordia diagram for GSWA 148945 and subset of data close to 1679 Ma

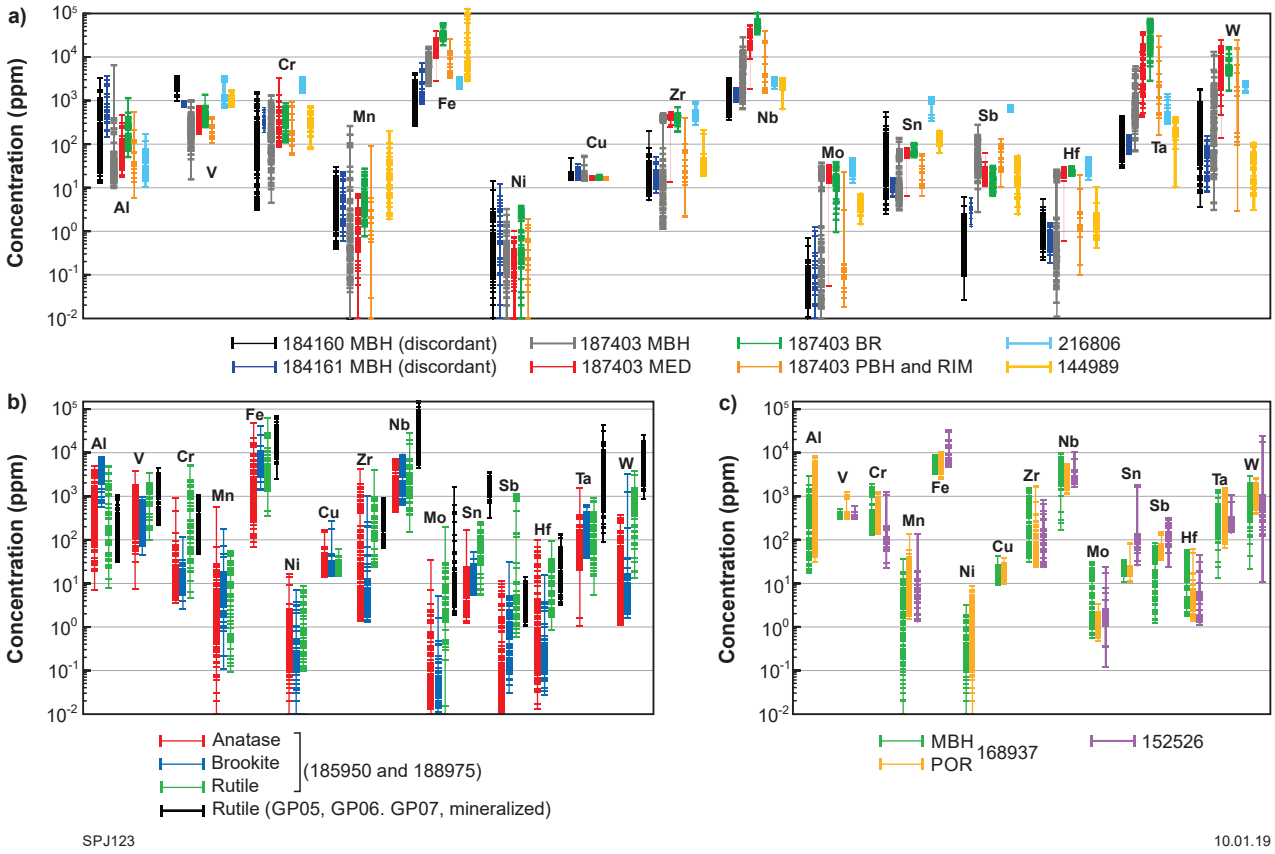

Figure 15. Trace element comparison plots for the Moogie Metamorphics (GSWA 184160, 184161 and 187403), Moorarie Supersuite (GSWA 185950 and 188975) and Pooranoo Metamorphics (GSWA 168937), Gascoyne Province

Zirconium and Hf concentrations in grains from GSWA 187403 with high discordance, showing patchy zoning in BSE images, or from rims (PBH and RIM), have lower Sb and higher Zr than other textural types (Fig. 15).

Correlations between different element pairs are shown in Figure 16. Positive correlations between all samples occur for Fe vs W, Fe vs Nb, and Fe vs Ta (Fig. 16a,b,c), as well as for Cr vs Nb (Fig. 17a) and W vs Mo (not shown). The much higher values of Fe with respect to Nb for GSWA 144898 (Fig. 16b) are due to Fe-rich inclusions in rutile. Aluminium correlates positively with Sb for GSWA 184160 and 184161 with a slight negative correlation in GSWA 187403 (Fig. 16e). Furthermore, positive correlations occur for GSWA 187403 between Fe and V, as well as Al and Nb, but no correlation between those element pairs occurs for GSWA 184160 and 184161 (Fig. 16f,g).

On the Cr vs Nb plot of Zack et al. (2002, 2004) for characterizing source provenance, most analyses plot in the 'metapelitic' field, suggesting largely felsic derivation (Fig. 17a). On the 100(Fe+Cr+V)–Ti–1000(W) discrimination plot of Clark and William-Jones (2004) for rutile associated with gold deposits (Fig. 18a), the majority of the analyses plot in the field of rutile associated with a mineralized zone. The majority of the Nb/Ta ratios for all samples are subchondritic (<17.5, Sun and McDonough, 1989) and range between 0.6 and 33 (Fig. 19a) whereas Zr/Hf ratios range between 6.8 and 40 (with minor outliers up to ~120 ppm). The variation in Nb/Ta ratio (particularly for GSWA 187403) is largely due to an increase in Ta for the brightest grains (Fig. 16d, MED and BRH), whereas the Hf vs Zr plot shows mainly a 1:1 correlation ($R^2 = 0.96$), with deviation from the linear regression line mainly in the brightest (BRH) grains (Fig. 16h).

1840–1810 Ma
Leake Spring Metamorphics

GSWA 190607 and 190608 have Nb contents between 2100 and 4600 ppm (Fig. 21), and are relatively enriched in Sn (up to 970 ppm) and Mo (up to 23 ppm). In the Cr vs Nb diagram (Fig. 17b), most analyses plot in the 'metapelitic' field, and a limited number of analyses plot in the metamafic field.

1820–1775 Ma
Moorarie Supersuite

A comparison of trace element concentrations for different TiO_2 phases in Moorarie Supersuite GSWA 185950 and 188975 is shown in Figure 15 and Appendix Table 5A. The lowest concentrations for all phases were observed for Ni (0.01–17 ppm), Mn (0.1 – 176 ppm), Mo (0.01 – 34 ppm) and Hf (0.01 – 100 ppm). Greatest enrichments, with orders of magnitude variations, occur for Nb (147–28 700 ppm), Fe (67–61 600 ppm), Al (7–8060 ppm) and V (8–3700 ppm).

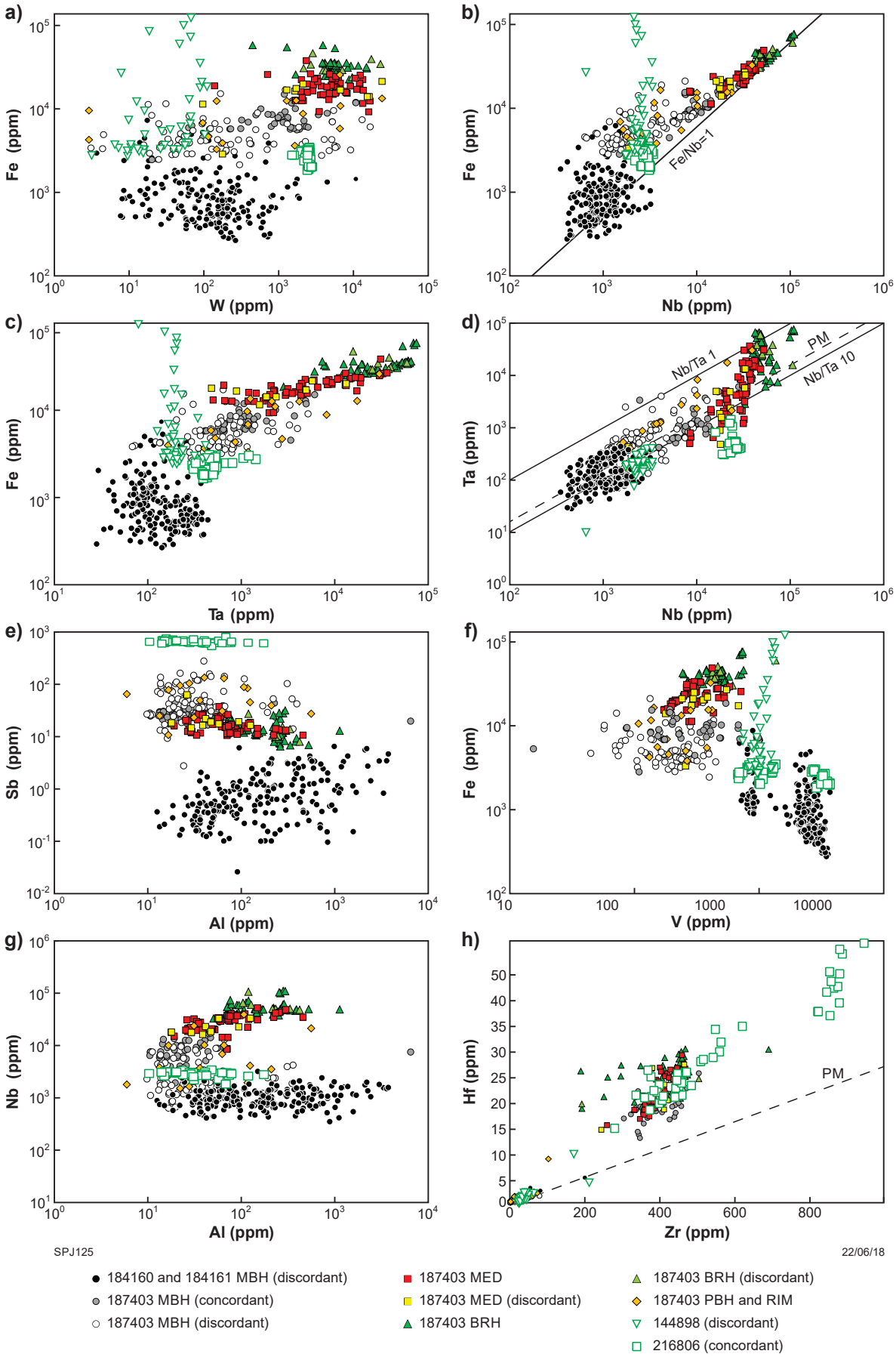

Figure 16. Trace element binary plots, Moogie Metamorphics. Abbreviation: PM, primitive mantle (Sun and McDonough, 1989)

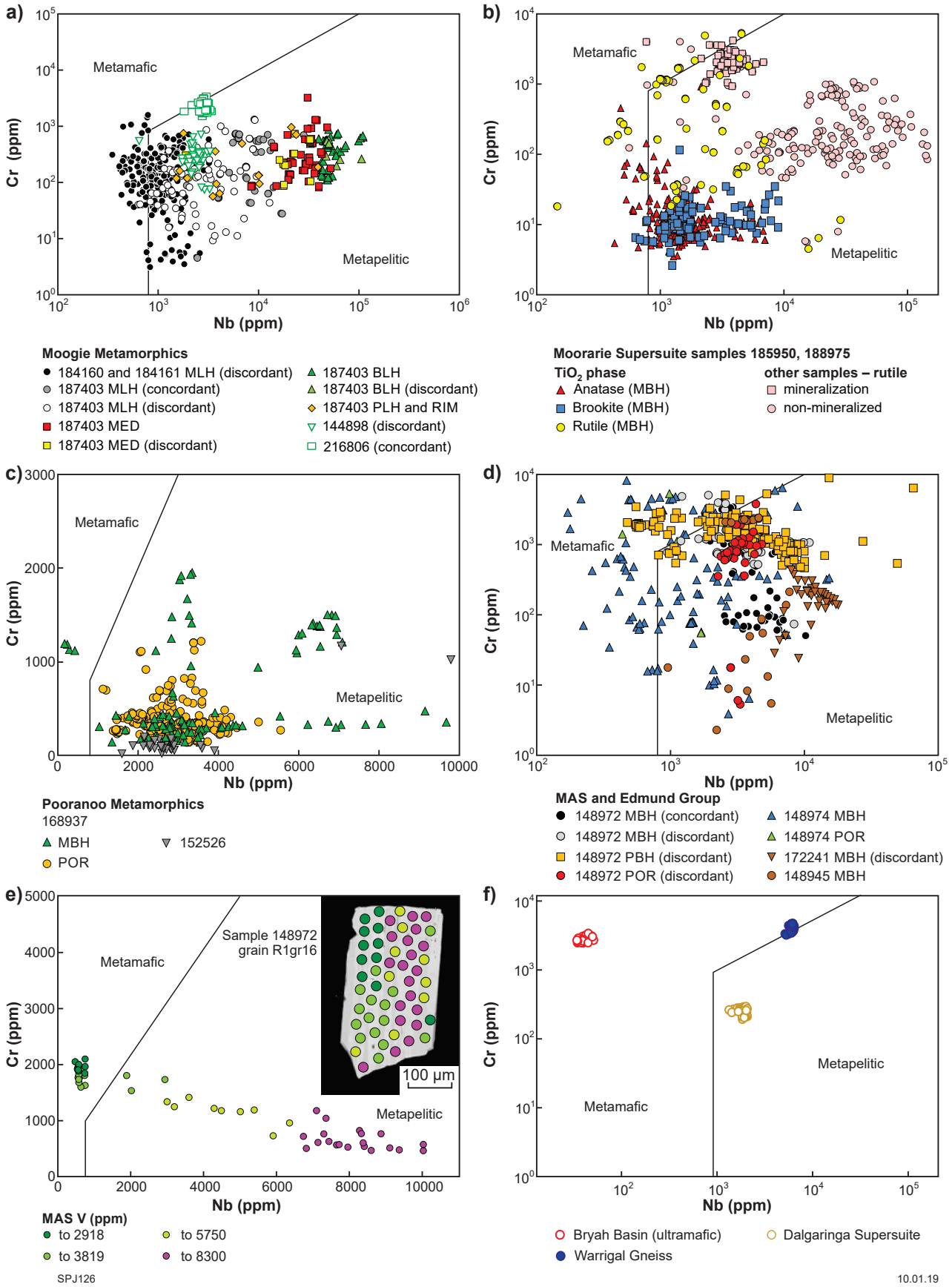

Figure 17. **Cr vs Nb discrimination plots for metamafic vs metapelitic rutile sources after Zack et al. (2002, 2004): a) Moogie Metamorphics; b) Moorarie Supersuite; c) Pooranoo Metamorphics; d) Mount Augustus Sandstone and Edmund Group; e) Single grain (GSWA 148972, R1gr16,) variation in Nb and Cr concentrations and the associated increase in V concentrations; f) Warrigal Gneiss, metasedimentary rocks in the Dalgaringa Supersuite, ultramafic rocks of the Bryah Group**

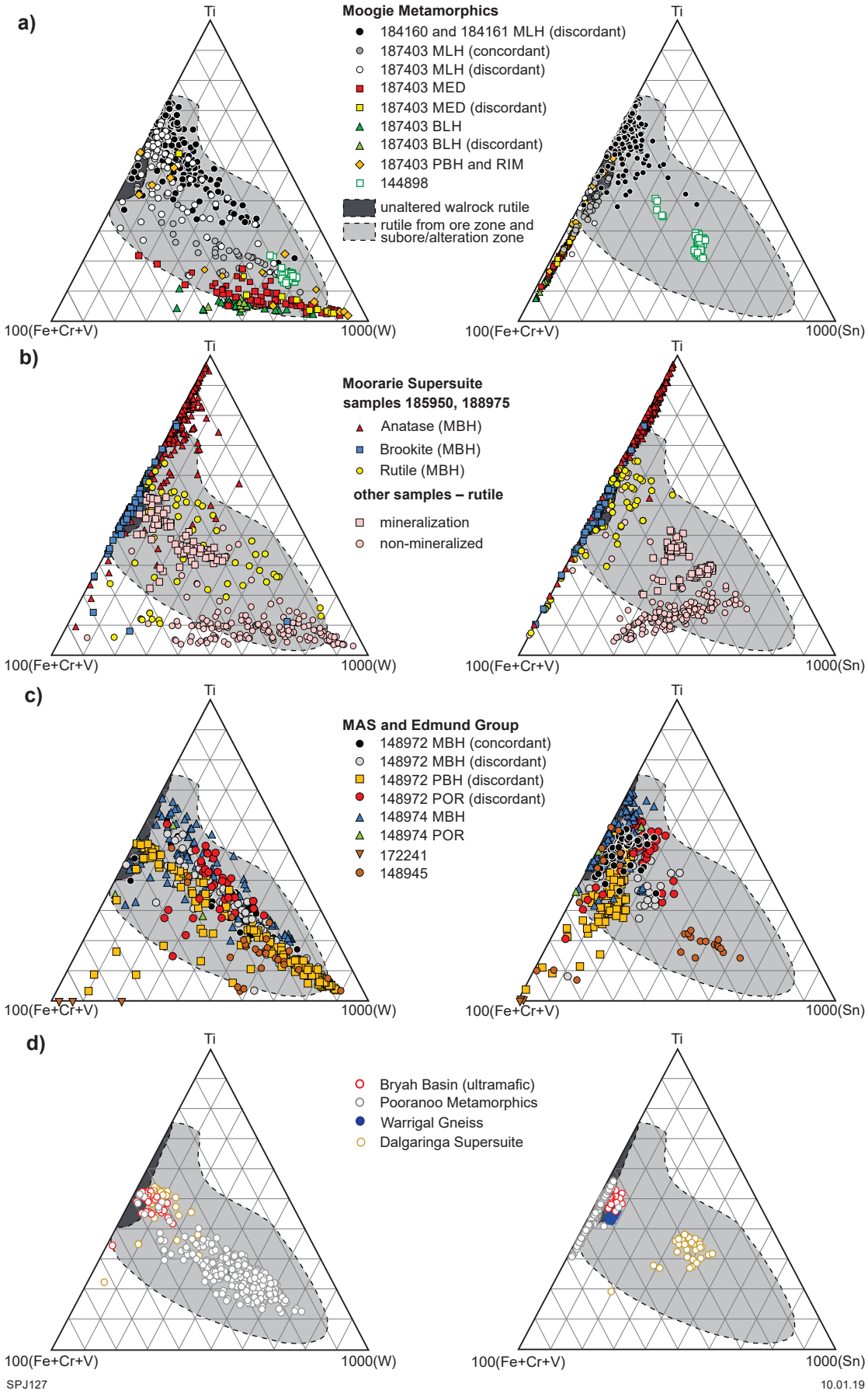

Figure 18. Ternary plots for discriminating rutile within unaltered, altered and mineralized bedrock after Clark and William-Jones (2004): a) Moogie Metamorphics; b) Moorarie Supersuite (various TiO_2 phases in GSWA 185950 and 188975, and rutile in other samples); c) Mount Augustus Sandstone (MAS) and Edmund Group; d) Pooranoo Metamorphics and other units

The highest Fe enrichments can be attributed to contamination with Fe-rich inclusions, such as ilmenite. Moderate enrichments, with the greatest variation between samples, exist for Cr with highest concentrations observed for rutile — mostly between 5–2400 ppm, with two outliers up to 5160 ppm –– (Fig. 15b), compared to brookite (3–115 ppm) and anatase (4–922 ppm). Similarly, W is enriched in rutile –– 61–1500 ppm, with two outliers up to 3750 ppm –– (Fig. 15b) compared to brookite (2–38 ppm, n = 68, with three outliers up to 3220 ppm) and anatase (1–310 ppm). Concentrations of Sb and Sn are higher in rutile (0.6 – 1130 ppm and 5.4 – 261 ppm, respectively) compared to brookite (Sb = 0.03 – 30.2 ppm, Sn = 5.4 – 53.2 ppm) and anatase (Sb = 0 – 11.1 ppm, Sn = 1.3 – 23.6 ppm). Aluminium concentrations are higher for brookite (553–8060 ppm), and lower in anatase (7–4900 ppm) and rutile (8–4890 ppm). Element pairs Hf and Zr show similar behaviour between the phases, with lowest concentrations observed in brookite (Hf = 0.03 – 3.7, Zr = 0–260 ppm with the majority of analyses having Zr up to 10 ppm) and highest in anatase (Hf = 2.2 – 100 ppm, Zr = 1.36 – 1860 ppm, with one outlier at 4170 ppm Zr), and rutile (Hf = 0.8 – 92 ppm, Zr = 23.4 – 960 ppm, with one outlier at approximately 4000 ppm Zr). However, unusually high concentrations of Zr (typically >2000 ppm) in anatase and rutile are commonly associated with the porous texture and massive textured grains indicating the presence of zircon micro-inclusions, as were observed under BSE. Rutile from samples DP14-GP05, DP14-GP06 and DP14-GP07, which are associated with Mo mineralization, has the highest concentrations of Nb, W, Ta and Sn in comparison to other Moorarie Supersuite samples. Rutile from metamafic GSWA 216818 has lower Nb (<2300 ppm), W (<110 ppm), Sn (<15 ppm) and Mo (<2.5 ppm) compared to other Moorarie Supersuite samples.

On ternary diagrams of Clark and William-Jones (2004), the majority of rutile grains from the 1820–1775 Ma Moorarie Supersuite samples plot in the field of rutile associated with ore zone (i.e. closer to the W apex), whereas anatase and brookite plot in the field of 'unaltered wallrock rutile' with anatase lying closer to the Ti apex and brookite closer to the 100(Fe + Cr + V) apex (Fig. 18b). However, if Sn is used instead of W, most analyses shift closer to the 'unaltered wallrock rutile' field, with rutile analyses still mostly plotting in the 'rutile from ore zone' field (Fig. 18b). When combined, the abovementioned variations in trace elements (Al, Fe, Cr, Sb and Sn) between different phases can be used to create ternary diagrams that can discriminate the three phases based on their composition (Fig. 20a). Brookite commonly plots closer to the Al and Fe apices and away from the Cr apex, whereas enrichment of Cr, Sb + Sn in rutile compared to anatase and brookite shifts the analyses closer to those apices (Fig. 20a). Anatase analyses commonly plot in the intermediate field between brookite and rutile.

Binary diagrams (Fig. 21) show some contrasting trends between different phases. All phases show positive correlation between Nb and Ta (Fig. 21b) as well as Zr and Hf (not shown) element pairs, as expected, due to their similarity in ionic sizes and charge. There is no correlation between Fe and Nb in GSWA 185950 and 188975, apart from a minor increase in Fe and a decrease in Nb for some analyses in all the phases (Fig. 21a). In contrast, Fe and Nb are strongly correlated in samples DP14-GP05, DP14-GP06 and DP14-GP07. Vanadium shows a negative correlation with Nb for anatase and brookite (Fig. 21c), whereas rutile shows no correlation for those element pairs in the unmineralized samples, and a positive correlation for the mineralized samples (DP14-GP05, DP14-GP06 and DP14-GP07). Furthermore, Fe and Sb correlate positively for anatase and brookite (Fig. 21f), but no correlation is observed for rutile. In addition, all phases show positive correlation between Fe vs Al and Zr vs W element pairs (Fig. 21g,h), albeit at different rates, as the rate of increase of Al with an increase in Fe in rutile is lower than that for anatase and brookite (Fig. 21g). Similarly, anatase and brookite show slight positive correlation on the Cr vs V plot (Fig. 20b), whereas rutile does not. Therefore, on the Fe/Al vs V/Cr plot (Fig. 20b), the majority of the rutile analyses plot at high-Fe/Al ratios (up to 143) and lower V/Cr ratios (<50), whereas brookite and anatase show consistently lower Fe/Al ratios (<20) and higher V/Cr ratios (up to 140). Element pair ratios Nb/Ta and Zr/Hf are quite variable and range from subchondritic to superchondritic (Fig. 19b).

1760–1680 Ma Pooranoo Metamorphics

Trace element concentrations for the two different grain types based on their texture are shown in Figure 15c. The lowest (<100 ppm) but variable concentrations for both porous (POR) and nonporous (MBH) grain varieties were obtained for Ni (0.01 – 8.6 ppm), Mo (0.47 – 31.61 ppm), Cu (9–42 ppm), Sn (11–85 ppm) and Hf (1.34 – 63 ppm). The nonporous (MBH) grains have slightly depleted values of Mn (0.01 – 35 ppm) and Sb (1.24 – 82 ppm) when compared to porous grains (Mn = 1.55 – 138 ppm and Sb = 34.4 – 154.4 ppm). Moderate enrichments with some order of magnitude variations occur for V (296–1266 ppm), Cr (132–1950 ppm), Ta (13–1512 ppm), Zr (24–1690 ppm) and W (21–2967 ppm) in both porous and nonporous grains. Tantalum and W are marginally lower in the nonporous grains (Fig. 15c). The greatest, but variable, enrichments occur for Al (17–8180 ppm), Fe (2490–10500 ppm) and Nb (172–9680 ppm), with Al marginally more enriched in porous grains (Fig. 15c).

Binary plots between various elements are shown in Figure 22. Positive correlation for all analyses is shown by the Zr vs Hf elemental pair (Fig. 22a), whereas the typically coupled Nb and Ta pair show some divergence, with Ta enrichment in porous grains at lower Nb concentrations and lower Ta concentrations in nonporous grains at higher Nb concentrations (Fig. 22b). Iron and Nb have a linear positive correlation in the MBH grains of GSWA 168937, whereas porous grains tend to have higher Fe at any given Nb value (Fig. 22c). These high-Fe values that deviate from the linear Fe–Nb correlation may be due to contamination with Fe-rich inclusions. Vanadium shows a slight positive enrichment for all grains with the exception of several high V analyses within the porous grains (Fig. 22d). A somewhat less pronounced negative correlation occurs between Mo and Sb in the nonporous grains, whereas the porous grains form a tight cluster (Fig. 22e). Similarly, Zr correlates positively with Mo in the nonporous grains, but no such correlation was observed for the porous grain analyses (Fig. 22f). Rutile from GSWA 168937 shows a relative enrichment in Sb and Sn in comparison to GSWA 152526. Depletion of Mn and Sb in the MBH grains is also shown in Figures 22g and 22h, respectively.

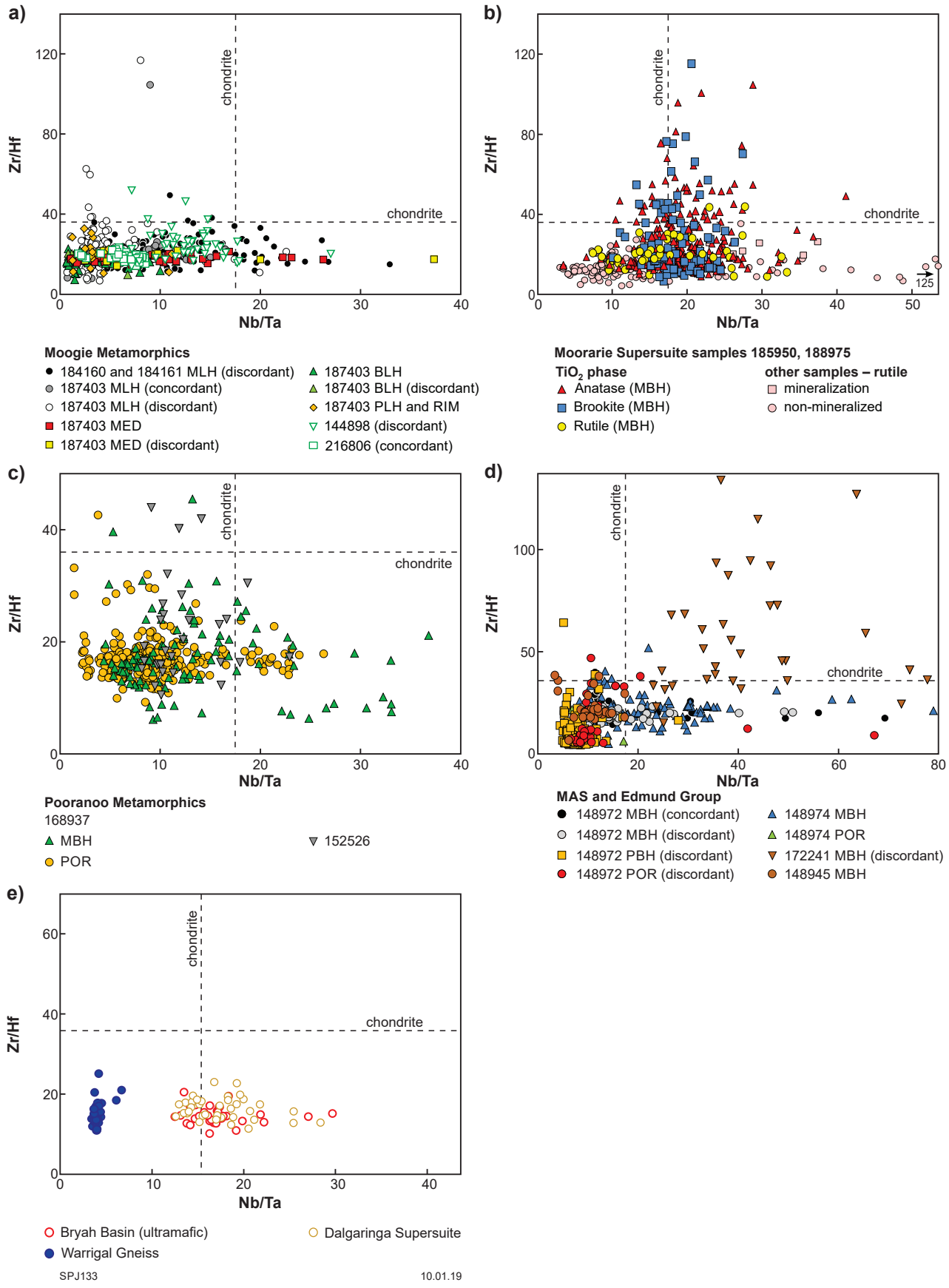

Figure 19. Zr/Hf vs Nb/Ta ratios of rutile grains from all samples. Chondritic values from Sun and McDonough (1989)

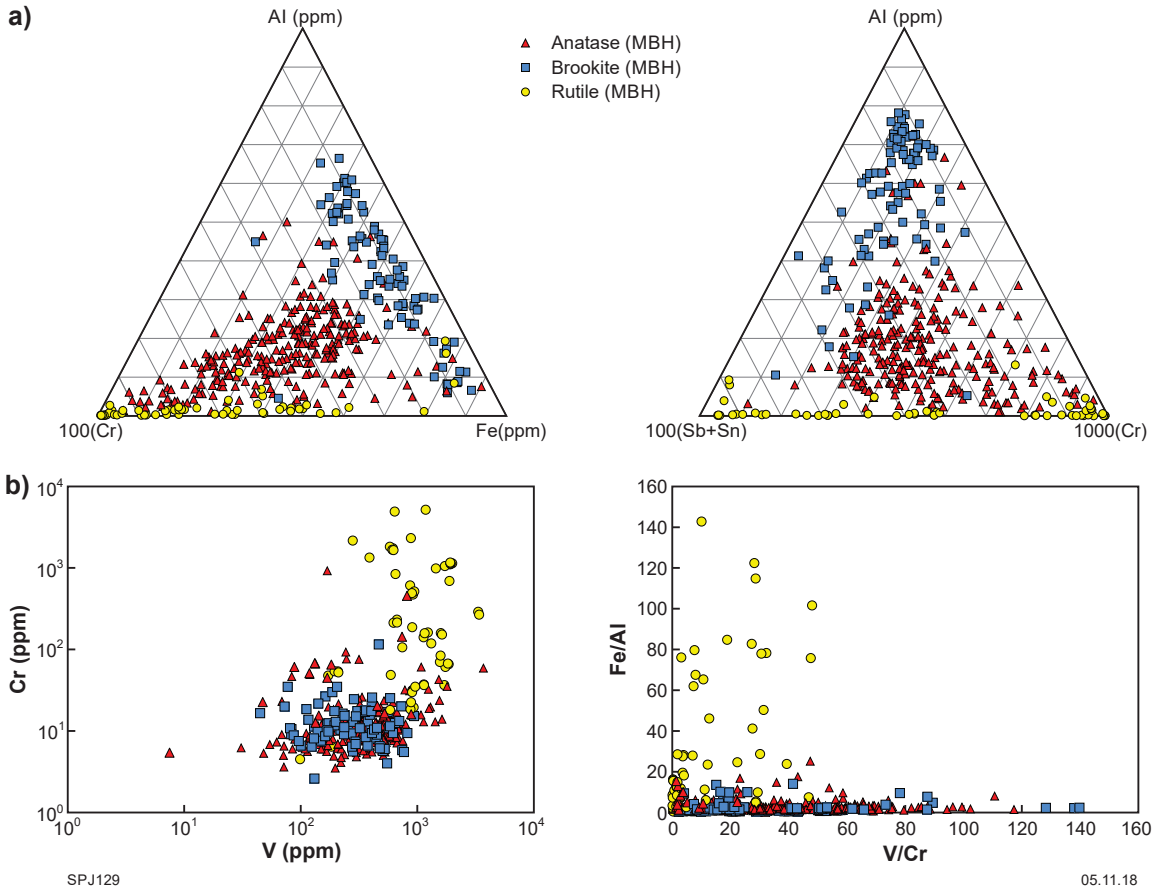

Figure 20. Discrimination plots for different TiO_2 polymorphs in Moorarie Supersuite igneous rocks (GSWA 185950 and 188975): a) ternary plots showing different trace element concentrations between anatase, brookite and rutile; b) binary plots Cr vs V and Fe/Al vs V/Cr showing higher concentrations of Cr and Fe/Al ratios in rutile compared to anatase and brookite

On the Nb vs Cr plot, most of the analyses plot in the 'metapelitic' field (Fig. 17c), whereas Nb/Ta and Zr/Hf ratios are largely subchondritic for the majority of the analyses, with some analyses also showing superchondritic values (Fig. 19c). Furthermore, in the discrimination plot of Clark and William-Jones (2004), the majority of the analyses plot in the 'rutile from ore zone' field when W is used at the right apex. However, with Sn at the right apex, all analyses plot along the Ti and 100(Fe + Cr + V) tie line in the 'unaltered wallrock rutile' field (Fig. 18d).

1679–1610 Ma
Mount Augustus Sandstone

Trace element concentrations for the Mount Augustus Sandstone sample (GSWA 148972), together with Edmund Group samples, are shown in Figure 23 and Appendix Table 6A, with binary plots displayed in Figure 24. Order of magnitude variations between all samples and grain textures occur for Al (from detection limit 9300 ppm), Cr (5 – 4890 ppm), Zr (mostly up to 840 ppm), Nb (up to 14 000 ppm) and W (up to 13 000 ppm). Greatest enrichments occur for V (≤8200 ppm) and Fe (mostly ≤11 000 ppm). Patchy (PBH) zoned rutile grains in GSWA 148972 (Fig. 23) show the greatest enrichment in V, Nb, Sn, Ta and W compared to other rutile textures (MBH and POR), but are depleted in Mo and Sb. The lowest concentrations (<10 ppm) were obtained for Mn, Ni, Cu, Mo and Hf. Tin is marginally more enriched (1.2 – 43 ppm) in the patchy (PBH) rutile grains in GSWA 148972, compared to other texturally different grains within the same sample (0.66 – 17 ppm).

Binary diagrams show positive correlations between Nb and Fe for all textures, suggesting a coupled substitution (Fig. 24a,b,c). The positive correlation of W and V with Nb for the patchy (PBH) zoned rutile grains (GSWA 148972, Fig. 24d,e, respectively) is likely an analytical artefact due to the large spot size leading to mixed analyses of different BSE zones (other samples and textures show no such correlation). An overall negative correlation for all rutile grains in GSWA 148972 is observed for V and Sb (Fig. 25f), with a negative correlation between Fe and Cr for the MBH concordant grains in the same sample. A broadly positive correlation between Zr and Mo is observed when considering Mount Augustus Sandstone (MAS) and Edmund Group samples (Fig. 24g). However, on the Sb vs Zr plot, patchy (PBH) zoned and porous (POR) grains from GSWA 148972 show a positive correlation, whereas moderately bright and homogeneous (MBH) grains show a negative correlation (Fig. 24h).

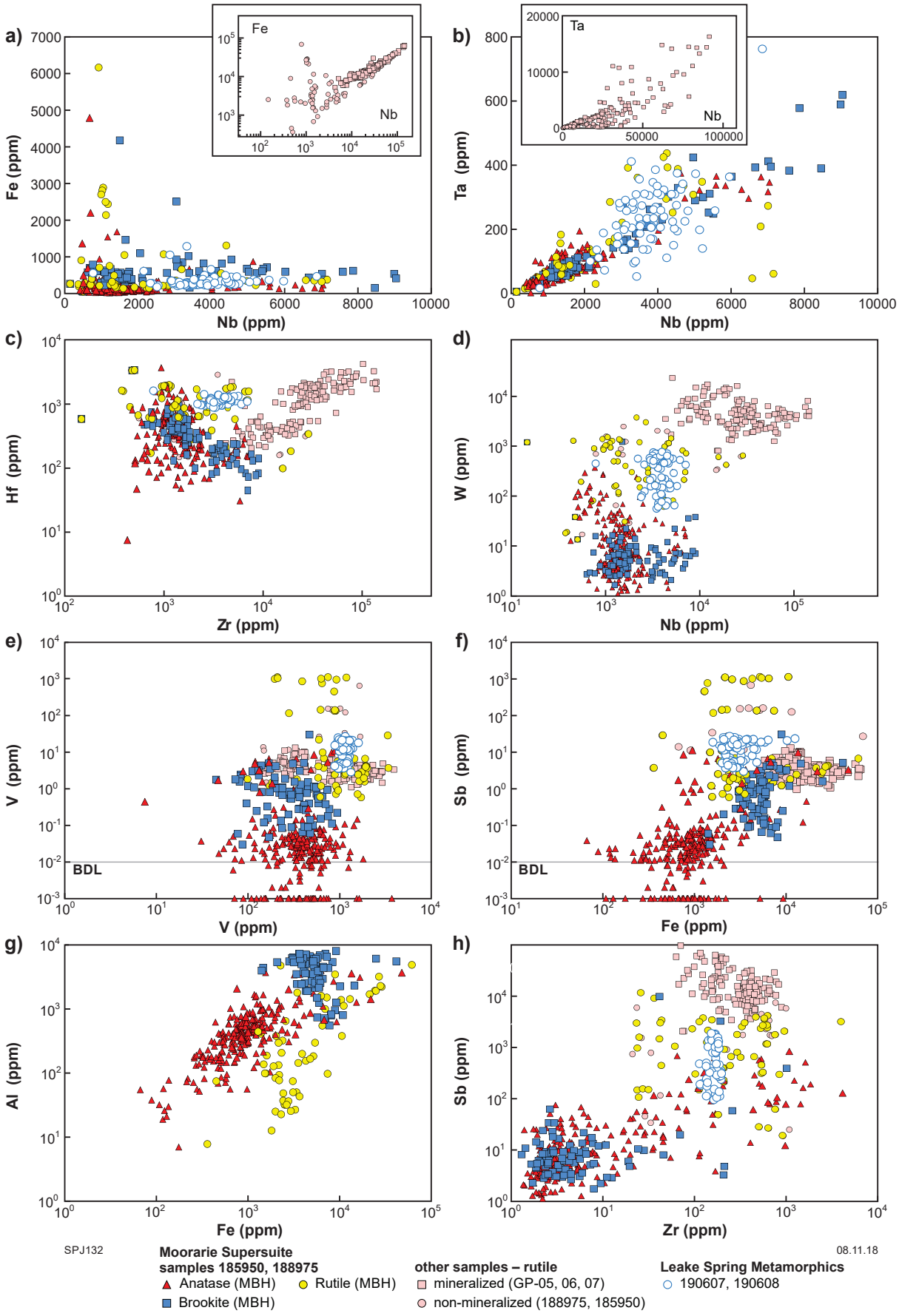

Figure 21. Binary trace element plots of rutile from the Moorarie Supersuite. Element concentrations are in parts per million (ppm)

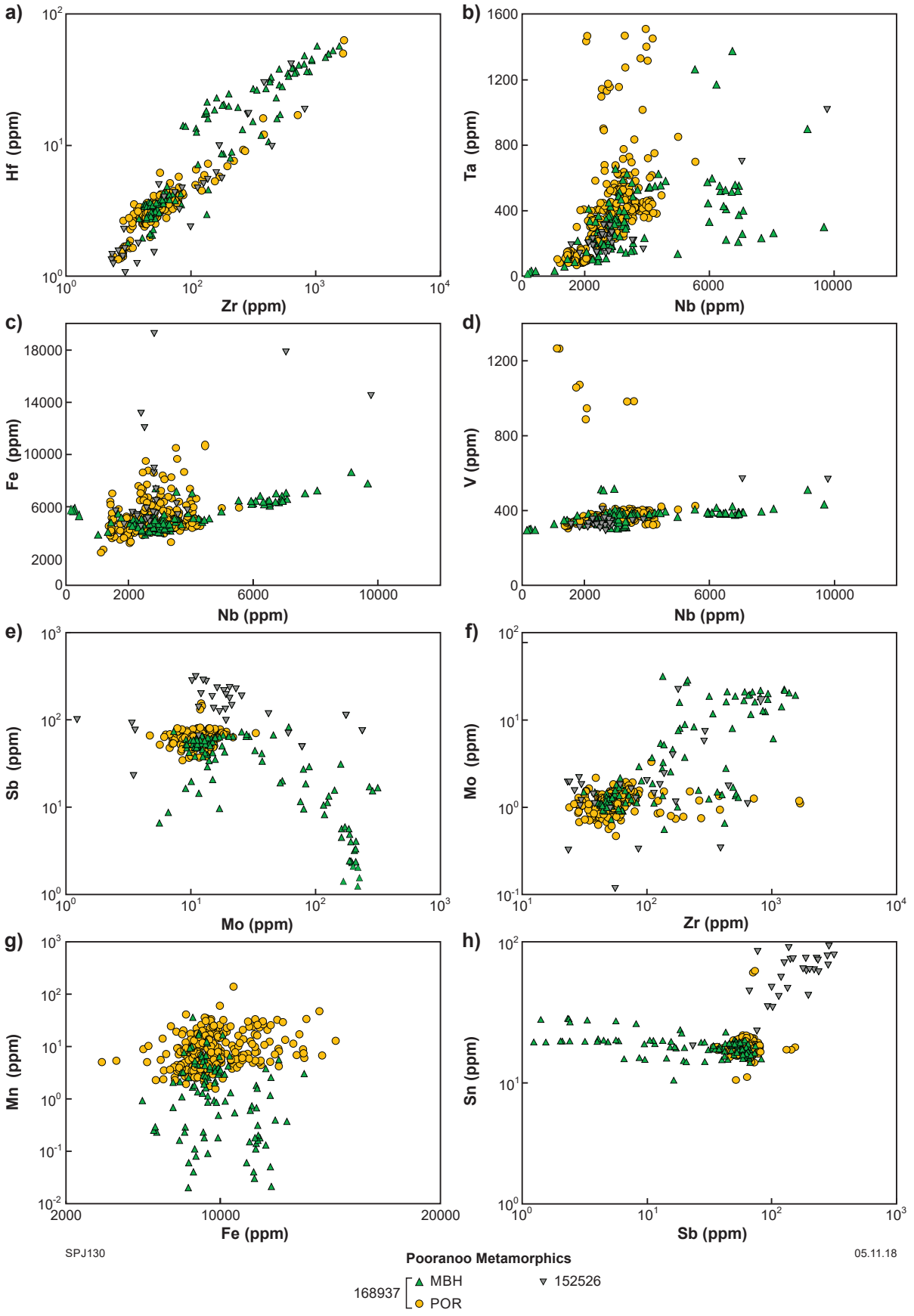

Figure 22. Binary trace element plots of rutile from the Pooranoo Metamorphics. Element concentrations are in parts per million (ppm)

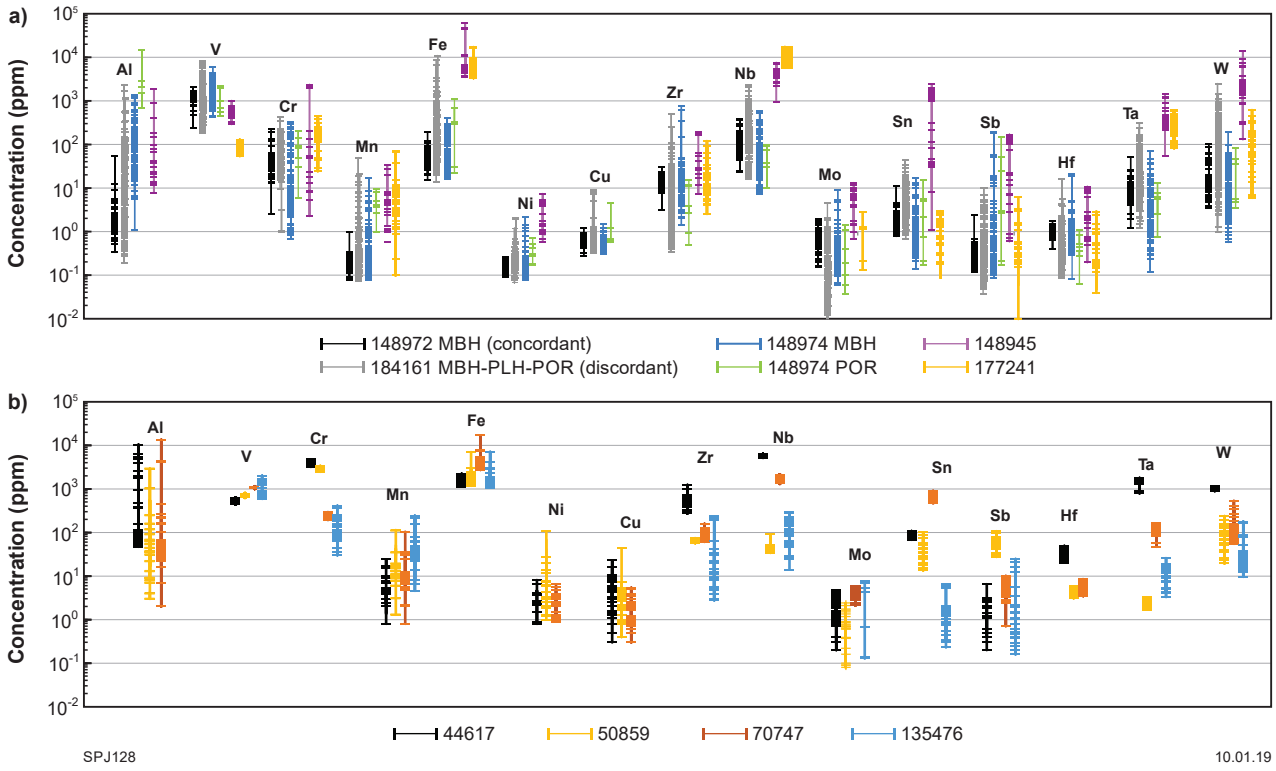

Figure 23. Trace element comparison of rutile from: a) Mount Augustus Sandstone (GSWA 148972), Ullawarra Formation (GSWA 148974), Irregully Formation (GSWA 148945 and 177241); b) Warrigal Gneiss (GSWA 44617), Bryah Group (GSWA 50859), Dalgaringa Supersuite metasiltstone (GSWA 70747) and Yarlarweelor Gneiss Complex (GSWA 135476)

On the Cr vs Nb plot of Zack et al. (2002, 2004), rutile grains from GSWA 148972 plot mainly in the 'metapelitic' field (Fig. 17d). The greatest variation between textures is seen for V, Cr and Sb (Fig. 23). Multiple spots on some large metamorphic rutile grains with variable BSE brightness (such as GSWA 148972, grain R1gr16, Fig. 8a) plot in both metamafic and metapelitic fields of the Cr vs Nb discrimination diagram (Fig. 17e). These grains also show zonation of V that increases with increasing Nb and decreasing Cr concentrations (Fig. 17e). This suggests care should be taken when interpreting source provenance for rutile using only Nb and Cr.

1673–1455 Ma Edmund Group

Binary diagrams for GSWA 148974, 172241 and 148945 show positive correlations between Nb and Fe for all textures and samples, suggesting a coupled substitution (Fig. 24a,b,c). On the Sb vs Zr plot, GSWA 148974 shows a negative correlation similar to that observed for MBH rutile in GSWA 148972 (Fig. 24h).

Antimony concentrations are higher and more variable in GSWA 148974 (0.09 – 190 ppm) compared to GSWA 148972 (largely <1 ppm for MBH, PBH and POR grains, and up to 10 ppm in MBH discordant grains, Fig. 23). Low concentrations of V and W are present in GSWA 172241 with respect to the other samples (Fig. 24e,f).

On the Cr vs Nb plot, rutile grains from GSWA 172241 and 148945 plot mainly in the 'metapelitic' field (Fig. 17d), similar to POR rutile from GSWA 148972. MBH rutile from GSWA 148974 plots across the metamafic–metapelitic boundary. This variability suggests mixed mafic–felsic sources of sediment. Ratios of elemental pairs Nb/Ta and Zr/Hf for all samples plot mainly in the subchondritic field, with a greater proportion of grains from GSWA 148974 plotting in the superchondritic field (Fig. 19d), indicating an overall preferential distribution of Ta in rutile.

Other samples

2758–2585 Ma Warrigal Gneiss

Rutile from Warrigal Gneiss sample GSWA 44617 has subchondritic Nb/Ta and Zr/Hf values (Fig. 19), and in the Nb vs Cr plot, straddles the boundary between metapelitic and metamafic fields (Fig. 17f).

2014–1920 Ma Bryah Group

In the Ti–100(Fe+Cr+V)–1000(W) and Ti–100(Fe+Cr+V)–1000(Sn) plots, rutile from Bryah Group sample GSWA 50859 plots between the fields of unmineralized and mineralized fields (Fig. 18d). This sample has near-chondritic Nb/Ta and largely subchondritic Zr/Hf (Fig. 19e). The rutile plots in the metamafic field of the Nb vs Cr plot (Fig. 17f).

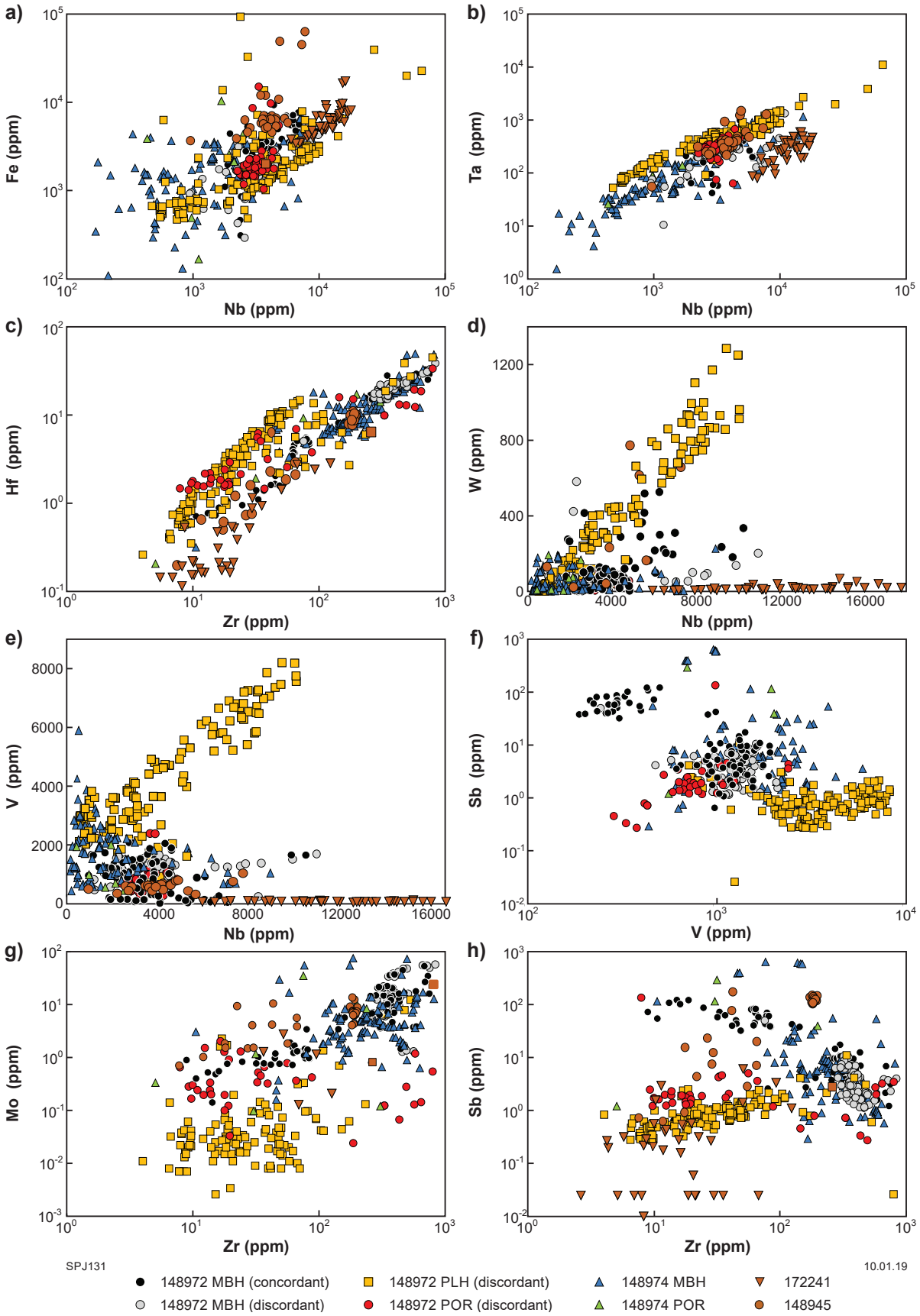

Figure 24. Binary trace element plots of rutile from Edmund Group samples (GSWA 148972, 148974, 172241 and 148945)

2005–1975 Ma Dalgaringa Supersuite

In the Ti–100(Fe+Cr+V)–1000(W) plot, rutile from Dalgaringa Supersuite sample GSWA 70747 plots between the fields of unmineralized and mineralized fields, but due to relatively high Sn concentrations it plots in the mineralized field of the Ti–100(Fe+Cr+V)–1000(Sn) diagram (Fig. 18d). Rutile from this sample has near-chondritic Nb/Ta and largely subchondritic Zr/Hf (Fig. 19e) and plots in the metapelitic field of the Nb vs Cr plot (Fig. 17f).

Trace element vs age evolution

By combining U–Pb ages and trace element compositions of rutile, it is possible to build time–composition plots (Fig. 25). These plots are interpreted to reflect the metal content of fluids and melts related with rutile-forming thermal events spanning a time range from the Mesoarchean to the Neoproterozoic and are used here for first-order considerations. The distribution of rutile ages appears to reflect major thermal events, such as the 1680–1620 Ma Mangaroon Orogeny (samples from the Edmund Group); the 1321–1171 Ma Mutherbukin Tectonic Event (samples from the Moogie Metamorphics); the 930–750 Ma Kuparr Tectonic Event (samples from the Moogie Metamorphics, GSWA 187403; and the Dalgaringa Supersuite, GSWA 70747). However, some ages do not correspond to known events. Rutile from Warrigal Gneiss sample GSWA 44617 recorded an apparent amphibolite-facies event at c. 1906 Ma that falls between the Glenburgh and Capricorn Orogenies, and cannot be attributed to either of the two, though it may reflect cooling ages associated with the Glenburgh Orogeny. The overall decrease of calculated rutile temperatures across the Proterozoic seems to reflect the history of the Capricorn Orogen, from high-temperature tectono-magmatic events related to collision; to younger, cooler and less well-defined tectonic events of the late Mesoproterozoic and early Neoproterozoic.

Element maps

Maps of element distribution in the western Capricorn Orogen have been obtained by plotting geographically constrained rutile element concentrations (Fig. 26). The values have been interpolated using the software ioGAS (the parameters used are: cell size = 1100, search radius = 50, minimum smoothing radius = 25). The map of temperatures was calculated based on Zr-in-rutile concentrations according to Tomkins et al. (2007). In these maps, high values of Mo, Sn and W coincide with the granitic rocks of the Moorarie Supersuite, particularly in the Limejuice Zone (Fig. 2). The map of calculated temperatures shows two peaks, with one coinciding with the Mo, W and Sn peaks in the Moorarie Supersuite. The highest Sb and U concentrations were measured in metamorphic rocks: the Moogie Metamorphics and Pooranoo Metamorphics, in the Mooloo Zone (Fig. 2). The distribution of these elements describes a gradient with increasing Sb and U northwards towards the Chalba Shear Zone. Antimony concentrations define a northwest–southeast-oriented low along the Mangaroon and Limejuice Zones. Overall, the scale of the area investigated and the wide spacing of samples may have resulted in significant approximations. This is visible, for example, in gradients crosscutting major structural discontinuities. However, the main northwest–southeast-oriented structural trends are reflected in the geochemical trends, confirming the validity of the method.

Discussion

Rutile geochronology

U–Pb geochronology on rutile grains from the 2240–2125 Ma Moogie Metamorphics yielded a range of metamorphic ages between c. 1890 and 870 Ma (Fig. 9). GSWA 184160 and 184161 contained high concentrations of common Pb, with U–Pb discordia lines yielding poorly defined intercepts at c. 1100 Ma. The Zr-in-rutile thermometer, however, yielded a uniform temperature for both samples of approximately 400°C (Fig. 9), possibly indicating modification of primary rutile during greenschist-facies metamorphism and deformation, most likely associated with the formation of chlorite (Fig. 3a–c). The quartzite sample (GSWA 187403) yielded a range of concordant dates between c. 1200 and 850 Ma, with a discrete mode at c. 870 Ma (Fig. 9). The older rutile grains are largely euhedral and belong largely to the MBH textural group (Fig. 5c). The spread of analyses along concordia between c. 1200 and 850 Ma may represent c. 1200-Ma-aged or older grains that were variably reset by a younger event at c. 870 Ma. The youngest <5% concordant analyses yielded a $^{206}Pb/^{238}U$ date of 871 ± 3 Ma that coincides with the low-grade 930–750 Ma Kuparr Tectonic Event (Occhipinti, 2007; Occhipinti and Reddy, 2009; Cutten and Johnson, 2018; Piechocka et al., 2018). The Zr-in-rutile thermometer suggests this overprint is associated with an increase of W, Nb, Ta and Fe (Figs 10 and 15a). The addition of these elements is also accompanied with a decrease in Nb/Ta ratios in the brightest (BRH) grains (Fig. 16d) with the rate of increase of Ta greater than that of Nb. Fractionation of Nb from Ta and the associated decrease in Nb/Ta ratio has commonly been reported for rutile equilibrated in the presence of fluids (Green, 1995; Dostal and Chatterjee, 2000). Rutile from GSWA 216806 yielded a concordant date of c. 1890 Ma and Zr-in-rutile average temperature of 674°C. This age is significantly younger than the 2005–1950 Ma Glenburgh Orogeny (Kinny et al., 2004; Occhipinti et al., 2004; Sheppard et al., 2004; Johnson et al., 2011b), and cannot be directly correlated with any of the main tectono-thermal events in the Capricorn Orogen.

Rutile from GSWA 190607 and 190608 of the 1840–1810 Ma Leake Spring Metamorphics yielded $^{238}U/^{206}Pb$ dates, mostly between c. 1160 and 850 Ma (Appendix Fig. 5). The age mode at c. 900 Ma can be interpreted as a metamorphic event re-setting pre-existing rutile with ages as old as c. 1160 Ma or older. The temperature of ~550°C is constant at different ages, and may be inherited from these previous events, rather than relating to peak temperatures during the overprinting 930–750 Ma Kuparr Tectonic Event.

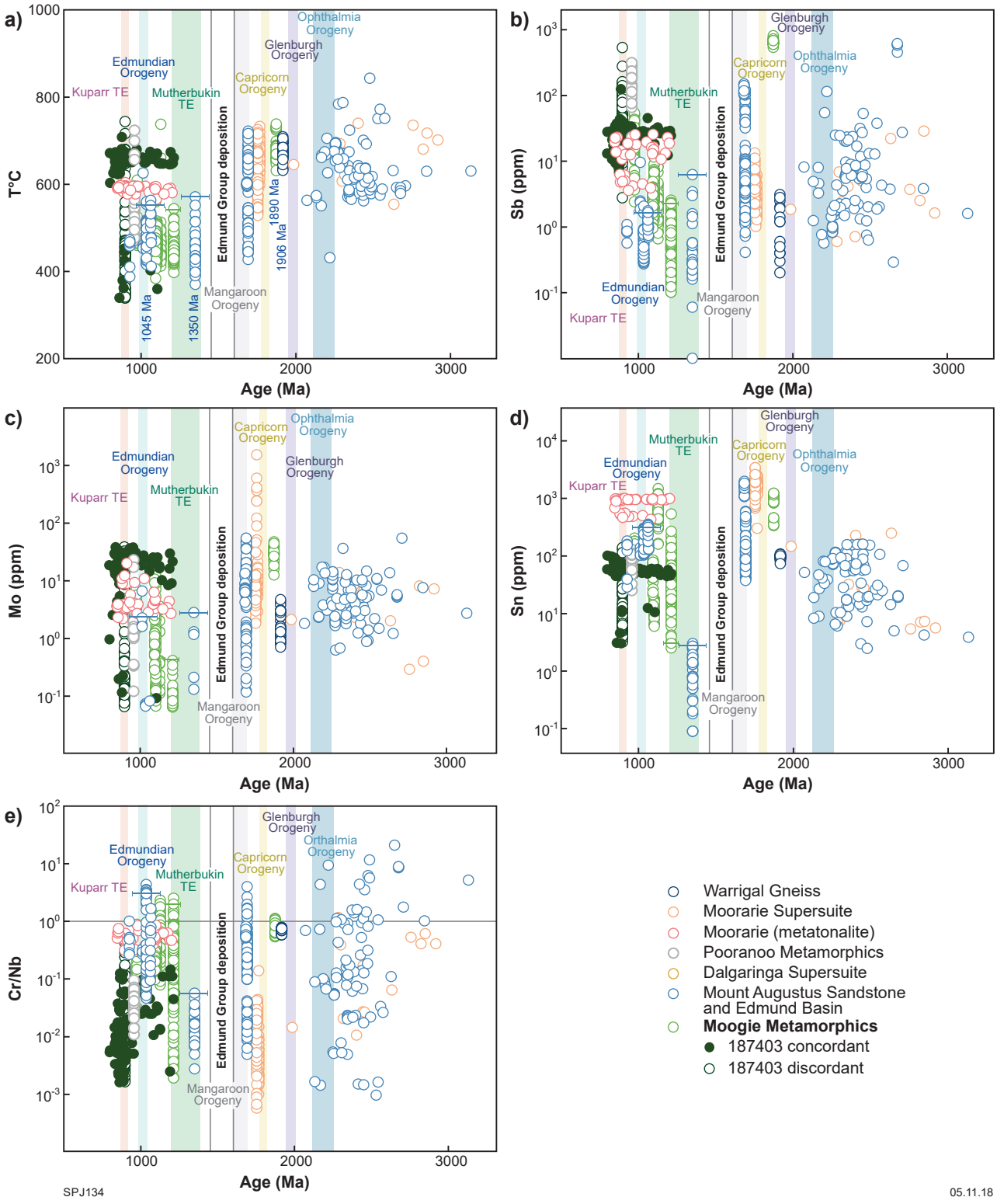

Figure 25. Plots of trace elements and Zr-in-rutile temperature vs U–Pb age of rutile from the Capricorn Orogen. Vertical coloured bars indicate tectonic events as labelled

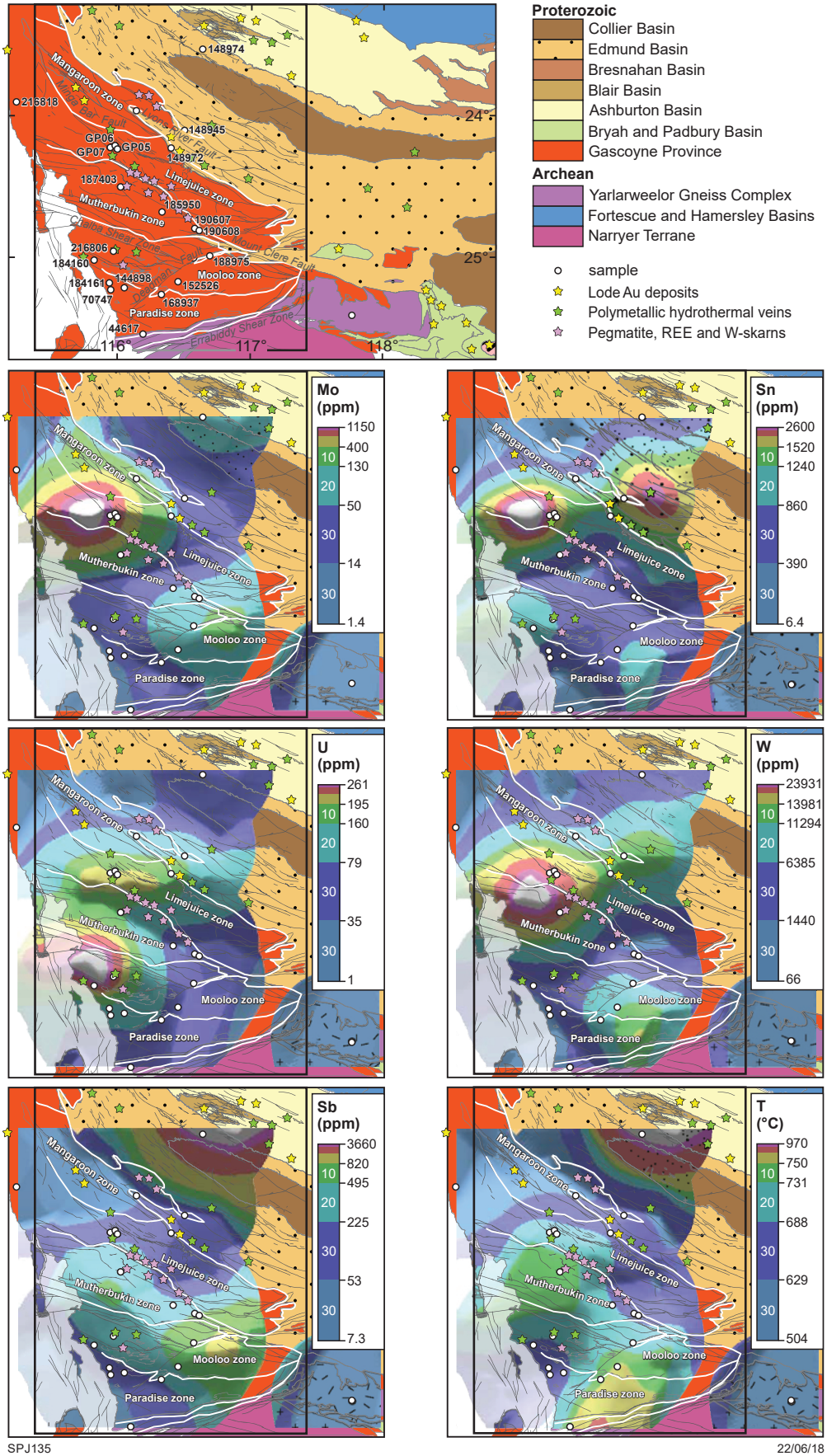

Figure 26. Maps of element concentrations in rutile from the western Capricorn Orogen. Equilibration temperature of rutile was calculated from Zr content (Tomkins et al., 2007). The boxed area indicates the study area location, indicated in Figure 2

The ages of rutile from samples DP14-GP05, DP14-GP06 and DP14-GP07 (1774–1761 Ma) of the 1820–1775 Ma Moorarie Supersuite overlap with, or are slightly younger than, the age of emplacement of the Moorarie Supersuite magmatic rocks as defined by the magmatic zircons (Sheppard et al., 2010b). The spread of calculated rutile temperatures (530–730°C) is slightly lower than zircon saturation temperatures calculated from whole-rock compositions of the Moorarie Supersuite samples (700–900°C), and possibly records progressive cooling during the transition from the orthomagmatic to hydrothermal stage, which is also suggested by the interstitial textures of rutile in these samples. High Sn, Mo and W concentrations in rutile are compatible with crystallization from a fractionated felsic magma and related hydrothermal fluids.

Ten rutile grains from Moorarie Supersuite biotite metatonalite (GSWA 188975) yielded a spread of concordant U–Pb dates with distinct age components from the Mesoarchean to Paleoproterozoic (2900–2200 Ma; Fig. 11). All other rutile analyses, as well as anatase, are strongly discordant. The spread in dates and trace element contents, along with distinct rutile textures, suggest the presence of inherited rutile. Previous U–Pb analyses of zircon (Wingate et al., 2011) indicated an igneous age of c. 1804 Ma and inherited zircon dates spanning back to the early Paleoproterozoic, with a few Meso- to Paleoarchean zircon grains (3526–1887 Ma). Our analyses suggest that rutile did not record the c. 1804 Ma magmatic event, but appears to have preserved the older dates that overlap with previous zircon analyses — in particular, the dates between c. 2400 and 2200 Ma.

The 1760–1680 Ma Pooranoo Metamorphics yielded largely discordant analyses that show a spread in ratios on the Tera-Wasserburg plots (Fig. 12a). GSWA 152526 yielded a discordia age of c. 960 Ma, comparable to ages calculated for some Moogie Metamorphics samples. The available geochronological record (Nelson, 2001) reports formation of rutile as mineral aggregates along margins of recrystallized quartz grains. This suggests possible formation and recrystallization of detrital rutile during metamorphism and the associated formation of rutile aggregates giving rise to the 'porous' grain component with high concentration of common Pb and younger lower intercept dates.

Rutile with MBH textures from Mount Augustus Sandstone sample GSWA 148972, as well as from GSWA 148945 from Depositional Package 1 of the Edmund Group, yielded a distinct age mode at c. 1680 Ma. This date is similar to the maximum depositional age of c. 1679 Ma obtained from detrital zircons from the Mount Augustus Sandstone sample (Martin et al., 2008). Maximum temperatures calculated for these concordant rutiles are 600–700°C and could have been derived from either felsic magmatic rocks of the 1680–1620 Ma Durlacher Supersuite or as metamorphic grains associated with the high-temperature 1680–1620 Ma Mangaroon Orogeny (Sheppard et al., 2005). The two samples also contain strongly discordant, lower temperature analyses at 400–550°C, likely representing partially reset rutile. Within GSWA 148972, a separate component of rutile grains, including patchy brightness (PBH) and porous (POR) grains, has strongly discordant ages clustering at around c. 1100 Ma (Fig. 13). This group of dates suggests a low-grade metamorphic event during the late Mesoproterozoic. Zr-in-rutile estimates suggest temperatures of 400–550°C; however, these results are unlikely considering that the Mount Augustus Sandstone shows no evidence of metamorphism. Temperature overestimates from Zr-in-rutile geothermometry applied to low-T rocks have been described previously (Cabral et al., 2015). The timing of the low-grade metamorphism or hydrothermal alteration is contemporaneous with the 1030–955 Ma Edmundian Orogeny, which resulted in the deformation of the Edmund Group and reactivation of crustal-scale faults, such as the Talga and Lyons River Faults, close to the sample (Cutten et al., 2016).

Imprecise dates of c. 1300 Ma were obtained from discordant rutile in GSWA 172241, also from Depositional Package 1 of the Edmund Group. These dates broadly overlap the timing of the 1321–1171 Ma Mutherbukin Tectonic Event (Korhonen et al., 2015, 2017). Zr-in-rutile temperature estimates suggest formation mostly in the range 390–490°C. The highly altered, low- to medium-grade metamorphic nature of GSWA 172241, is consistent with the rutile thermometry. This sample is located in the northern part of the Mangaroon Zone (Fig. 2) that was affected by alkaline metasomatic fluids during the emplacement of the c. 1300 Ma Gifford Creek ferrocarbonatite (Pirajno et al., 2014).

GSWA 148974 from the Ullawarra Formation, yielded a spread of concordant analyses between c. 3170 and 2020 Ma, with major age modes present at c. 2675, 2454, 2345 and 2275 Ma (Fig. 14). Rutile grains were largely present in the clay-rich matrix (Fig. 4d) and likely represent a detrital component. The dominance of Paleoproterozoic to Archean detrital zircons is also present in the sample, although the two younger rutile age modes, at c. 2345 and 2275 Ma, have not been identified in the zircon detritus (Johnson et al., 2018). The main paleocurrent vector for the sample indicates that detritus was derived from the northwest (Martin et al., 2008) and, together with the older detrital rutile and zircon grains at c. 2675 and 2450 Ma, suggests that the Hamersley and Fortescue Groups, along with the northern margin of the Gascoyne Province, are the likely source for the detritus (Martin et al., 2008; Johnson et al., 2018). In contrast, the variable Nb–Cr compositions of the younger detrital rutile suggest sourcing from a variety of mafic and felsic sources (Fig. 17), for which there is no accompanying zircon detritus (Fig. 14).

Rutile from the 2758–2585 Ma Warrigal Gneiss quartzite (GSWA 44617) yielded a date of c. 1917 Ma and temperatures of 630–710°C. These data may reflect cooling associated with the 2005–1950 Ma Glenburgh Orogeny.

Trace element geochemistry

Trace element geochemistry of TiO_2 is dependent on many factors, including, but not limited to: primary rock/fluid composition (van Gaans et al., 1995; Zack et al., 2002, 2004; Scott and Radford, 2007); oxygen fugacity affecting mainly the incorporation of polyvalent cations (Urban et al., 1992; Liu et al., 2014); pressure and temperature (Jenner et al., 1993; Brenan et al., 1994; Cherniak et al., 2007; Tomkins et al., 2007; Meyer et al., 2011); and polymorph type (Triebold et al., 2011). On an atomic level, the abundance of oxygen vacancies, ionic radius,

presence of H_2O, saturation of trace elements in solution (Henry's Law) and Ti substitution play a major role in controlling the incorporation of trace elements into the rutile crystal lattice (Fromknecht et al., 1996; Meyer et al., 1997, 1998; Lucassen et al., 2013). Therefore, the final trace element concentrations are controlled by the interplay of both geological and atomic-scale factors. Samples analysed in this study come from a range of metamorphic, igneous and sedimentary rocks, so a generalized process-based evaluation of trace element incorporation in rutile is difficult to assess. However, a number of first-order observations can be made for individual rock packages, as well as between different polymorph types.

The lowest concentrations for all samples were observed for largely divalent to trivalent cations Mn, Ni and Cu (Figs 15 and 23). The greatest variation in concentrations was observed for polyvalent cations V, W, Al, Cr, Fe, Mo, Sn and Sb, with monovalent cations Nb and Ta as well as Zr and Hf showing coupled behaviour across all samples, whereas their relative abundance is different between the various textures in the same sample and between different rock types. In many samples, Nb shows a positive correlation with Fe (Figs 16, 21, 22 and 24) suggesting a coupled substitution of $Fe^{3+} + Nb^{5+} \leftrightarrow 2Ti^{4+}$ (Meinhold, 2010). In several analyses, a strong deviation from the 1:1 line in the Nb vs Fe plot towards higher Fe contents is likely due to the presence of Fe–(Ti) oxide. Also, deviation from this trend, such as in the samples from the Moorarie Supersuite (Fig. 21), could reflect the reduced valance state of Fe(2+). This is confirmed by the fact that some grains show ilmenite lamellae and micro-inclusions (Fig. 8b) which can affect the Fe concentrations. The flat signals of Zr, Nb, W, Ta, Sb, Sn, and in most cases Mo, suggest that all these elements are contained in the structure of rutile, or in sub-microscopic inclusions, which cannot be resolved by LA-ICPMS. However, some analyses, for example in GSWA 148974 of the Edmund Group, have unusually high Zr concentrations (>1000 ppm) that plot separately from other analyses. These high Zr values were not used for Zr-in-rutile calculations. In addition, high Fe content uncorrelated with Nb is interpreted as being due to Fe inclusions. Therefore, outliers with the highest Fe contents were not plotted in discrimination diagrams (Fig. 18). Thorium is typically very low in our analyses, confirming the typically low Th contents of rutile (e.g. Zack et al., 2011). Some samples, however, have irregular LA-ICPMS patterns with co-occurring spikes of Th and ^{208}U, which suggest the presence of Th-bearing inclusions. Thus, we interpret the presence of Th in some analyses as the consequence of inclusions, despite an attempt to avoid these inclusions during recalculation of analyses.

Lower Zr-in-rutile temperatures are most common in grains associated with the highest degree of discordance and are accompanied by low-U concentrations at lower temperatures. A positive correlation between Zr and hexavalent cations (Mo, W and U) is present in rutile from most samples, particularly with textures associated with patchy brightness (PBH) due to higher concentrations of Fe, W, Nb and Ta, with exceptions being detrital rutile grains from the Edmund Group. The exact mechanism for incorporation of hexavalent elements at higher temperatures (associated with high Zr) and/or in the presence of a fluid has not been previously reported, but in order to preserve charge balance, a coupled substitution of hexavalent and divalent cations: $(Fe, V, Mn)^{2+} + (Mo, W, U)^{6+} \leftrightarrow 2Ti^{4+}$ may offer a possible solution. Another possibility is the coupled substitution $(Zr, Hf)^{4+} + 2(Mo, W, U)^{6+} \leftrightarrow 4Ti^{4+}$ which, however, would introduce a point defect (vacancy).

Zr-in-rutile geothermometry

Zr-in-rutile geothermometry is applicable to zircon- and quartz-bearing assemblages. This includes the majority of our samples, when metamorphic rutile is considered. However, the results of this method are uncertain when applied to detrital rutile, as the composition of the source rock cannot be ascertained. The Nb–Cr compositions of some samples (e.g. GSWA 148972 and 148974 from the Edmund Group, Fig. 17d) suggest provenance from mafic sources; therefore, the temperature estimates of these grains should be considered as unreliable and have not been considered further.

Rutile as an indicator of mineralization

Anomalous concentrations of Fe, W, V, Sn, Sb and Mo (between 0.2–5 wt.%) have been reported from various gold-related deposits around the world (Clark and William-Jones, 2004; Scott and Radford, 2007; Meinhold, 2010; Scott et al., 2011). Although only some samples show anomalous compositions between different deposits, concentrations of Fe, V, Cr, W and Sn were used by Clark and William-Jones (2004) in order to differentiate samples based on their association with barren, altered and mineralized host rock (Fig. 18). Outliers with Fe contents uncorrelated with Nb, which are interpreted to contain Fe-rich inclusions, were not plotted in these diagrams (e.g. GSWA 148972 and 148945). In the plot of temperature, detrital rutile with Nb–Cr compositions plotting in the metamafic field was also omitted.

High concentrations of W measured in samples of the Moogie Metamorphics (up to 2.9 wt.% WO_3, GSWA 187403), Pooranoo Metamorphics and other units would suggest association with mineralization when plotted in the diagrams of Clark and William-Jones (2004) (Fig. 18). To date, no known gold-mineralization has been reported in that area. A number of W, Mo and Nb occurrences have been reported immediately to the north of GSWA 187403 (Nardoo Creek, GSWA MINEDEX database) and close to GSWA 185950 (see Fig. 2, Mutherbuckin Zone), and generally along the Ti Tree Shear Zone, where W and Mo mineralization is prevalent (Pirajno et al., 2008). High concentrations of Mo, Sn and Win rutile, especially within rutile from Moorarie Supersuite samples DP14-GP05, DP14-GP06 and DP14-GP07, reflect this enrichment. Nevertheless, no known gold mineralization, or Mo, W and Nb occurrences have been reported elsewhere in proximity to other samples analysed in this study. Notwithstanding the lack of mineralization associated with these samples, the majority of analyses plot in the field of 'rutile from ore zone' when W is used at the right apex of the ternary diagrams (Fig. 18). Therefore, given the possibility of false positives, this diagram should be used with care. Furthermore, anatase and brookite (Fig. 18b) plot largely in the 'unaltered wallrock rutile' field and suggest a polymorph-type control on the distribution of various trace elements. When Sn is used at the right apex of the diagrams of Clark and William-Jones (2004), the majority of analyses plot in the 'unaltered wallrock rutile'

field. However, this is highly dependent on the type of mineralization and the associated fluids and, as is evident in Figure 18, a clear distinction cannot be made for some samples. Furthermore, the concentration of Ti is not only dependent on elements represented in the ternary diagrams, but on the concentrations of Nb and Ta, which can be up to 100 000 ppm (~14 wt.% Nb_2O_5) in the brightest grains analysed during this study (Fig. 15a).

Trace element variations between polymorphs

The three different types of polymorphs observed in the Moorarie Supersuite have quite different trace element geochemistry, whereas the greatest variation observed for Al, Cr, Fe, Sb, Sn and V. Iron and Al are enriched in brookite, while Cr, Sb and Sn are enriched in rutile. Anatase typically displays intermediate values between rutile and brookite (Fig. 20a). Triebold et al. (2011) detected similar variations in rutile grains from detrital and metamorphic rocks, with greatest variations for Cr, Nb, Fe, Sn, V and Zr. They established a linear discriminant analysis in order to distinguish between TiO_2 polymorphs based on the chemistry. When using the linear discriminant analysis, anatase grains are largely classified as brookite (probabilities typically around 95–100%), whereas 90–95% of brookite and rutile grains were classified correctly. Although the Triebold et al. (2011) linear discriminant analysis works well for detrital and metamorphic rocks, it may not work well for igneous rocks, particularly when discriminating anatase. Until a better evaluation tool for igneous rocks can be developed, we strongly encourage distinguishing of TiO_2 polymorphs using the EBSD method.

On the Nb vs Cr plot of Zack et al. (2002, 2004), the majority of analyses plot in the metapelitic field (Fig. 17), suggesting largely pelitic sources for rutile. In contrast, Edmund Group samples show a mixture of mafic and pelitic sources, which is in agreement with having been derived from the southern Pilbara (mafic?) sources (Johnson et al., 2018). Rutile from an ultramafic GSWA 50859 of the Bryah Group plots within the metamafic field, and mafic rocks of the Warrigal Gneiss (GSWA 44617) plot at the boundary between the two fields (Fig. 17f). However, care should be taken when interpreting these diagrams as a single grain in the Mount Augustus Sandstone (GSWA 148972, grain R1gr16) yielded values of Nb and Cr that cross the divisional line between metamafic to metapelitic sources (Fig. 17e).

The Nb, Ta and Nb/Ta budgets are strongly controlled by titanium-rich phases, of which rutile is significant, so that even small modal proportions of residual rutile in eclogite residue can significantly affect the total Nb and Ta budgets of arc magmas above subduction zones (Green and Pearson, 1987; Foley et al., 2000; Rudnick et al., 2000; Schmidt et al., 2009). Subchondritic Nb/Ta ratios – chondritic Nb/ Ta ~17.5 (Hofmann et al., 1986; Sun and McDonough, 1989; Green, 1995) occur mostly in continental crust and depleted mantle (Barth et al., 2000; Rudnick et al., 2000), whereas the superchondritic reservoir is proving to be more elusive (Green, 1995; Schmidt et al., 2009). The majority of samples analysed show subchondritic Nb/Ta and Zr/Hf values (Fig. 19), except for the Moorarie Supersuite (Fig. 19b) where the majority of the analyses have superchondritic values for both Nb/Ta and Zr/Hf. Although subchondritic Nb/Ta values in rutile are common in melts equilibrated with rutile (Foley et al., 2000) and strongly fractionated felsic melts (Antipin et al., 2006), as well as rutile equilibrated in the presence of a fluid (Dostal and Chatterjee, 2000), Zr/Hf ratios of rutile are strongly affected by fractionation in the presence of clinopyroxene and, to a lesser degree, garnet and/or equilibration in the presence of a fluid (David et al., 2000; Ewing et al., 2014). This may explain a large variation in Zr/Hf values in the Moorarie Supersuite. The Zr/Hf ratio decreases with zircon fractionation, a characteristic that has been observed in A-type felsic magmas (Agangi et al., 2012), which may also explain subchondritic Zr/Hf in rutile crystallizing in the presence of zircon in igneous samples.

Conclusions

The main outcomes of this study are summarized below:

- Rutile is sensitive to changing fluid and temperature conditions, particularly where temperatures are not high enough to reset zircon grains and where dissolution of zircon does not allow for the tectono-thermal or fluid event to be detected. In this instance, the LASS-ICPMS method proves to be very useful in detecting changes of elements over time.
- Concentrations of Zr and U are correlated, and analyses with low U (1 ppm or less), typically yield highly discordant U–Pb results. The closure temperature of Pb in rutile is believed to be lower than the closure temperature of Zr. This may result in a decoupling and opening of the U–Pb system during a metamorphic event (T = 500–600°C), whereas the Zr concentrations can preserve temperature information of a previous high-temperature event.
- Anatase and brookite do not contain any U, have very low Zr concentrations, and cannot be used for U–Pb dating or Zr-in-rutile thermometry.
- The Nb vs Cr diagrams for discrimination of metamafic vs metapelitic source provenance should be used with care, as single grains can show variation between the two types of sources. Furthermore, higher Cr concentrations in anatase and rutile, when compared with brookite, can skew the data, so polymorph discrimination is paramount.
- The different types of polymorphs as detected in the Moorarie Supersuite show variable chemistries of Fe, Cr, V, Sb, Sn and Al, so polymorph distinction is essential when using chemistry of rutile in discrimination of distal footprints of mineralizing ore systems.
- This regional-scale study shows large differences in trace element composition of rutile grains from different types of rocks, but can provide complementary information regarding lower-temperature events that affected the Capricorn Orogen, with the best example provided by the U–Pb geochronology and geochemistry of the Moogie Metamorphics samples.

- An integrated EBSD, SEM and LASS approach offers a powerful analytical combination in successfully characterizing chemical and mineralogical changes of TiO_2 in association with mineralized ore systems.

Acknowledgements

We would like to thank GSWA for providing the samples and heavy mineral separates. In particular, many thanks to Simon Johnson who provided an invaluable overview of the Capricorn Orogen geology and who was always there to help with organizing fieldwork and addressing queries. Furthermore, we thank the team at the University of Santa Barbara for setting up the analytical method, especially Andrew Kylander-Clark for offering help at any hour of the day. Thanks also to Elaine Miller from the Microscopy and Microanalysis Facility, John de Laeter Centre, Curtin University for her support and training on the SEM instruments. This study is funded by the Science and Industry Endowment Fund (SIEF).

References

Agangi, A, Kamenetsky, VS and McPhie, J 2012, Evolution and emplacement of high fluorine rhyolites in the Mesoproterozoic Gawler silicic large igneous province, South Australia: Precambrian Research, v. 208–211, p. 124–144.

Antipin, VS, Savina, EA and Mitichkin, MA 2006, Geochemistry and formation conditions of rare-metal granites with various fluorine-bearing minerals (fluorite, topaz, and cryolite): Geochemistry International, v. 44, p. 965–975.

Barth, MG, McDonough, WF and Rudnick, RL 2000, Tracking the budget of Nb and Ta in the continental crust: Chemical Geology, v. 165, p. 197–213.

Bodorkos, S and Wingate, MTD 2007, The contribution of geochronology to GSWA's mapping programs: current perspectives and future directions, in GSWA 2007 extended abstracts: promoting the prospectivity of Western Australia: Geological Survey of Western Australia, Record 2007/2, p. 10–11.

Brenan, JM, Shaw, HF, Phinney, DL and Ryerson, FJ 1994, Rutile-aqueous fluid partitioning of Nb, Ta, Hf, Zr, U and Th: implications for high field strength element depletions in island-arc basalts: Earth and Planetary Science Letters, v. 128, p. 327–339.

Cabral, AR, Rios, FJ, de Oliveira, LAR, de Abreu, FR, Lehmann, B, Zack, T and Laufek, F 2015, Fluid–inclusion microthermometry and the Zr-in-rutile thermometer for hydrothermal rutile: International Journal of Earth Sciences, v. 104, p. 513–519.

Cawood, PA and Korsch, RJ 2008, Assembling Australia: Proterozoic building of a continent: Precambrian Research, v. 166, no. 1–4, p. 1–38.

Cherniak, DJ, Manchester, J and Watson, EB 2007, Zr and Hf diffusion in rutile: Earth and Planetary Science Letters, v. 261, p. 267–279.

Clark, DJ, Hensen, BJ and Kinny, PD 2000, Geochronological constraints for a two-stage history of the Albany–Fraser Orogen, Western Australia: Precambrian Research, v. 102, no. 3, p. 155–183.

Clark, JR and Williams–Jones, AE 2004, Rutile as a potential indicator mineral for metamorphosed metallic ore deposits Rapport Final de DIVEX, Sous–project SC2, Montreal, Canada, 17 p.

Cutten, HN, Johnson, SP, Thorne, AM, Wingate, MTD, Kirkland, CL, Belousova, EA, Blay, OA and Zwingmann, H 2016, Deposition, provenance, inversion history and mineralization of the Proterozoic Edmund and Collier Basins, Capricorn Orogen: Geological Survey of Western Australia, Report 127, 74p.

Cutten, HN and Johnson, SP 2018, Kuparr Tectonic Event (KU): Geological Survey of Western Australia, WA Geology Online, Explanatory Notes extract, viewed 05 October 2018, <wwwdmpwagovau/ens>.

Daneu, N, Rečnik, A and Mader, W 2014, Atomic structure and formation mechanism of (101) rutile twins from Diamantina (Brazil): American Mineralogist, v. 99, p. 612.

David, K, Schiano, P and Allègre, CJ 2000, Assessment of the Zr/Hf fractionation in oceanic basalts and continental materials during petrogenetic processes: Earth and Planetary Science Letters, v. 178, p. 285–301.

Dostal, J and Chatterjee, AK 2000, Contrasting behaviour of Nb/Ta and Zr/Hf ratios in a peraluminous granitic pluton (Nova Scotia, Canada): Chemical Geology, v. 163, p. 207–218.

Evans, DAD, Sircombe, KN, Wingate, MTD, Doyle, M, McCarthy, M, Pidgeon, RT and Van Niekerk, HS 2003, Revised geochronology of magmatism in the western Capricorn Orogen at 1805–1785 Ma: Diachroneity of the Pilbara–Yilgarn collision: Australian Journal of Earth Sciences, v. 50, no. 6, p. 853–864.

Ewing, TA, Rubatto, D and Hermann, J 2014, Hafnium isotopes and Zr/Hf of rutile and zircon from lower crustal metapelites (Ivrea–Verbano Zone, Italy): Implications for chemical differentiation of the crust: Earth and Planetary Science Letters, v. 389, p. 106–118.

Foley, SF, Barth, MG and Jenner, GA 2000, Rutile/melt partition coefficients for trace elements and an assessment of the influence of rutile on the trace element characteristics of subduction zone magmas: Geochimica et Cosmochimica Acta, v. 64, p. 933–938.

Fromknecht, R, Khubeis, I and Meyer, O 1996, La-, Sn- and Hf-implanted in TiO_2 single crystals: lattice disorder and lattice site location: Nuclear Instruments and Methods in Physics Research Section B: Beam Interactions with Materials and Atoms, v. 116, p. 109–112.

Graham, J and Morris, RC 1973, Tungsten- and antimony-substituted rutile: Mineralogical Magazine, v. 39, p. 470–473.

Green, TH 1995, Significance of Nb/Ta as an indicator of geochemical processes in the crust–mantle system: Chemical Geology, v. 120, p. 347–359.

Green, TH and Pearson, NJ 1987, An experimental study of Nb and Ta partitioning between Ti-rich minerals and silicate liquids at high pressure and temperature: Geochimica et Cosmochimica Acta, v. 51, p. 55–62.

Hofmann, AW, Jochum, KP, Seufert, M and White, WM 1986, Nb and Pb in oceanic basalts: new constraints on mantle evolution: Earth and Planetary Science Letters, v. 79, p. 33–45.

Horn, M, Schwebdtfeger, CF, Meagher, EP 1972, Refinement of the structure of anatase at several temperatures: Z Krist, v. 136, p. 273–281.

Horwitz, RC and Smith, RE 1978, Bridging the Yilgarn and Pilbara Blocks: Precambrian Research, v. 6, p. 293–322.

Janssen, A, Putnis, A, Geisler, T and Putnis, CV 2010, The experimental replacement of ilmenite by rutile in HCl solutions: Mineralogical Magazine, v. 74, p. 633–644.

Jenner, GA, Foley, SF, Jackson, SE, Green, TH, Fryer, BJ and Longerich, HP 1993, Determination of partition coefficients for trace elements in high pressure–temperature experimental run products by laser ablation microprobe-inductively coupled plasma-mass spectrometry (LAM–ICP–MS): Geochimica et Cosmochimica Acta, v. 57, p. 5099–5103.

Johnson, SP 2013, The birth of supercontinents and the Proterozoic assembly of Western Australia: Geological Survey of Western Australia, 78p.

Johnson, SP, Cutten, HN, Tyler, IM, Korsch, RJ, Thorne, AM, Blay, OA, Kennett, BLN, Blewett, RS, Joly, A, Dentith, MC, Aitken, ARA, Goodwin, JA, Salmon, M, Reading, A, Boren, G, Ross, J, Costelloe, RD and Fomin, T 2011a, Preliminary interpretation of deep seismic reflection lines 10GA–CP2 and 10GA–CP3: crustal architecture of the Gascoyne Province, and Edmund and Collier Basins, *in* Capricorn Orogen seismic and magnetotelluric (MT) workshop 2011: extended abstracts *edited by* SP Johnson, AM Thorne and IM Tyler: Geological Survey of Western Australia, Record 2011/25, p. 49–60.

Johnson, SP, Kirkland, CL, Evans, NJ, McDonald, BJ, Cutten, HN 2018, The complexity of sediment recycling as revealed by common Pb isotopes in K-feldspar: Geoscience Frontiers, 9, p. 1515–1527

Johnson, SP, Korhonen, FJ, Kirkland, CL, Cliff, JB, Belousova, EA and Sheppard, S 2017, An isotopic perspective on growth and differentiation of Proterozoic orogenic crust: from subduction magmatism to cratonization: Lithos, v. 268–271, p. 76–86.

Johnson, SP, Sheppard, S, Rasmussen, B, Wingate, MTD, Kirkland, CL, Muhling, JR, Fletcher, IR and Belousova, EA 2011b, Two collisions, two sutures: punctuated pre-1950 Ma assembly of the West Australian Craton during the Ophthalmian and Glenburgh Orogenies: Precambrian Research, v. 189, no. 3–4, p. 239–262.

Johnson, SP, Sheppard, S, Wingate, MTD, Kirkland, CL and Belousova, EA 2011c, Temporal and hafnium isotopic evolution of the Glenburgh Terrane basement: an exotic crustal fragment in the Capricorn Orogen: Geological Survey of Western Australia, Report 110, 27p.

Johnson, SP, Thorne, AM, Tyler, IM, Korsch, RJ, Kennett, BLN, Cutten, HN, Goodwin, J, Blay, OA, Blewett, RS, Joly, A, Dentith, MC, Aitken, ARA, Holzschuh, J, Salmon, M, Reading, A, Heinson, G, Boren, G, Ross, J, Costelloe, RD and Fomin, T 2013, Crustal architecture of the Capricorn Orogen, Western Australia and associated metallogeny: Australian Journal of Earth Sciences, v. 60, no. 6–7, p. 681–705.

Kinny, PD, Nutman, AP and Occhipinti, SA 2004, Reconnaissance dating of events recorded in the southern part of the Capricorn Orogen: Precambrian Research, v. 128, p. 279–294.

Kirkland, CL, Wingate, MTD, Bodorkos, S and Sheppard, S 2009, 184161: quartzofeldspathic migmatite, Mount Dalgety; Geochronology Record 835: Geological Survey of Western Australia, 4p.

Korhonen, FJ and Johnson, SP 2015, The role of radiogenic heat in prolonged intraplate reworking: The Capricorn Orogen explained?: Earth and Planetary Science Letters, v. 428, p. 22–32.

Korhonen, FJ, Johnson, SP, Fletcher, IR, Rasmussen, B, Sheppard, S, Muhling, JR, Dunkley, DJ, Wingate, MTD, Roberts, MP and Kirkland, CL 2015, Pressure–temperature–time evolution of the Mutherbukin Tectonic Event, Capricorn Orogen: Geological Survey of Western Australia, Report 146, 64p.

Korhonen, FJ, Johnson, SP, Wingate, MTD, Kirkland, CL, Fletcher, IR, Dunkley, DJ, Roberts, MP, Sheppard, S, Muhling, JR and Rasmussen, B 2017, Radiogenic heating and craton–margin plate stresses as drivers for intraplate orogeny: Journal of Metamorphic Geology, v. 35, no. 6, p. 631–661.

Kylander-Clark, ARC 2008, Slow subduction and exhumation of a thick ultrahigh-pressure terrane: Western Gneiss Region, Norway: University of California, Santa Barbara, 121 p.

Kylander-Clark, ARC, Hacker, BR and Cottle, JM 2013, Laser-ablation split-stream ICP petrochronology: Chemical Geology, v. 345, p. 99–112.

Liu, L, Xiao, Y, Aulbach, S, Li, D and Hou, Z 2014, Vanadium and niobium behavior in rutile as a function of oxygen fugacity: evidence from natural samples: Contributions to Mineralogy and Petrology, v. 167, p. 1–22.

Longerich, HP, Jackson, SE and Gunther, D 1996, Inter-laboratory note. Laser ablation inductively coupled plasma mass spectrometric transient signal data acquisition and analyte concentration calculation: Journal of Analytical Atomic Spectrometry, v. 11, p. 899–904.

Lucassen, F, Koch-Müller, M, Taran, M and Franz, G 2013, Coupled H and Nb, Cr, and V trace element behavior in synthetic rutile at 600 °C, 400 MPa and possible geological application: American Mineralogist, v. 98, p. 7–18.

Luvizotto, GL, Zack, T, Meyer, HP, Ludwig, T, Triebold, S, Kronz, A, Münker, C, Stockli, DF, Prowatke, S, Klemme, S, Jacob, DE and von Eynatten, H 2009, Rutile crystals as potential trace element and isotope mineral standards for microanalysis: Chemical Geology, v. 261, p. 346–369.

Martin, DMcB, Sircombe, KN, Thorne, AM, Cawood, PA and Nemchin, AA 2008, Provenance history of the Bangemall Supergroup and implications for the Mesoproterozoic paleogeography of the West Australian Craton, *in* Assembling Australia: Proterozoic building of a continent *edited by* PA Cawood and RJ Korsch: Precambrian Research, v. 166, p. 93–110.

Meagher, EP and Lager, GA 1979, Polyhedral thermal expansion in the TiO_2 polymorphs: refinement of the crystal structures of rutile and brookite at high temperature. Canadian Mineralogist. v. 17, p. 77–85.

Meinhold, G 2010 Rutile and its applications in earth sciences: Earth-Science Reviews, v. 102, p. 1–28.

Meyer, M, John, T, Brandt, S and Klemd, R 2011, Trace element composition of rutile and the application of Zr-in-rutile thermometry to UHT metamorphism (Epupa Complex, NW Namibia): Lithos, v. 126, p. 388–401.

Meyer, O, Khubeis, I, Fromknecht, R and Massing, S 1997, Ions implanted into TiO_2 rutile single crystals: lattice disorder, lattice site occupation and conductivity: Nuclear instruments and methods in physics research Section B: Beam Interactions with Materials and Atoms, v. 127–128, p. 624–628.

Meyer, O, Khubeis, I, Fromknecht, R and Massing, S 1998, Ion implantation in TiO_2: effect of the charge state on the lattice site occupation: Nuclear instruments and methods in physics research Section B: Beam Interactions with Materials and Atoms, v. 136–138, p. 436–441.

Müller, SG, Krapež, B, Barley, ME and Fletcher, IR 2005, Giant iron-ore deposits of the Hamersley province related to the breakup of Paleoproterozoic Australia: New insights from in situ SHRIMP dating of baddeleyite from mafic intrusions: Geology, v. 33, p. 577–580.

Nelson, DR 2001, 168937: metasandstone, Fitzpatrick Well; Geochronology Record 208: Geological Survey of Western Australia, 4p.

Occhipinti, SA 2007, Neoproterozoic reworking in the Paleoproterozoic Capricorn Orogen: evidence from 40Ar/39Ar ages: Geological Survey of Western Australia, Record 2007/10, 41p.

Occhipinti, SA and Reddy, SM 2009, Neoproterozoic reworking of the Palaeoproterozoic Capricorn Orogen of Western Australia and implications for the amalgamation of Rodinia: Geological Society London, Special Publications 327, p. 445–456.

Occhipinti, SA and Sheppard, S 2001, Geology of the Glenburgh 1:100 000 sheet: Geological Survey of Western Australia, 1:100 000 Geological Series Explanatory Notes, 37p.

Occhipinti, SA, Sheppard, S, Nelson, DR, Myers, JS and Tyler, IM 1998, Syntectonic granite in the southern margin of the Palaeoproterozoic Capricorn Orogen, Western Australia: Australian Journal of Earth Sciences, v. 45, p. 509–512.

Occhipinti, SA, Sheppard, S, Passchier, C, Tyler, IM and Nelson, DR 2004, Palaeoproterozoic crustal accretion and collision in the southern Capricorn Orogen: the Glenburgh Orogeny: Precambrian Research, v. 128, p. 237–255.

Paton, C, Woodhead, JD, Hellstrom, JC, Hergt, JM, Greig, A and Maas, R 2010, Improved laser ablation U–Pb zircon geochronology through robust downhole fractionation correction: Geochemistry, Geophysics, Geosystems, v. 11, Q0AA06.

Piechocka, AM, Gregory, CJ, Zi, J-W, Sheppard, S, Wingate, MTD and Rasmussen, B 2018, Monazite trumps zircon: applying SHRIMP U–Pb geochronology to systematically evaluate emplacement ages of leucocratic, low-temperature granites in a complex Precambrian orogeny: Contributions to Mineralogy and Petrology, v. 172, 63p.

Pirajno, F 2004, Metallogeny in the Capricorn Orogen, Western Australia: Precambrian Research, v. 128, p. 411–439.

Pirajno, F, Gonzalez-Álvarez, I, Chen, W, Kyser, KT, Simonetti, A, Leduc, E and LeGras, M 2014, The Gifford Creek Ferrocarbonatite Complex, Gascoyne Province (Western Australia): a putative link to the 1075 Ma Warakurna large igneous province: Acta Geologica Sinica, v. 88, p. 431–432.

Pirajno, F, Sheppard, S, Groenewald, PB and Johnson, SP 2008, Mineral systems in the Gascoyne Complex, Western Australia, *in* GSWA 2008 extended abstracts: promoting the prospectivity of Western Australia: Geological Survey of Western Australia; Record, p. 4–7.

Rasmussen, B, Fletcher, IR and Sheppard, S 2005, Isotopic dating of the migration of a low-grade metamorphic front during orogenesis: Geology, v. 33, p. 773–776.

Reddy, S, Timms, N, Pantleon, W and Trimby, P 2007, Quantitative characterization of plastic deformation of zircon and geological implications: Contributions to Mineralogy and Petrology, v. 153, p. 625–645.

Rice, CM, Darke, KE, Still, JW and Lachowski, EE 1998, Tungsten-bearing rutile from the Kori Kollo gold mine, Bolivia: Mineralogical Magazine, v. 62, p. 421–429.

Rudnick, RL, Barth, M, Horn, I and McDonough, WF 2000, Rutile-bearing refractory eclogites: missing link between continents and depleted mantle: Science, v. 287, p. 278–281.

Schmidt, A, Weyer, S, John, T and Brey, GP 2009, HFSE systematics of rutile-bearing eclogites: new insights into subduction zone processes and implications for the earth's HFSE budget: Geochimica et Cosmochimica Acta, v. 73, p. 455–468.

Scott, KM and Radford, NW 2007, Rutile compositions at the Big Bell Au deposit as a guide for exploration geochemistry: Exploration, Environment, Analysis, v. 7, p. 353–361.

Scott, KM, Radford, NW, Hough, RM and Reddy, SM, 2011, Rutile compositions in the Kalgoorlie Goldfields and their implications for exploration: Australian Journal of Earth Sciences, v. 58, p. 803–812.

Sheppard, S, Bodorkos, S, Johnson, SP, Wingate, MTD and Kirkland, CL 2010a, The Paleoproterozoic Capricorn Orogeny: intracontinental reworking not continent–continent collision: Geological Survey of Western Australia, Report 108, 33p.

Sheppard, S, Johnson, SP, Wingate, MTD, Kirkland, CL and Pirajno, F 2010b, Explanatory Notes for the Gascoyne Province: Geological Survey of Western Australia, 336p.

Sheppard, S, Occhipinti, SA, Nelson, DR 2005, Intracontinental reworking in the Capricorn Orogen, Western Australia: the 1680–1620 Ma Mangaroon Orogeny: Australian Journal of Earth Sciences, v. 52, p. 443–460

Sheppard, S, Occhipinti, SA and Tyler, IM 2004, A 2005–1970 Ma Andean-type batholith in the southern Gascoyne Complex, Western Australia: Precambrian Research, v. 128 (Assembling the Palaeoproterozoic Capricorn Orogen), p. 257–277.

Sheppard, S, Rasmussen, B, Muhling, JR, Farrell, TR and Fletcher, IR 2007, Grenvillian-aged orogenesis in the Palaeoproterozoic Gascoyne Complex, Western Australia: 1030–950 Ma reworking of the Proterozoic Capricorn Orogen: Journal of Metamorphic Geology, v. 25, p. 477–494.

Stacey, JS and Kramers, JD 1975, Approximation of terrestrial lead isotope evolution by a two-stage model: Earth and Planetary Science Letters, v. 26, p. 207–221.

Sun, S-S and McDonough, WF 1989, Chemical and isotopic systematics of oceanic basalts: implications for mantle composition and processes, *in* Magmatism in the Ocean Basins *edited by* AD Saunders and MJ Norry: Geological Society, London, Special Publication 42, p. 313–345.

Swope, RJ, Smyth, JR and Larson, AC 1995, H in rutile-type compounds: I. Single-crystal neutron and X-ray diffraction study of H in rutile: American Mineralogist, v. 80, p. 448–453.

Taylor, R, Clark, C and Reddy, SM 2012, The effect of grain orientation on secondary ion mass spectrometry (SIMS) analysis of rutile: Chemical Geology, v. 300–301, p. 81–87.

Tomkins, HS, Powell, R and Ellis, DJ 2007, The pressure dependence of the zirconium-in-rutile thermometer: Journal of Metamorphic Geology, v. 25, p. 703–713.

Triebold, S, Luvizotto, G, Tolosana-Delgado, R, Zack, T and Eynatten, H 2011, Discrimination of TiO2 polymorphs in sedimentary and metamorphic rocks: Contributions to Mineralogy and Petrology, v. 161, p. 581–596.

Triebold, S, von Eynatten, H, Luvizotto, GL and Zack, T 2007, Deducing source rock lithology from detrital rutile geochemistry: an example from the Erzgebirge, Germany: Chemical Geology, v. 244, p. 421–436.

Triebold, S, von Eynatten, H and Zack, T 2012, A recipe for the use of rutile in sedimentary provenance analysis: Sedimentary Geology, v. 282, p. 268–275.

Tyler, IM and Thorne, AM 1990, The northern margin of the Capricorn Orogen, Western Australia — an example of an early Proterozoic collision zone: Journal of Structural Geology, v. 12, p. 685–701.

Urban, AJ, Hoskins, BF and Grey, IE 1992, Characterization of V–Sb–W-bearing rutile from the Hemlo gold deposit, Ontario: The Canadian Mineralogist, v. 30, p. 319–326.

van Gaans, PFM, Vriend, SP and Poorter, RPE 1995, Hydrothermal processes and shifting element association patterns in the W–Sn enriched granite of Regoufe, Portugal: Journal of Geochemical Exploration, v. 55, p. 203–222.

Whitney, DL and Evans, BW 2010, Abbreviations for names of rock-forming minerals: American Mineralogist, v. 95, p. 185–187.

Wingate, MTD, Bodorkos, S and Sircombe, KN 2007a, 148974: lithic sandstone, Coodardo Well; Geochronology Record 691: Geological Survey of Western Australia, 6p.

Wingate, MTD, Bodorkos, S and Sircombe, KN 2007b, 148972: feldspathic sandstone, Ulna Well; Geochronology Record 689: Geological Survey of Western Australia, 7p.

Wingate, MTD, Kirkland, CL, Bodorkos, S, Groenewald, PB and Sheppard, S 2010a, 187403: quartzite, Robinson Bore; Geochronology Record 862: Geological Survey of Western Australia, 5p.

Wingate, MTD, Kirkland, CL, Bodorkos, S and Sheppard, S 2010b, 184160: psammitic schist, Weedarrah Homestead; Geochronology Record 863: Geological Survey of Western Australia, 5p.

Wingate, MTD, Kirkland, CL and Johnson, SP 2011, 188975: biotite metatonalite, Daly Bore; Geochronology Record 980: Geological Survey of Western Australia, 6p.

Wingate, MTD, Kirkland, CL, Sheppard, S and Johnson, SP 2010c, 185950: gneissic granite, Lucky Bore; Geochronology Record 903: Geological Survey of Western Australia, 5p.

Zack, T, Kronz, A, Foley, SF and Rivers, T 2002, Trace element abundances in rutiles from eclogites and associated garnet mica schists: Chemical Geology, v. 184, p. 97–122.

Zack, T, Stockli, D, Luvizotto, G, Barth, M, Belousova, E, Wolfe, M and Hinton, R 2011, In situ U–Pb rutile dating by LA–ICP–MS: 208Pb correction and prospects for geological applications: Contributions to Mineralogy and Petrology, v. 162, p. 515–530.

Zack, T, von Eynatten, H and Kronz, A 2004, Rutile geochemistry and its potential use in quantitative provenance studies: Sedimentary Geology, v. 171, p. 37–58.

Appendices

Appendix 1A

U–Pb concordia and weighted average ages for rutile standards R10, PCA and 9826J

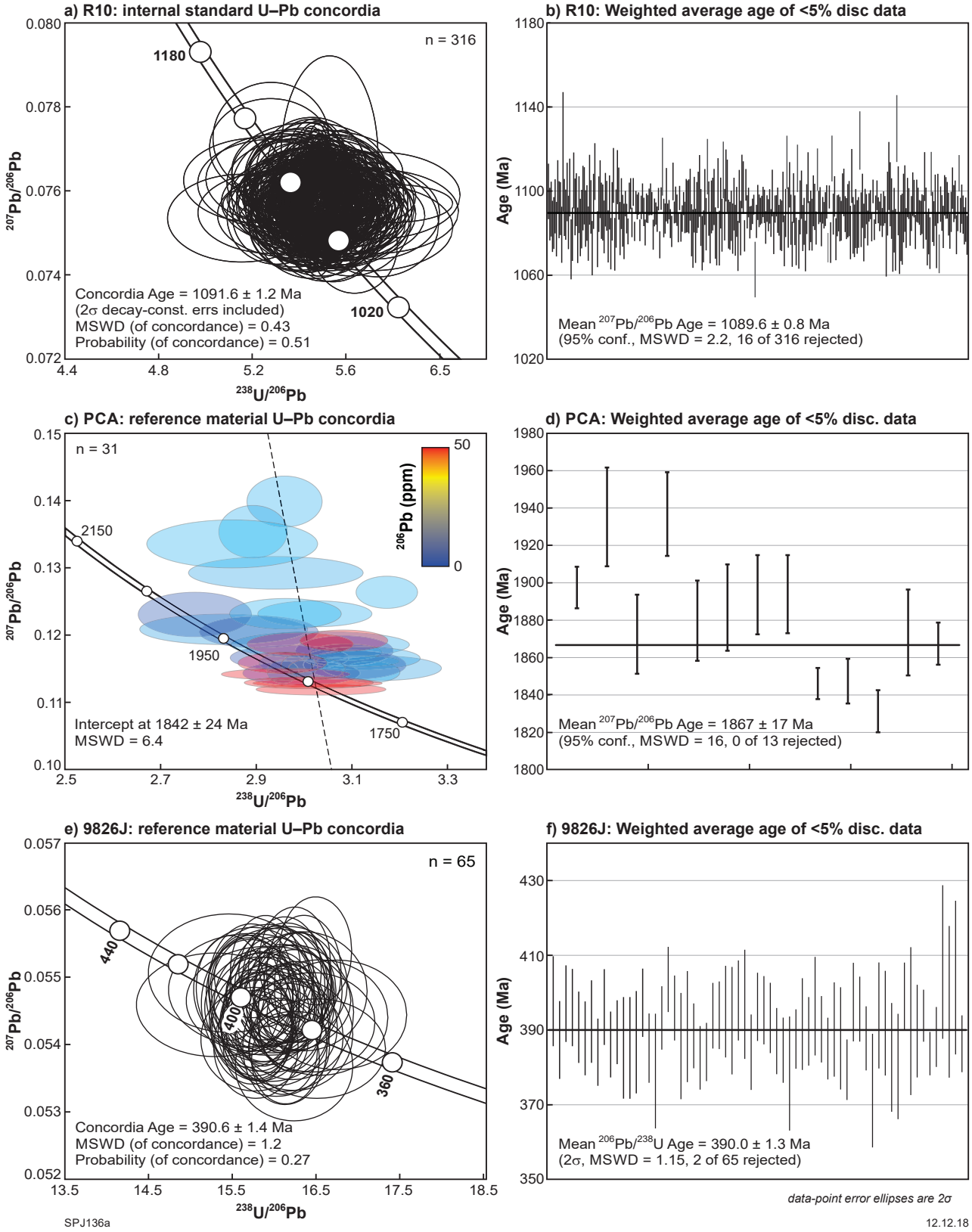

Appendix 1B

U–Pb concordia and weighted average ages for rutile standards SUG and WHQ

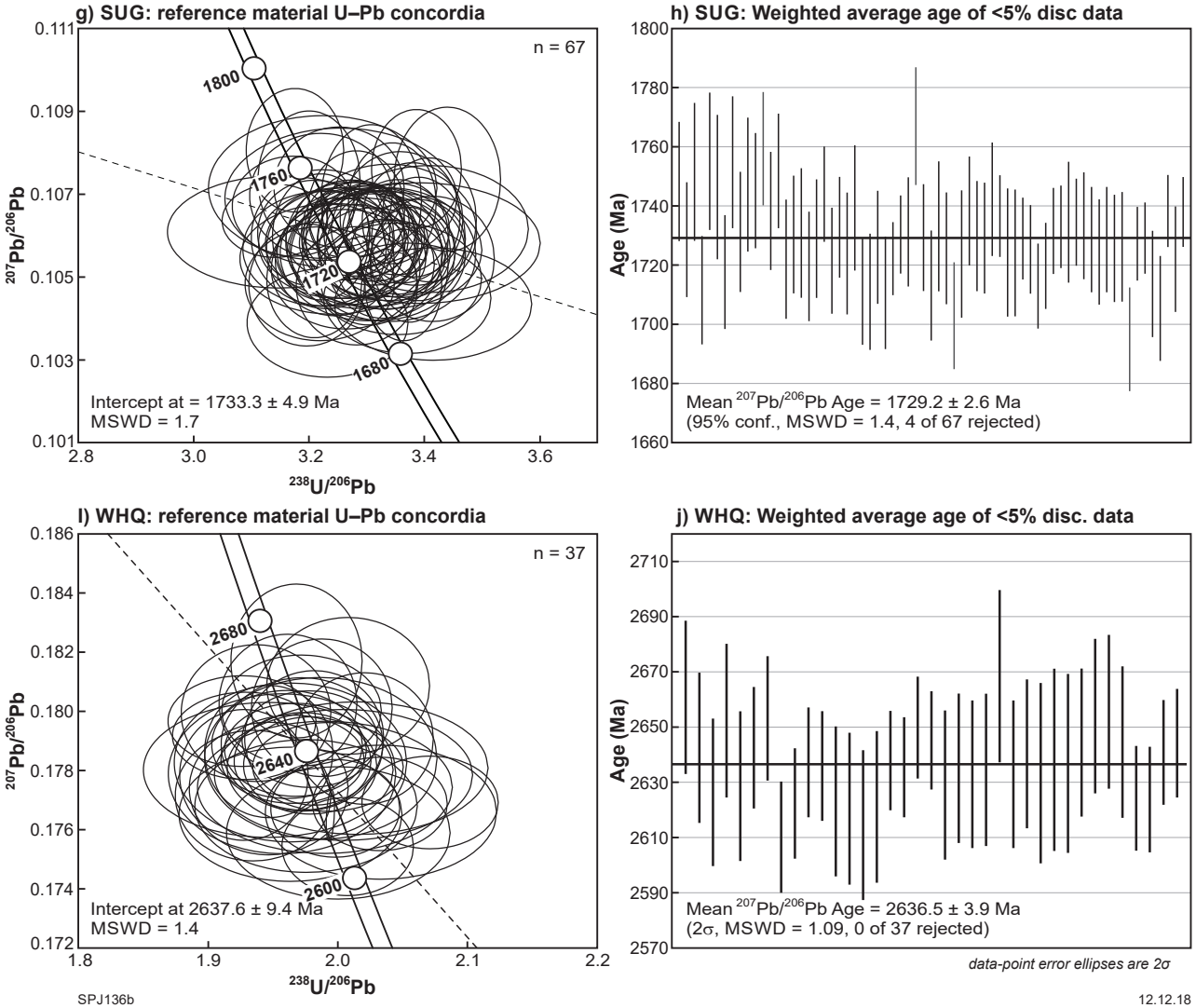

Appendix 2A

Trace element (Al, Cu, Nb, Sn, Sb, Cr, Fe and V) variations in the reference standard R10 before and after polishing halfway through the analytical session

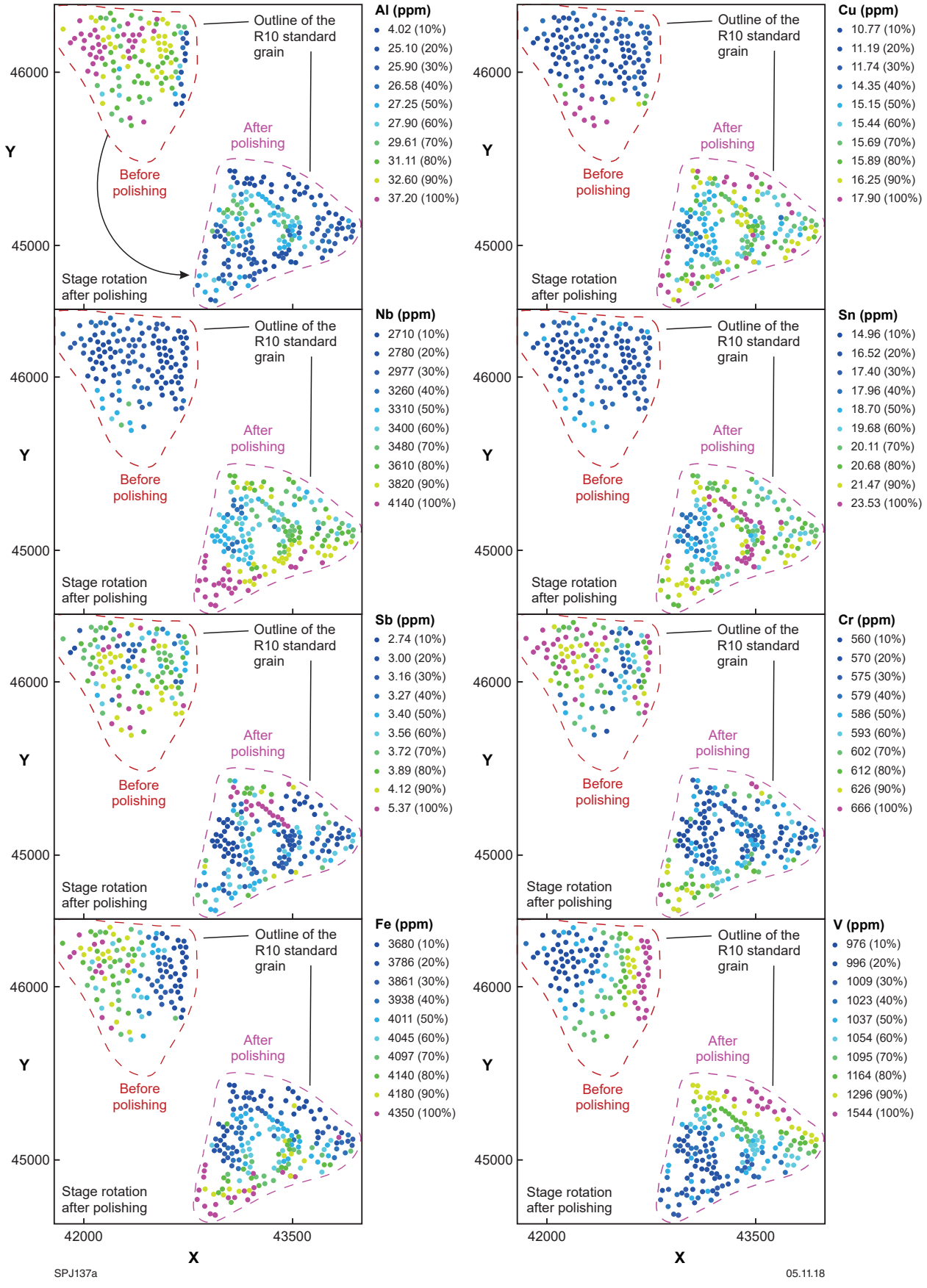

Appendix 2B

Trace element (W and Ta) variations in the reference standard R10 before and after polishing half-way through the analytical session

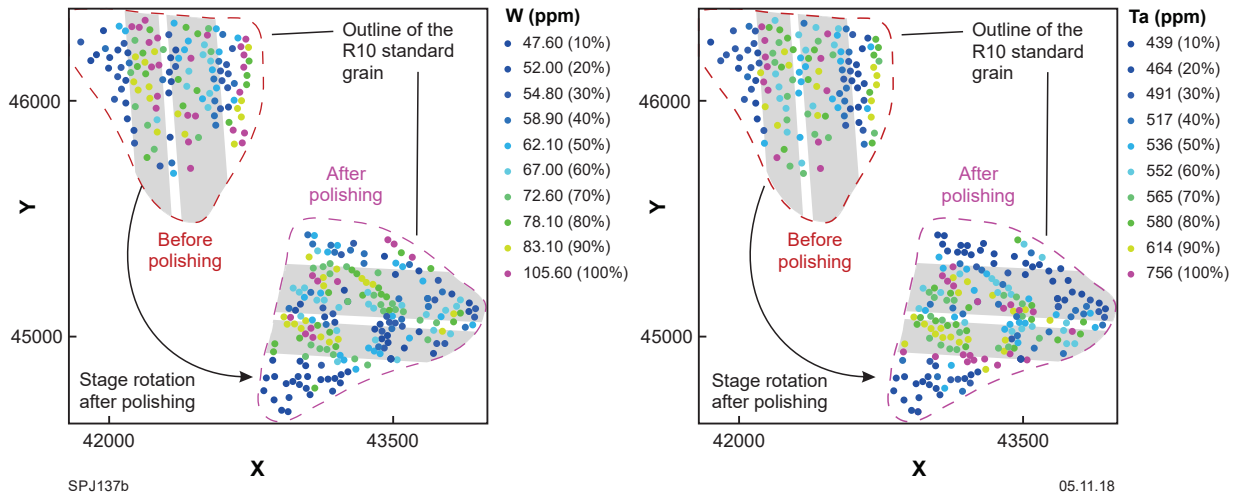

Appendix 3

Backscatter electron (BSE), EDS and EBSD maps of TiO_2 grains from Moorarie Supersuite samples

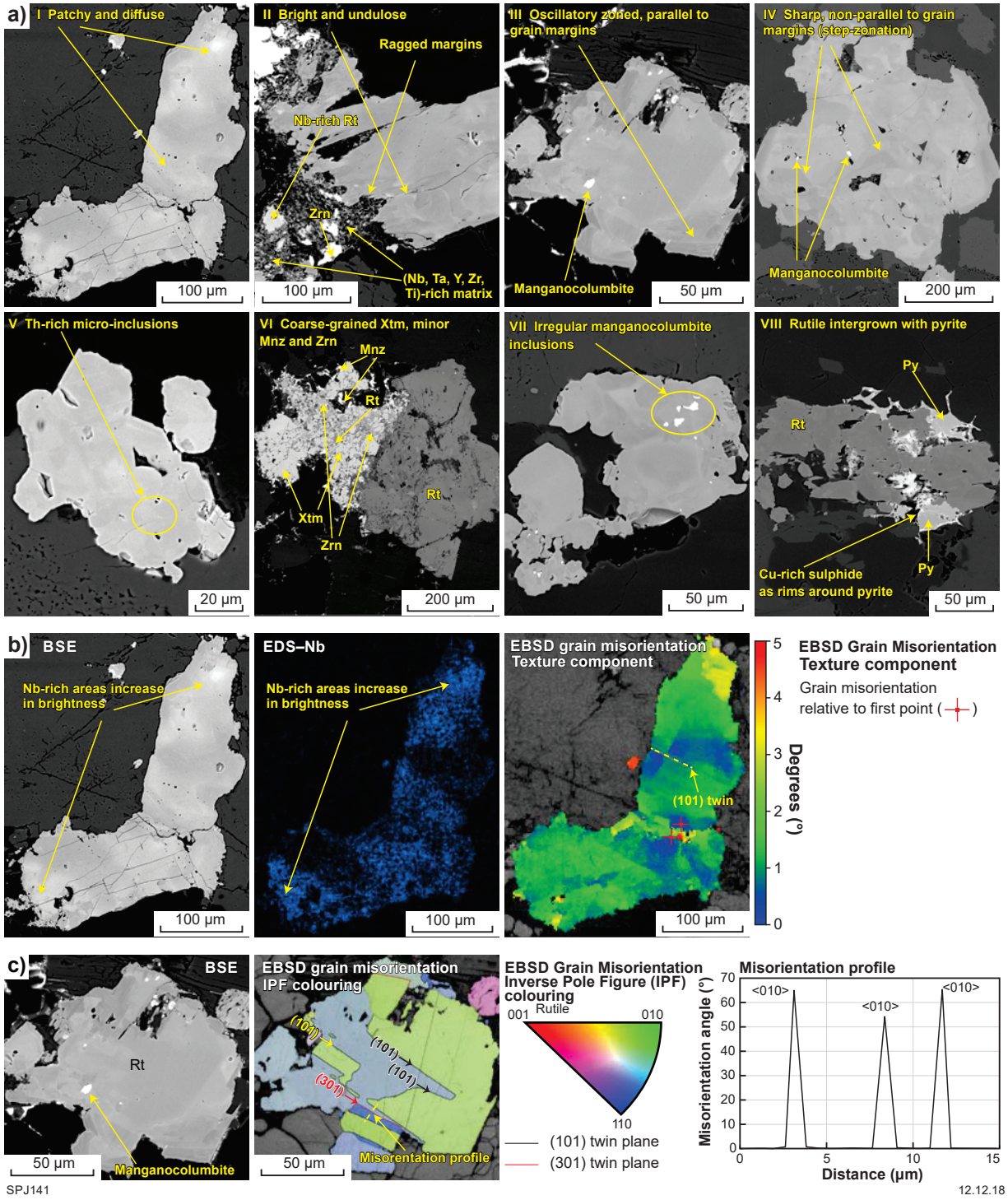

Appendix 4

Age vs U plot showing decrease in age with decreasing U concentration

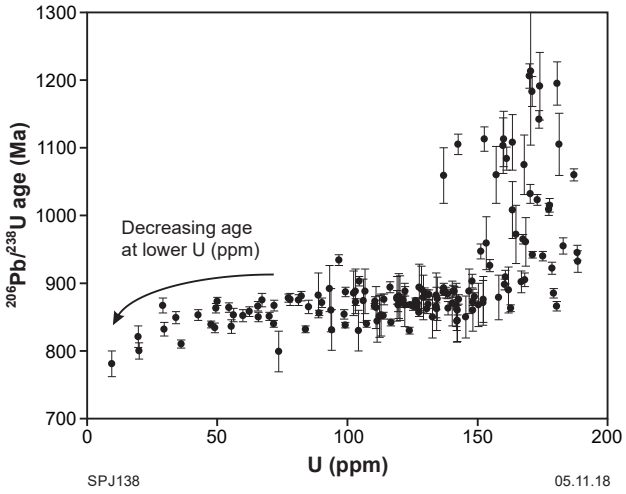

Appendix 5

U–Pb concordia diagrams and probability diagrams for Leake Spring Metamorphics samples

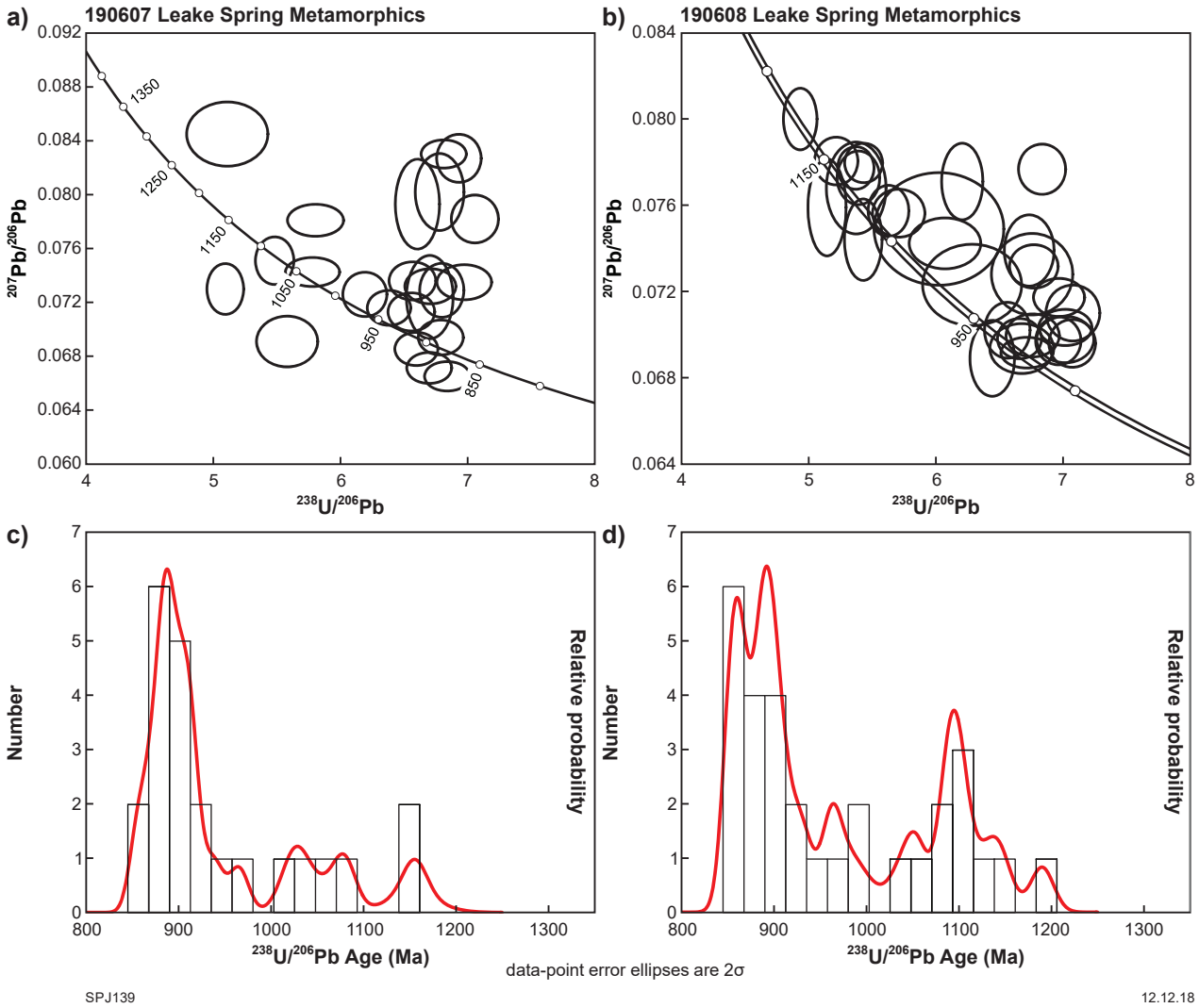

Appendix 6

U–Pb results for Warrigal Gneiss sample GSWA 44617 and Dalgaringa Supersuite sample

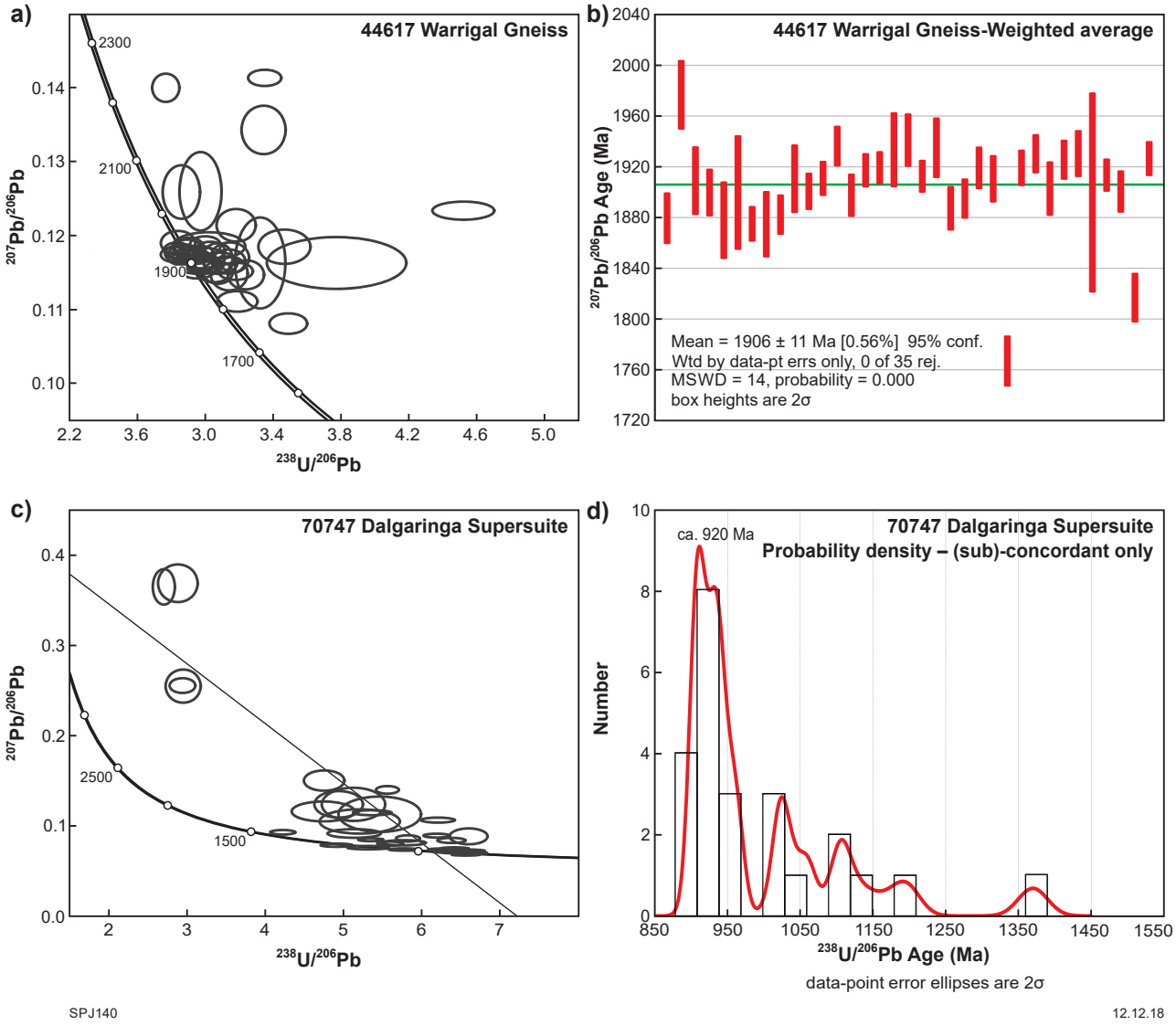

RECORD 2018/12

CAPRICORN OROGEN RUTILE STUDY: A COMBINED ELECTRON BACKSCATTER DIFFRACTION (EBSD) AND LASER ABLATION SPLIT STREAM (LASS) ANALYTICAL APPROACH

Plavsa et al.